SYNTHESIS AND DOPING OF NICKEL AND ZINC TUNGSTATE WITH GROUP 11 ELEMENTS FOR THE ANALYSIS OF PHOTOCATALYTIC PROPERTIES

A THESIS

SUBMITTED TO THE GRADUATE SCHOOL

IN PARTIAL FULFILLMENT OF THE REQUIREMENTS

FOR THE DEGREE

MASTER OF SCIENCE

BY

ANDREW RILEY

DR. ZHIHAI LI - ADVISOR

BALL STATE UNIVERSITY

MUNCIE, INDIANA

JULY 2019

Table of Contents

Table of Figures

List of Tables

1 – Introduction to Tungstate Semiconductors

Nickel and zinc tungstate are semiconducting compounds, possessing many specific electronic properties. These properties allow nickel and zinc tungstate, as well as many other semiconductors, to be applied to a variety of different technologies and chemical systems. These technologies include integrated circuits[1], LED displays[2], and solar cells[3–5]. In a chemical context, they can be used for photocatalysis of organic compounds[6,7], and photodegradation of organic contaminants[2,8,9]. Below, the properties which allow for these applications will be explained.

Currently semiconductors such as TiO_2 has received much attention for its preferable band positioning which allows it to perform many reactions[10], but its large band gap prevents it from harnessing the majority of sunlight's emitted photons. Tungstates have come into view for their similar band positioning, but potentially lower band gap which allows for higher activity in sunlight. Currently, many tungstates have been synthesized by various groups, but extended research into the modification of these structures for photocatalysis is an area which is lacking literature. This study aims to investigate the role in dopants for the band positioning and reduction in band gap for metal tungstates in order to provide a better photocatalyst.

1.1 – Semiconductors

Semiconductors are a class of compound which exhibit conductive properties under specific conditions, where a conductor classically has no energy difference between its valence and conduction band[1], a semiconductor has an energy separation ranging from 0.5-5 eV (Figure 1)[11]. On the other end of the spectrum, an insulator has an energy difference between the

valence and conduction band which is so large, that there is a negligible amount of excitation of valence electrons (Figure 1). While conductors are ubiquitous within modern society for their ability to easily transfer heat and electricity, semiconductors have become an area of increased interest in the field of integrated circuits.

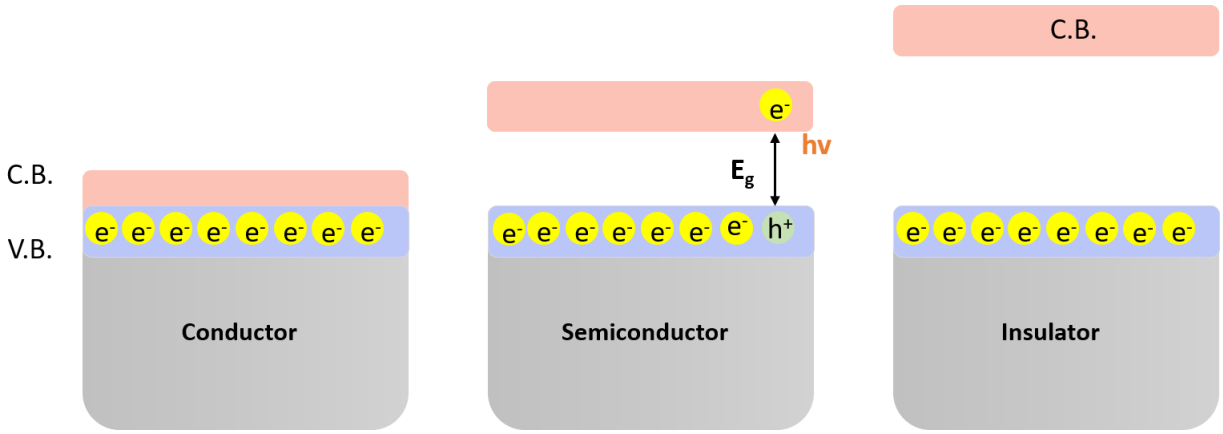

Figure 1: An illustration of the various band gap energies of a conductor, semiconductor, and insulating materials

1.1.1 – Properties

Energy Gap

The energy gap (E_G), sometimes called the band gap, refers to the difference in potential energy between an electron in the valence band (HOMO) of a semiconductor and an electron in the conduction band (LUMO). These values are relative to different materials studied, but are essential to the classification of conductors, semiconductors, and insulators. As discussed earlier, semiconductors generally have a band gap between 0.5-5 eV, which is in the range of ~250-2500nm when translated to wavelengths of light.

Compared to the visible spectrum, ranging from 400-700nm, there exist many semiconductors which can be excited through sunlight – a form of electromagnetic irradiation.

This is a very important property for studies in photocatalysis, which uses an initially inert semiconductor to perform redox reactions under illumination[12], as illustrated in Figure 2.

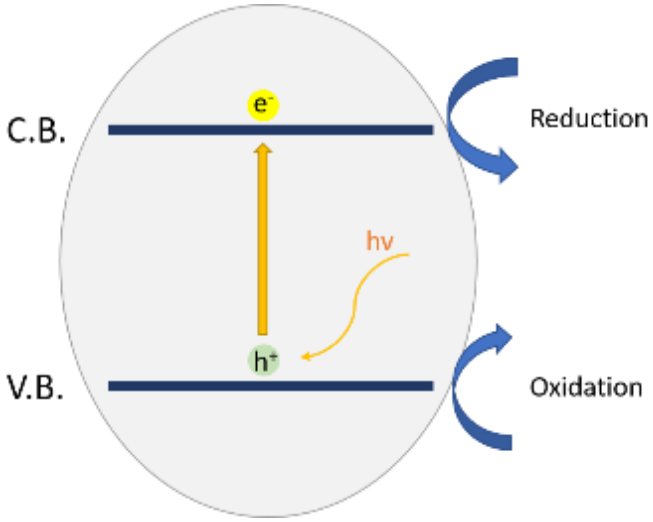

Figure 2: Redox reaction on the surface of a semiconductor under illumination of light

Once excited, the electrons and holes can either drive reactions or recombine.

Fermi Level

The Fermi level, or E_F, describes the energy level at which there is a 50% chance an electron is occupying when at thermodynamic equilibrium[1]. In a conductor, this level exists at the center between the overlapping conduction and valence band. In a semiconductor, however, these bands are separated by an energy barrier which must be overcome for an electron to be excited or relax between them. In this system, the E_F lies somewhere between these two bands. In the case of an intrinsic semiconductor, this level would exist directly in the middle of the energy gap[13]. This level can change under different conditions, such as temperature or applied electronic potentials. It can also be changed from a structural standpoint through doping.

The location of the Fermi Level is especially important in semiconductors when electron transfer takes place. When an interface exists between the surface of a semiconductor and another matrix, whether it would be an electrolytic solution or another semiconductor, an equilibrium process takes place.

Doping

Doping describes the addition of specific impurities to a material. These impurities are generally chosen in relation to the elements within a material. A classic example is silicon, which can be doped with boron to create a p-type semiconductor[14]. Boron, which sits one group to the left of silicon, possesses one less valence electron than silicon. This absence of a valence electron can be thought of as an electron hole. Like an electron in an open conduction band, an electron hole can move relatively freely within a heavily occupied valence band[1].

In terms of E_F, a p-type doped semiconductor would have a Fermi level closer to the valence band than the same semiconductor without a p-type dopant[1]. The same idea can be applied to an element with one more valence electron than the semiconductor. This is referred to as an n-typed doped semiconductor. In this scenario, there is a relative excess of electrons in the valence band. The n-type doped semiconductor would have a Fermi level closer to the conduction band of the semiconductor.

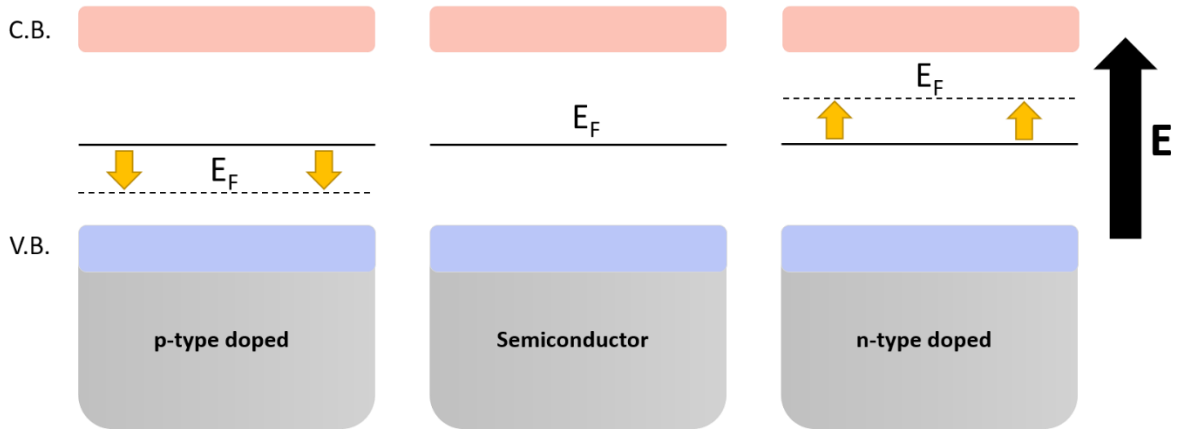

Figure 3: Relative fermi energy levels based on doping type

1.2 – Metal Tungstates

Metal tungstates are a group of metal oxide semiconductors with the general chemical equation of $M_X(WO_4)_Y$, where 'M' represents a transition metal, and 'X' and 'Y' represent a ratio based on the charge of the transition metal ion and tungstate. Tungstate alone is written as WO_4^{2-}, and as an example silver tungstate formed with Ag(I) would be written as Ag_2WO_4. Due to the wide amount of different atoms which can be stably coordinated with tungstate, this class of semiconductor can possess various electronic and physical properties, and have been studied for application in sensor[15], catalytic[16–18], and photovoltaic[3] systems.

1.2.1 – Various Properties of Tungstate Semiconductors

Many metal tungstate complexes have been synthesized and characterized in labs, and as a result there exist some cross-sectional studies comparing different metal tungstates in terms of their properties and efficiencies in various applications. A metal tungstate will usually exist as a complex between a transition metal coordinated with a WO_4^{2-} anion, adopting a crystal structure

dependent on the size and oxidation state of the cation. In this study, two tungstates have been explored, nickel and zinc tungstate, for their electronic properties. These tungstates have been chosen for their relative photocatalytic performance and band positioning. Nickel tungstate has a low band gap which makes it preferable to currently popular materials such as TiO_2, but its band positioning prevents it from reduction of reactive oxygen species in water[19]. Zinc tungstate has the ability to both oxidize and reduce reactive oxygen species in water, but its high band gap gives it the same issue as TiO_2 with low reactivity in sunlight.

Nickel Tungstate

Nickel tungstate exists as a complex of tungstate ions and Ni(II) ions. Nickel's atomic radius is much smaller than tungsten's, causing the material to adopt a wolframite structure with a P2/c symmetry[20]. Nickel tungstate's band gap is variable, and has been reported to exist between 2.5-3.5eV[20–23]. This variation is due to various factors, such as size, crystallinity, and synthetic methods. Nickel tungstate has gained attention from the group of metal tungstates due to its relatively large surface area[24], lending itself to use in sensor devices[15] and photocatalyst systems[2].

Zinc Tungstate

Zinc tungstate is similar to nickel tungstate in the fact that it is a complex of tungstate ions and Zn(II) ions. Also like nickel tungstate, its relatively low atomic radius causes it to adopt a wolframite structure with a space group of P2/c[25]. Like all metal tungstates, its electronic

properties vary greatly depending on the size and shape of the nanoparticles, but its band gap is generally around 4.2 eV[18,26], leaving its excitation wavelength beyond the visible spectrum. Despite this fact, zinc tungstate has shown a relatively high photocatalytic yield when compared to other metal tungstates[19].

Copper Tungstate

Copper Tungstate exists in a similar wolframite structure[27] to nickel and zinc tungstate, but its d^9 electronic configuration leads to Jahn-Teller distortion. This causes $CuWO_4$ to take a triclinic P-1 spacing compared to $NiWO_4$ and $ZnWO_4$ which exist as a monoclinic structure[28]. This distortion causes $CuWO_4$ to have a relatively low band gap of around 2.2 eV compared to other M^{II} cations which have band gaps above 3.0 eV[29].

Silver Tungstate

Silver tungstate is unique to the other tungstates discussed as it exists as a M_2WO_4 structure. Synthesis of silver tungstate is also unique in the fact that calcination is not required to form crystalline Ag_2WO_4[30]. Nanophased silver tungstate has a band gap of around 3.2 eV[8], and precipitates in a rod shape. It exists in an orthorhombic structure with a space group of Pn2n.

1.2.2 – Synthetic Methods of Tungstate Semiconductors

There exist many methods for synthesizing metal tungstates, many of which focus on either providing a cost-effective and scalable method geared toward mass production, or those

which focus on refining some property of these materials such as size or band gap. Below are a few notable methods.

Coprecipitation

A coprecipitation method is the most common route of synthesis for these materials. Along with its simplicity, it is extremely scalable. In a coprecipitation synthesis, a transition metal salt is added to a solution containing WO_4^{2-} ions, resulting in an almost immediate precipitation of the desired metal tungstate, as illustrated in Figure 4.

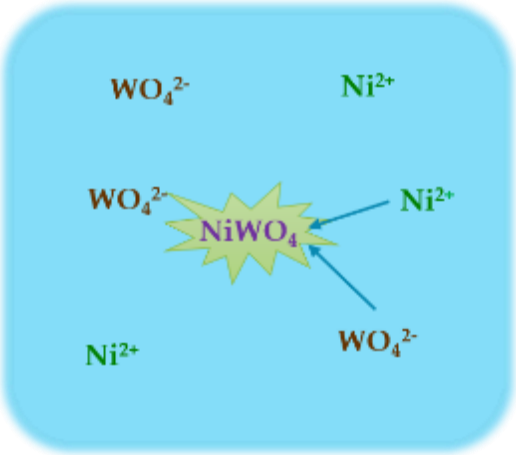

Figure 4: Coprecipitation scheme of $NiWO_4$

Various modifications can be made to this procedure, such as addition of a surfactant[8], use of solvent mixtures[31], changes in rate of addition[32,33], or addition under sonication[23]. Each of these methods aims to optimize some trait of these nanoparticles. Once the nanoparticles have precipitated completely, they are generally washed through centrifugation and then calcinated in the range of 400-600°C for multiple hours[29] in order to promote complete coordination between metal atoms and tungstates.

Solid-State Metathesis

A solid-state approach to metal tungstate synthesis opts to remove a solvent from the reaction scheme. One disadvantage of this approach is that precipitation within a solution involves many factors which may not be able to be consistently controlled such as rate of addition or temperature of solution. The Kumari group successfully formed multiple transition metal tungstates through this approach by grinding metal chlorides and tungstate salts for 2 hours, followed by calcinating at 400°C[34]. X-Ray Diffraction (XRD confirmed highly crystalline products, although average and median particle size was not reported.

The Parhi group reported a separate solid-state method with similar materials, opting to use a microwave to aid the formation of the metal tungstates before calcination[35]. This novel method employed the use of a consumer-grade microwave to demonstrate a low-cost method of synthesizing these powders. Standard calcination procedures were taken, and crystalline products were confirmed by XRD.

Sol-Gel Formation

One application, formation of scintillators, or materials which can convert X-ray light into more easily detected UV-light, was approached using a sol-gel method of synthesis. L. Nadaraia and their group investigated forming multiple metal tungstates through this synthetic method in order to form nanocrystalline powders[36]. This method involves mixing of the salts within a solvent, with the addition of some organic phase which helps form a colloid. The solvent is then slowly evaporated away, turning the sol (solution) into a solid phase, referred to

as a gel. This gel is an agglomeration of many nano-sized crystals. This gel can then be ground into a powder and calcinated to form a crystalline product. The resulting crystals averaged sub-micron sizes.

The Zalga group performed a similar experiment, with the addition of forming molybdates. Tartaric acid was used as a complexing agent, as it is saturated with oxygen-containing functional groups which can coordinate with metal cations. Ratios of molybdate and tungstate were used with calcium to investigate properties of these combined crystals[37].

Solution Combustion Synthesis

A solution combustion synthesis has also been used with great success to form ultrafine metal tungstate nanoparticles[38]. This synthetic method begins similarly to a coprecipitation method, but with the addition of a fuel such as urea. This solution is then placed in an oven and heated at a high temperature until the fuel combusts. The resulting particles showed sizes ranging from 10-20nm with very low variation of 1-2nm depending on the compound.

For this study, a coprecipitation method has been employed, due to its allowance for surfactant mediated size control to be used, as well as a hydrothermal step in some experiments. The time and cost factor also play a role in the preference to this method.

1.3 – Applications of Metal Tungstates

As discussed, the varying properties of metal tungstates lends them to a wide field of applications. Their wide band gap provides them with sufficient ability to perform redox reactions, and their high surface area allows for great catalytic activity. Tungstates have been applied in the fields of photovoltaics, photochemistry, and photocatalysis, among others.

1.3.1 – Photovoltaic Cells

Photovoltaic cells are a growing area of interest for clean energy generation. Semiconducting materials lie at the heart of photovoltaics, as the energy from a photon is converted to electricity through the movement of excited electrons[5]. Tungstates have shown some ability for photovoltaics due to their fine particle sizes and high surface area, which make them suitable for dye-sensitized systems[4].

The Kharat group investigated the efficiency of spray deposited $NiWO_4$ thin films as a photovoltaic material, which showed a power conversion efficiency (PCE) of 0.78%, and a fill factor (FF) of 0.47[3]. One large problem with photovoltaics is finding materials which show high stability over prolonged periods of use while also having a high power conversion efficiency. Dye sensitization is one way to help increase the PCE.

The Li group has also experimented with $NiWO_4$ thin films as a photovoltaic material, choosing to modify the $NiWO_4$ through doping and coating with graphene as a cocatalyst. By doping $NiWO_4$ with up to 10% copper, it was found that PCE increased by 6×, though FF remained low at around 0.4. FF can be an indicator of the material and also the construction of

the cell. When the bulk $NiWO_4$ was coated with graphene, an increase in PCE of up to 2.5× was observed, and FF doubled from 0.21 to up to 0.45[39].

1.3.2 – Sensors

$NiWO_4$ has been explored for sensor applications by the Liu group, which employed a hydrothermal synthesis of $NiWO_4$ nanoparticles as an enzyme-free glucose sensor[15]. $NiWO_4$'s high surface area and porosity provides the opportunity for large adsorption of glucose in solution, which was detected through cyclic voltammetry (CV) and evaluated through electrochemical impedance spectroscopy (EIS). A glassy carbon electrode (GCE) modified with the nanoparticles showed enhanced activity for detection of glucose.

1.4 – Photocatalysis

Photocatalysis is a process in which a reaction becomes more thermodynamically favorable in the presence of light. This process is often mediated by the presence of a semiconducting material[8,18,38]. The benefits of using a semiconductor to perform these reactions is that an electron with a very high level of energy can participate in a redox reaction. This allows for reactions which would not normally happen under standard conditions or at low temperatures.

Currently, photocatalysis has been demonstrated as a novel method to tackle various issues such as energy conversion or the reduction of environmental contaminants. Reactions which participate in energy conversion or formation of energy storing compounds include water

splitting[10,40,41] and CO_2 reduction[12,42,43]. The reduction of environmental contaminants is much more broad.

A photocatalytic reaction requires two concurrent steps. When an electron on the surface of the semiconductor is excited by light of a sufficient energy, it becomes available to react with a species adsorbed to the surface of the particle. In the valence band, an electron hole is also present which must also participate in a reaction to return the semiconductor to its electrostatic equilibrium[27]. These steps can only take place if the redox reactions are thermodynamically favorable.

Illustrated in Figure 2, the reduction potential of the species reacting with the electron must be at a lower energy than the excited electron, and the oxidized species must have a reduction potential above the energy level of the valence band of the semiconductor. While photocatalysis at its core is a process which can be performed via simple metal oxide semiconductors, much exploration has been done into optimizing and enhancing photocatalytic yields for standard materials.

Below, a few different photocatalysis experiments are outlined as performed by various groups working with tungstate materials:

1.4.1 – Photodegradation

Methylene Blue

Methylene blue is a dye used in biological staining[44], as well as an antifungal in aquariums[45]. Figure 5 shows the structure of methylene blue.

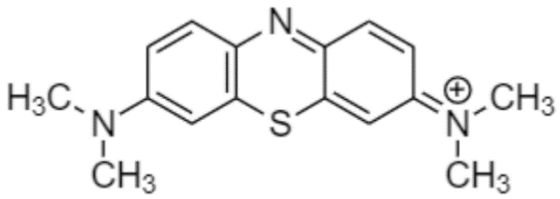

Figure 5: Methylene blue ion as found in solution

As a strongly conjugated heterocyclic aromatic compound, methylene blue has extremely high absorbances in the visible spectrum, with an extinction coefficient of 9.5×10^4 at 664nm[46]. Methylene blue strongly absorbs in the red visible light region, especially at 610 and 664nm. These arise from the benzene ring and the heteropolyaromatic system[47]. For this reason, methylene blue is an extremely popular dye to use when testing the efficiency of photocatalysts. The photocatalyzed degradation of methylene blue is not solely a direct reaction between the semiconductor and the dye, but can be a multi-step reaction as outlined below, where 'SC' is the abbreviation for the semiconductor of study, MB represents methylene blue, and (e^-) and (h^+) represent charge carriers on the surface of the semiconductor[48]:

1) $SC + hv \rightarrow SC(e^-) + SC(h^+)$

2) $SC(e^-) + O_2 \rightarrow SC + O_2^{\bullet-}$

3) $SC(h^+) + HO^- \rightarrow SC + HO^{\bullet}$

or

4) $SC(h^+) + MB^* \rightarrow SC + MB^+$

For step 4 in the above outline, the ionized methylene blue is unstable and rapidly decomposes.

Rhodamine B

Rhodamine B, abbreviated as RhB, is a dye with versatile applications, such as biological staining[49] and use for laser-based analysis[50]. Figure 6 illustrates the structure of Rhodamine B:

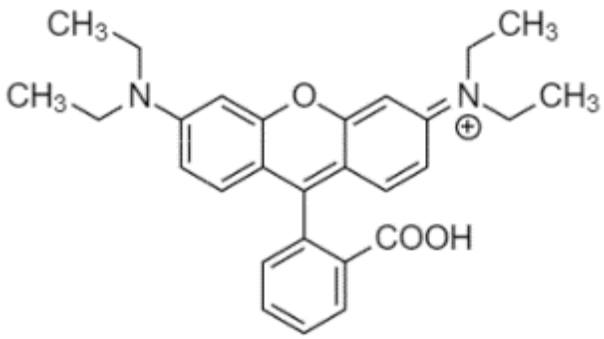

Figure 6: Molecular structure of Rhodamine B dye cation

Rhodamine B is another strongly conjugated compound with multiple benzene groups and a heterocyclic portion. It absorbs very strongly at a wavelength of 554nm[51] with an extinction coefficient of 1.06×10^5, and has a strong pink color in dilute concentrations[52].

A study by the Longo group investigated the morphological effect on photocatalytic efficiency for Ag_2WO_4 on RhB dye[8]. Like the degradation of Methylene Blue, the decay of RhB occurs from an oxidative attack. The active oxygen species are formed through redox reactions on the photocatalyst surface. These oxygen species attack one of the two N-ethyl groups, resulting in an N,N,N'-triethylated RhB, which shifts the absorbance to 539 nm. Further attacks can occur at the remaining ethyl groups, leading to N,N'-diethylated RhB with an absorbance of 522 nm, an N'-ethylated RhB with an absorbance at 510 nm, and finally a completely de-ethylated RhB with an absorbance at 498 nm. This creates a shouldering effect, where the absorbance at 554 nm will decrease as photocatalysis proceeds, but the shoulder at lower

wavelengths will decrease less rapidly due to the higher concentration of partially reacted species as a result of the degradation of the fully formed RhB species.

1.4.2 – Photocatalytic Synthesis

Tetrazoles

Tetrazoles are an important class of organic compounds which contain aromatic five membered rings composed of four nitrogen atoms and a carbon. They are generally formed through a reaction of a nitrile group with an azide salt, and the reactions often use a catalyst. The Yin group performed an intensive study on multiple tungstate compounds to evaluate relative efficiency of catalysis for these compounds[6].

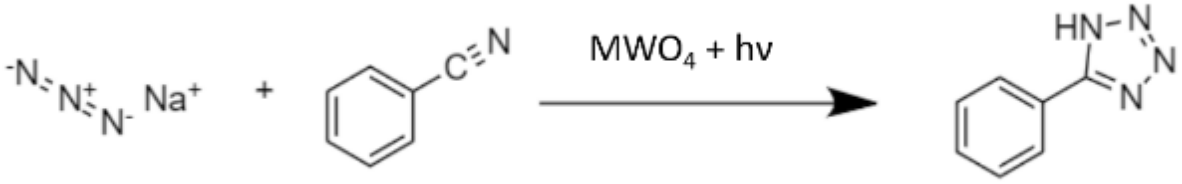

Figure 7: Tungstate catalyzed formation of a tetrazole compound

In the case of transition metal tungstates, it was discovered that the coordinated metal was not a source of catalytic activity. It was found that the reactions depended almost entirely on the WO_x polyhedrons, which existed as the active sites. Interestingly, higher surface area of a catalyst did not correlate to higher yields. It was proposed that vacant sites on the W atoms activate the nitriles and enhance their reactivity to the azides in solution, and that oxygen vacancies were the key to increased activity.

1.5 – Cocatalysts

One such optimization for photocatalysts is the addition of a cocatalyst. A cocatalyst is a separate structure which exists at an interface of the main photocatalyst. This cocatalyst is usually light insensitive, helping direct the electron movement from the semiconductor material, as the cocatalyst does not have an E_G capable of promoting electrons to a much higher energy level. A classic example of this process would be platinum nanoparticles deposited onto the surface of TiO_2[41,53]. The role of the TiO_2 is to absorb light, causing its electrons to be excited. As discussed earlier in section 1.1.1, one of the possible outcomes of excitation is the recombination of an electron and its hole. By placing a conductive material on the surface of the semiconductor, the electron has an additional path it can travel to. By traveling to a metal such as platinum, the electron is able to relax partially, but maintain an energy level high enough to still perform a specific reaction[54].

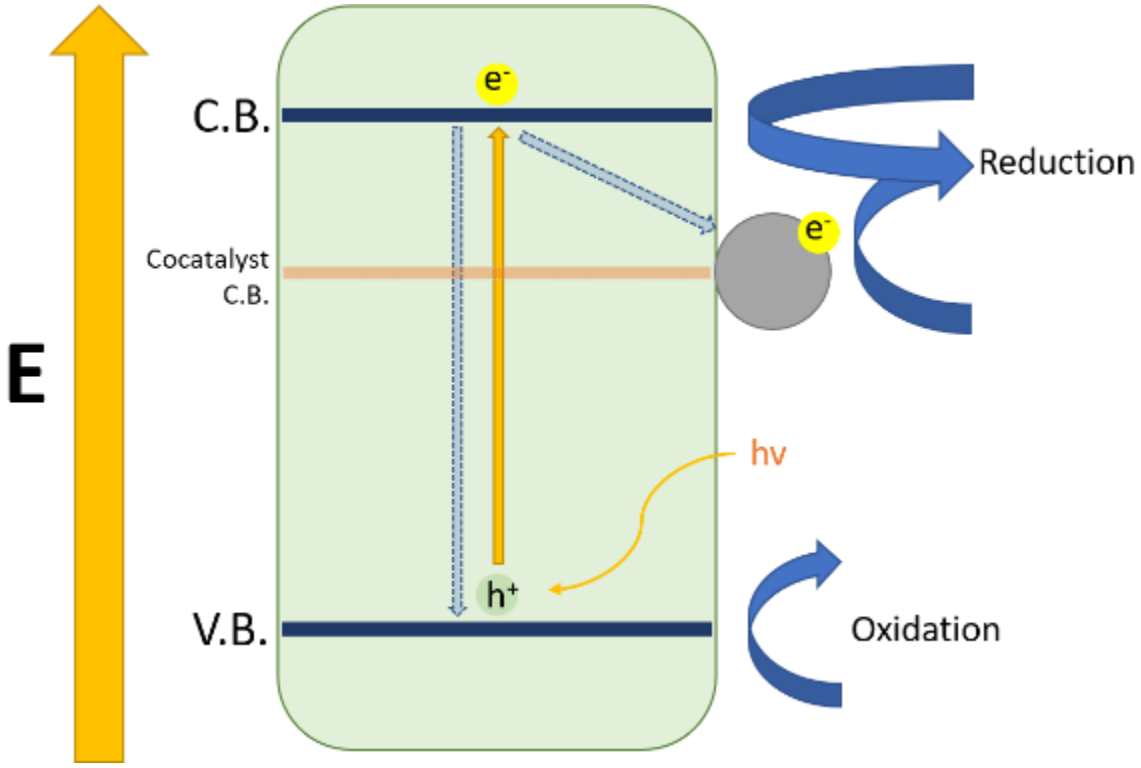

Figure 8: Mechanism of a cocatalyst assisting a semiconductor in a redox reaction

In a study by the Yang group[41], it was discussed that the fermi level for Pt nanoparticles is appropriate for a hydrogen evolution reaction (HER), which is described by the following formula:

$$2H^+ + 2e^- \rightarrow H_2$$

The benefit of a conductor-semiconductor junction lies at the creation of a Schottky barrier[55], in which electrons are able to be quickly transferred away from the semiconductor surface and held at the fermi level of the conductor. This greatly reduces the likelihood of electron-electron hole recombination. It is still important to consider the relative energy levels of the fermi level of the conductor and the redox potential of the species being acted upon, however.

In a study performed by Boz and his group, TiO_2 coated with Ag_2O nanoparticles was investigated for its enhanced photocatalytic activity toward methylene blue dye[48]. They

proposed that two pathways exist for an excited electron in a semiconductor with a cocatalyst on its surface. In one pathway, the electron can travel directly to an O_2 molecule adsorbed to its surface, reducing it to O_2^- where the superoxide can react with the MB dye to degrade it. In the second pathway, the excited electrons can move to the valence band of Ag_2O, reducing the recombination rate on the semiconductor. This was experimentally supported by a higher rate of photodegradation with higher amounts of Ag_2O on the surface, though a point is reached where there is an excess of Ag_2O on the surface and the excess Ag^0 on the surface can no longer prevent recombination.

The proposed mechanism by the Boz group:

1) $TiO_2 + hv \rightarrow TiO_2(e^-) + TiO_2(h^+)$

2) $\begin{cases} a) \ TiO_2(e^-) + O_2 \rightarrow TiO_2 + O_2^{\bullet -} \\ b) \ TiO_2(e^-) + Ag_2O \rightarrow TiO_2 + Ag_2O(e^-) \end{cases}$

2b) $Ag_2O(e^-) + Ag^+ \rightarrow Ag_2O + Ag^0$

2c) $Ag^0 + O_2 \rightarrow Ag^+ + O_2^{\bullet -}$

A co-catalyst exists as a heterostructure to the main catalyst, and thus it requires additional synthetic steps in order to be properly deposited. There are many different deposition methods which have gained favor for their efficiency and ease, though each has its own benefit and downfall. Such methods include photodeposition[56] and electrodeposition[57].

Photodeposition

A typical photodeposition reaction for a metal on the surface of a semiconductor involves the suspension of the semiconductor in a solvent in which it remains colloidal. Alternatively, constant stirring can be employed to keep the particles suspended within the solution. Next, a salt of a certain metal is chosen is added to the solution in low quantities. The quantity of salt added relates to the amount of nanoparticles produced on the surface of the semiconductor, as well as the size. Once the mixture is properly homogenized, the solution is exposed to high intensity light, which helps promote the reduction of the metals. The electrons are provided by the semiconductor, which results in the deposition of the newly reduced atoms onto its surface.

As demonstrated by the Choi group[42], this procedure is extremely versatile, and can be employed for many widely used co-catalysts such as gold, silver, and platinum. In the experiment, these salts were photodeposited onto the surface of TiO_2 for use in a photocatalyzed HER.

Electrodeposition

Like photodeposition, electrodeposition involves a solution of the already formed catalyst and an ionic form of the proposed co-catalyst. In an experiment run by the Anicai group, TiO_2 was coated with silver nanoparticles by using what is referred to as a "sacrificial anode" setup[36]. In the experiment, TiO_2 nanoparticles were dispersed into a solution along with a stabilizer. The solution participated as an interface between two silver electrodes. A current was generated, activating a migration of TiO_2 to the surface of the anode. Meanwhile, the stabilizer interacted

with silver ions near the surface of the anode in order to keep them in solution as ionic silver.

Once TiO_2 interacted with silver, it was able to be reduced on the surface leaving behind silver nanoparticles. While this method was shown to be effective for depositing silver on TiO_2, it has not been demonstrated to be a universally applicable procedure for any metal on a semiconductor. Another issue with this method is that it is not scalable, requiring very small quantities of a semiconductor to react.

1.6 – Previous Work

Previous work done by SeyyedAmirhossein Hosseini with my help as an undergraduate research assistant expanded the applications of nickel tungstate as a photovoltaic material by doping it with copper and also by coating it in graphene. Each of these techniques were aimed at enhancing the electronic properties of the semiconductor to increase charge carrier density and improve charge carrier lifetime. This was intended to take a relatively poor performing material and enhance it through small modifications. All reactions for $NiWO_4$ and its analogues were performed through coprecipitation, with the addition of a hydrothermal step[58].

1.6.1 – Copper Doped $NiWO_4$

Copper doped $NiWO_4$ was synthesized by adding stoichiometric ratios of Ni^{2+} and Cu^{2+} ions to a WO_4^{2-} solution. Proper ratios of copper and nickel on the surface of the crystal was confirmed by X-Ray Photoemission Spectroscopy (XPS analysis and integrating the peaks of the respective electrons. Below is a table of the values for each atom in the crystal:

Table 1: XPS defined elemental ratios on surface of copper doped $NiWO_4$

Sample	Ni	W	O	Cu	Cu/Cu+Ni
3% Cu	16.4	16.3	66.7	0.5	0.03
6% Cu	15.13	16.8	67.2	0.966	0.06
9% Cu	15.57	16.5	66.2	1.73	0.10

As shown in Table 1.1, proper elemental ratios of Ni and Cu appeared on the surface, indicating that proper ratios must also be dispersed throughout the inside of the material as well. In other words, there is no excess copper or nickel forming their own species on the surface of the tungstate. Furthermore, the oxygen peaks were slightly shifted from their expected values, which is possibly due to the different environments of oxygen bound to copper vs. oxygen bound to nickel. Transmission Electron Microscopy (TEM) analysis of the samples also showed a crystalline nano-sized structure for the particles as shown in Figure 9.

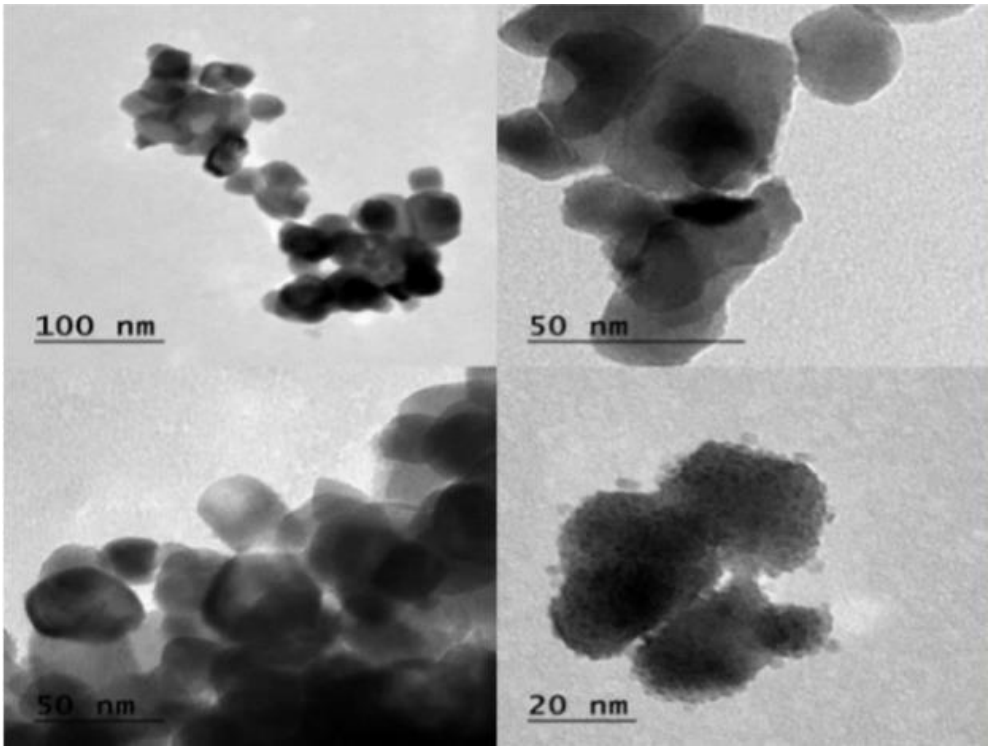

Figure 9: TEM images of copper doped nickel tungstate

Along with TEM analysis to assess the size and morphology of the particles, XRD was done to give a more definitive analysis of the crystallinity:

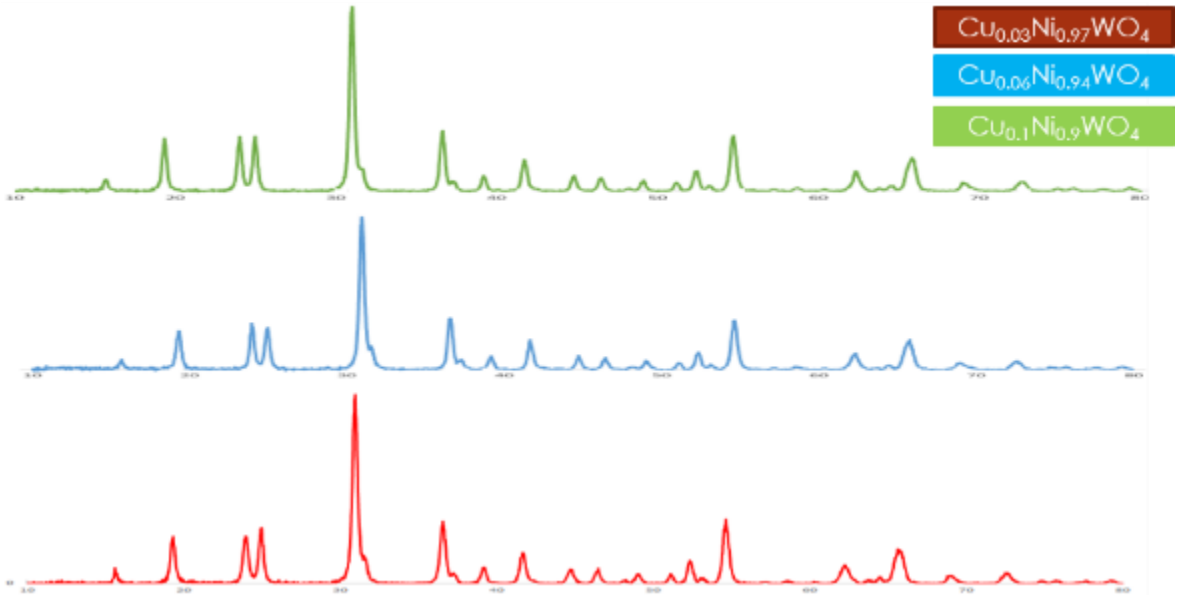

Figure 10: XRD analysis of copper doped $NiWO_4$

It was shown that the Cu did not heavily disrupt the structure of the $NiWO_4$, though shifts in peaks could be attributed to the replacement of nickel atoms with copper, similar to the oxygen peak shifts experienced in XPS.

With a confirmation of the structure and morphology of the particles, it was possible to perform a photovoltaic experiment on them to assess the effect of the copper on the charge carrier lifetime and density.

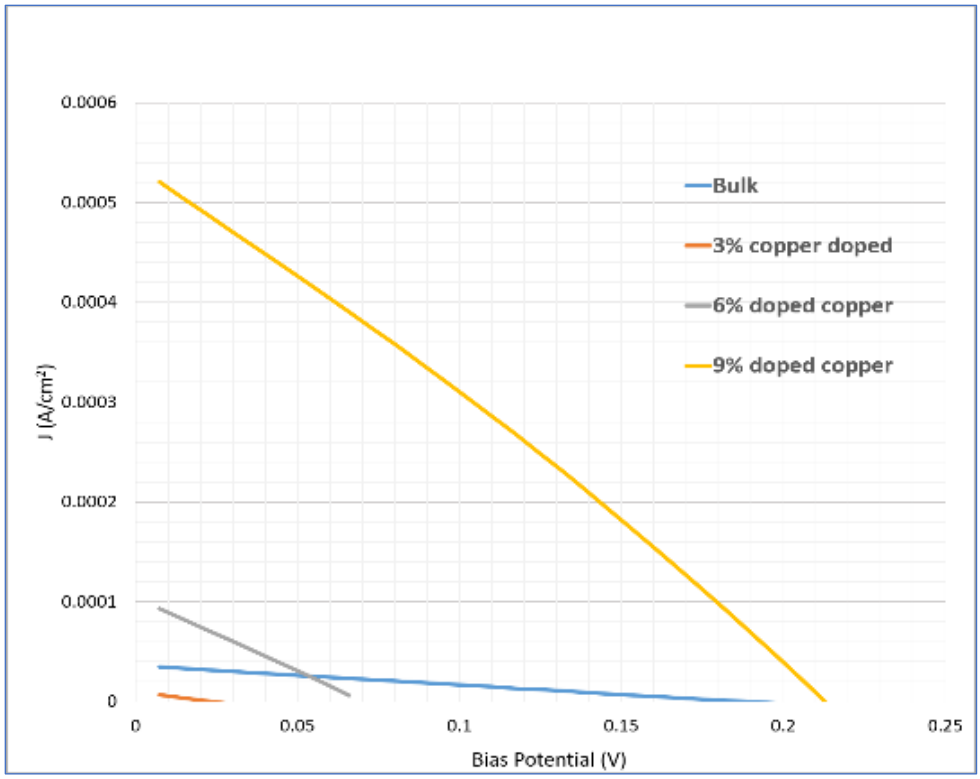

Figure 11: Photovoltaic experiment with copper doped $NiWO_4$

An I-V curve was created under a solar light simulator to explore the power conversion efficiency (PCE) of each cell created for the tungstate materials. Table 2 summarizes the PCE:

Table 2: PCE of copper doped $NiWO_4$ based solar cells

Sample	I_{sc} (mA)	V_{oc} (mV)	Efficiency
Pure $NiWO_4$	0.08	118	0.15%
3% Copper	0.06	35	0.07%
6% Copper	0.1	65	0.21%
9% Copper	0.52	210	0.86%

The equation to determine PCE is shown below, where FF represents fill factor and η represents PCE:

$$\eta = I_{SC} * V_{OC} * FF$$

Fill factor can be affected by many parameters and is often an assessment of the cell's quality[59], rather than the properties of the nanomaterials under study. Fill factor is found by drawing the largest square under the I-V curve and finding where that square intersects the x and y axis. The squarer the curve is, the better the fill factor. In the case of the I-V curves generated for the copper doped samples, they are practically linear and thus have a very small fill factor. This results in a low PCE.

It was found that the higher the concentration of copper in the $NiWO_4$, the higher the PCE. It was explained the copper is very willing to donate an electron to the conduction band in order to relieve strain caused by Jahn-Teller distortion. In lower concentrations, however, copper may be scavenging electrons and reducing charge carrier concentration, resulting in a lower PCE. With the higher concentrations of copper, this distortion allows for a higher concentration of charge carriers and thus a higher number of electrons completing the circuit even though the band gap of the material was unchanged. The band gap properties were determined by UV-DRS.

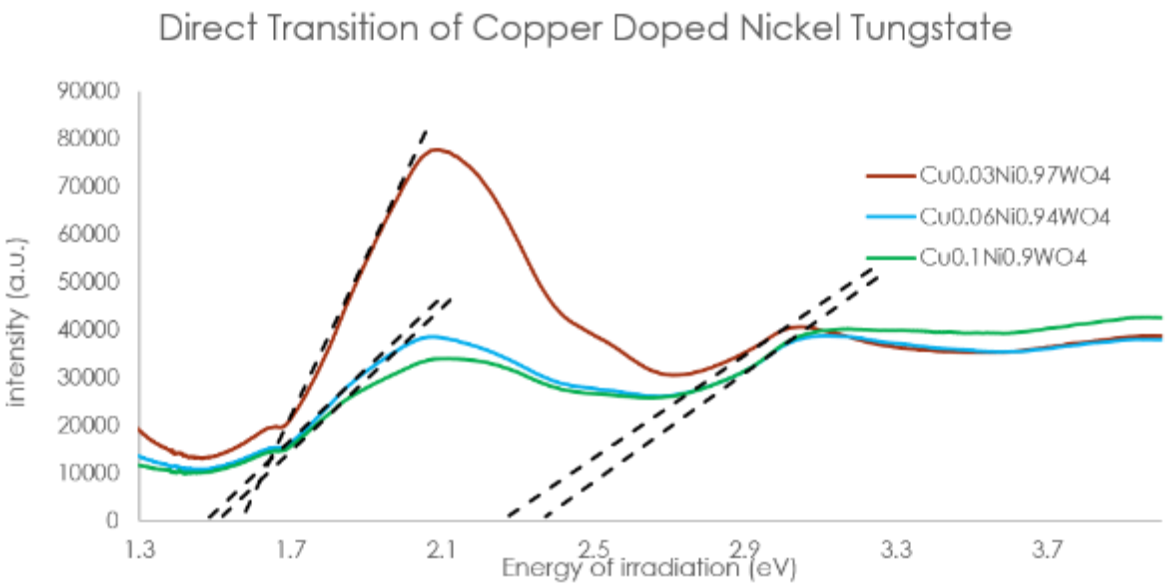

Figure 12: UV-DRS of copper doped $NiWO_4$

For the solar cell study, the reduction of PCE at 3% doping was explained by the copper atom's tendency to scavenge for electrons, rather than donate them at low concentrations. Dopants changing their properties at varying concentrations is a well known phenomenon[11].

With the success of doping $NiWO_4$ with copper to show greatly increased photovoltaic performance, an investigation to the effect of other group 11 elements in $NiWO_4$ was performed. Two experiments aimed to investigate the role of a group 11 dopant, one with a larger atom, silver, to see the size and oxidation state limits of doping $NiWO_4$. The other experiment looked at doping $ZnWO_4$, another high performing material, with copper to investigate the size dependency and dopant type (p vs. n) on performance.

2 – Synthesis of Group 11 Element Doped Metal Tungstates

For the purposes of this study, a coprecipitation synthesis of metal tungstates was chosen. This was chosen in part for its low cost and quick yield when dealing with small volumes. Furthermore, as a coprecipitation reaction is the common method for the synthesis of tungstates, it may yield the ability for cross-sectional analysis of the properties of the products when compared to literature.

The materials used include: **$Na_2WO_4 \cdot 2H_2O$ (95%)** from Alfa Aesar, **$Ni(NO_3)_2 \cdot 6H_2O$ (98%)** from Alfa Aesar, **$AgNO_3$ (Certified ACS)** from Fisher Scientific, **$Zn(NO_3)_2$ (Certified ACS)** from Fisher Scientific, **$Cu(NO_3)_2$ (Certified ACS)** from Fisher Scientific, **Sodium Dodecyl Sulfate (ACS reagent ≥99%)** from Sigma-Aldrich, **Methylene Blue, (high purity, biological stain)** from Alfa Aesar, **MilliQ water**, and **Ethyl Alcohol (160 proof, Pure)** from Sigma-Aldrich.

2.1 – Bulk Synthesis of $NiWO_4$

Initially, 0.0015 moles of sodium Na_2WO_4 was measured out to 0.4948g. This was dissolved in 20mL of Millipore water, and allowed to stir until completely dissolved forming a 0.075M solution. A corresponding amount of nickel nitrate, 0.4362g, was measured and put into a separate beaker of 25 mL and allowed to stir forming a 0.06M solution. After both beakers were allowed to stir until complete dissolution, the nickel solution was added immediately and completely to the tungstate solution.

A cloudy precipitate of mint green color was formed within 5 seconds, and solution was stirred for 30 minutes to ensure a complete reaction. The precipitate was then centrifuged multiple times a 1:1 mixture of ethanol and water at 3k RPM for 10 minutes each cycle 3 times.

The washed nickel tungstate was dried in acetone overnight at 90℃. After this, the sample was annealed in atmosphere at 550℃ for 5 hours. The mint green precipitate transitioned to a dull grayish-tan after sintering.

2.1.1 – Hydrothermal Synthesis of $NiWO_4$

The hydrothermal synthesis of $NiWO_4$ is nearly identical to that of the bulk synthesis, with the addition of a heating step. After the precipitation reaction, the solution was transferred to a hydrothermal reactor and heated at 190°C for 24 hours. Subsequent steps are identical to the bulk synthesis.

2.1.2 – Copper Doping of $NiWO_4$

Copper doping of $NiWO_4$ involved a coprecipitation of a stoichiometric ratio of WO_4^{2-} ions with Ni^{2+} and Cu^{2+} ions. This coprecipitation took place in an aqueous solution as described in Section. 1.6.1.

2.1.3 – Silver Doping of $NiWO_4$

Silver doping of $NiWO_4$ was carried out through a coprecipitation method with silver ratios of 2x:1-x:1 of $Ag(NO_3):Ni(NO_3)_2:Na_2WO_4$, where 'x' represents the % of doping. Sodium dodecyl sulfate (SDS) was used as an anionic surfactant. A general frame of this synthesis was kept consistent throughout all experiments, though many factors were changed between each sample. The synthesis involved two initial solutions, one which contained Na_2WO_4 and SDS in a round bottom flask, and one which contained the $Ag(NO_3)$ and $Ni(NO_3)_2$ with or without

additional SDS. Both of these solutions were stirred and sonicated for several minutes in order to assure dispersion. Finally, the Ag^{+}/Ni^{2+} solution was added to the WO_4^{2-} flask and was stirred for 30 minutes.

Following complete reaction, the solution was washed via centrifugation at 3k RPM for 10 minutes. At least three cycles were carried out with a 1:1 ratio of H_2O:EtOH, though depending on the SDS concentration used, additional cycles were performed until SDS bubbles were no longer forming in the supernatant liquid. The sample was then suspended in acetone and dried at 80℃ overnight. The dried sample was then crushed in an agate mortar and pestle, and calcinated for 5 hours at a temperature between 230℃ and 550℃. Below is a table of various trials which have been performed and the parameters of the experiment. Multiple levels of doping may have been studied in each batch.

Table 3: Concentrations of SDS used in cationic and anionic solutions for synthesis of silver doped $NiWO_4$

Batch	[SDS] in WO_4^{2-} (mmol)	[SDS] in cation (mmol)	Calcination Temperature (°C)
1	0	0	230
2	120	0	230
3	120	0	550
4	120	6	230
5	120	6	550
6	0	0	550
7	120	10	380

2.2 – Bulk Synthesis of $ZnWO_4$

Stoichiometric amounts of $Zn(NO_3)_2$ and Na_2WO_4 were measured. Initially, the Na_2WO_4 was dissolved in a 20mL solution of 2:1 water:ethanol, along with 50mg of SDS. The solution was stirred for 10 minutes, and then transferred to a sonication bath. The sonication was set for 30 minutes, at which time the $Zn(NO_3)_2$ was added to the flask and left to react. Following sonication, the resulting precipitate was washed, dried, and calcinated with the standard procedure outlined in the $NiWO_4$ synthesis.

2.2.1 – Copper Doping of $ZnWO_4$

Doping of $ZnWO_4$ with copper was performed through a hydrothermal synthesis involving the coprecipitation of a stoichiometric ratio of Cu^{2+}/Zn^{2+} and WO_4^{2-} to form Cu_x-$Zn_{1-x}WO_4$. The WO_4^{2-} ions were dispersed in 25mL of this solution, along with 50mg of SDS. In a separate beaker, the Cu^{2+} and Zn^{2+} ions were dispersed in 5mL of the mixture. After the SDS/WO_4^{2-} solution was allowed to stir and completely disperse for 15 minutes, the Cu/Zn solution was added instantaneously to the anionic solution. This resulting mixture was allowed to stir for 30 minutes, and then transferred to a hydrothermal reactor where it was heated to 190℃ for 24 hours. Following the heat treatment, the nanoparticles were washed in a 1:1 mixture of H_2O:EtOH at 3k RPM for 10 minutes. This washing procedure was repeated 3 times. The nanoparticles were then dispersed in acetone and dried in an oven at 80℃ overnight. They were then crushed and calcinated at 550℃ for 5 hours.

It was seen that at increasing levels of copper within $ZnWO_4$, the color shifted from a pure white to a brown hue:

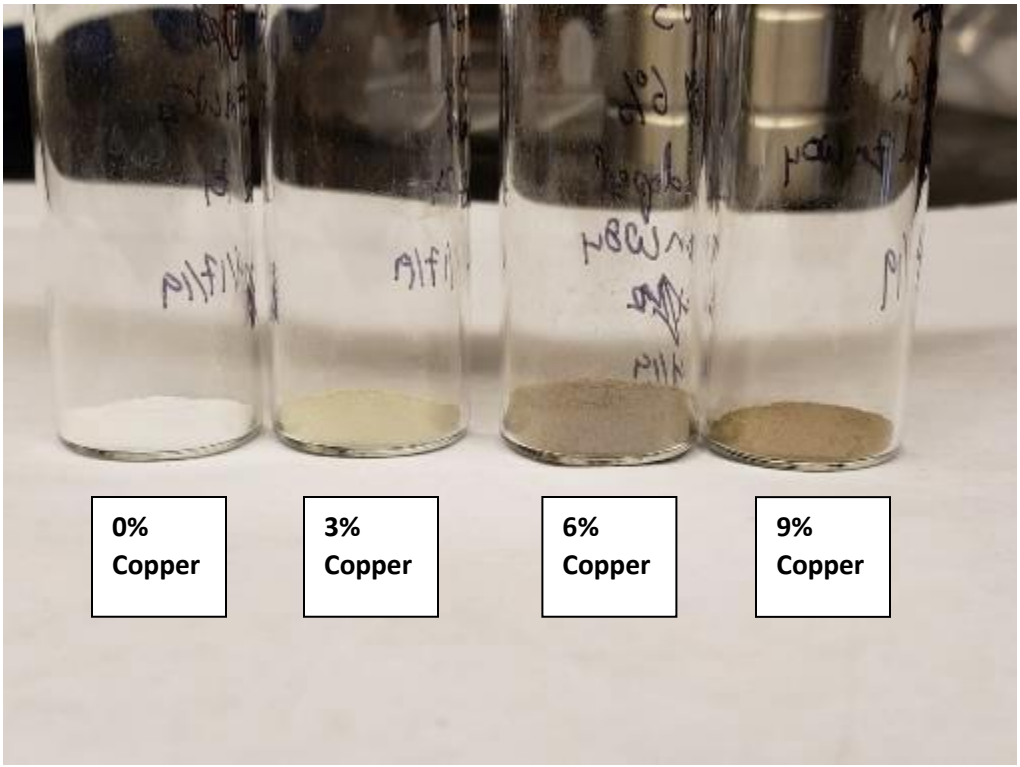

Figure 13: Color change of $ZnWO_4$ with respect to the amount of copper doping

3 – Characterization of Group 11 Modified Nickel and Zinc Tungstates

In order to confirm the structural, compositional, and electronic properties of these materials, a variety of characterization techniques were performed. For the confirmation of structural properties, Transmission Electron Microscopy (TEM) and X-Ray Diffraction (XRD) were performed. These techniques were useful to gauge both the average particle size and also the crystallinity of the samples. The compositional properties of the nanoparticles were confirmed by X-Ray Photoemission Spectroscopy (XPS) and Infrared Spectroscopy (IR). XPS and IR allowed for confirmation of surface ratios of elements for our samples, which is especially useful in characterizing the doped tungstates. UV-Diffuse Reflectance Spectroscopy (UV-DRS) was used for the analysis of the electronic properties of the samples. All analysis was done at Ball State University, with the exception of XPS, UV-DRS, and XRD, which were performed by Seyyedamirhossein Hosseini at Indiana University Bloomington and data used with permission. This data was provided by the Dennis Peters group as part of a collaboration.

3.1 – Silver Doped $NiWO_4$

Silver doping was carried out in a similar method to the doping of nickel tungstate with copper. Due to the success of previous lab member Seyyedamirhossein, there was a justification for a continuation of the project with the same methods. As will be shown in the results, doping of nickel tungstate with silver through the same methods employed for copper is not feasible, though interesting results have emerged which have potential for future studies. Figure 14 shows a flowchart which details the morphology of nickel tungstate doped with silver based on the synthetic procedure.

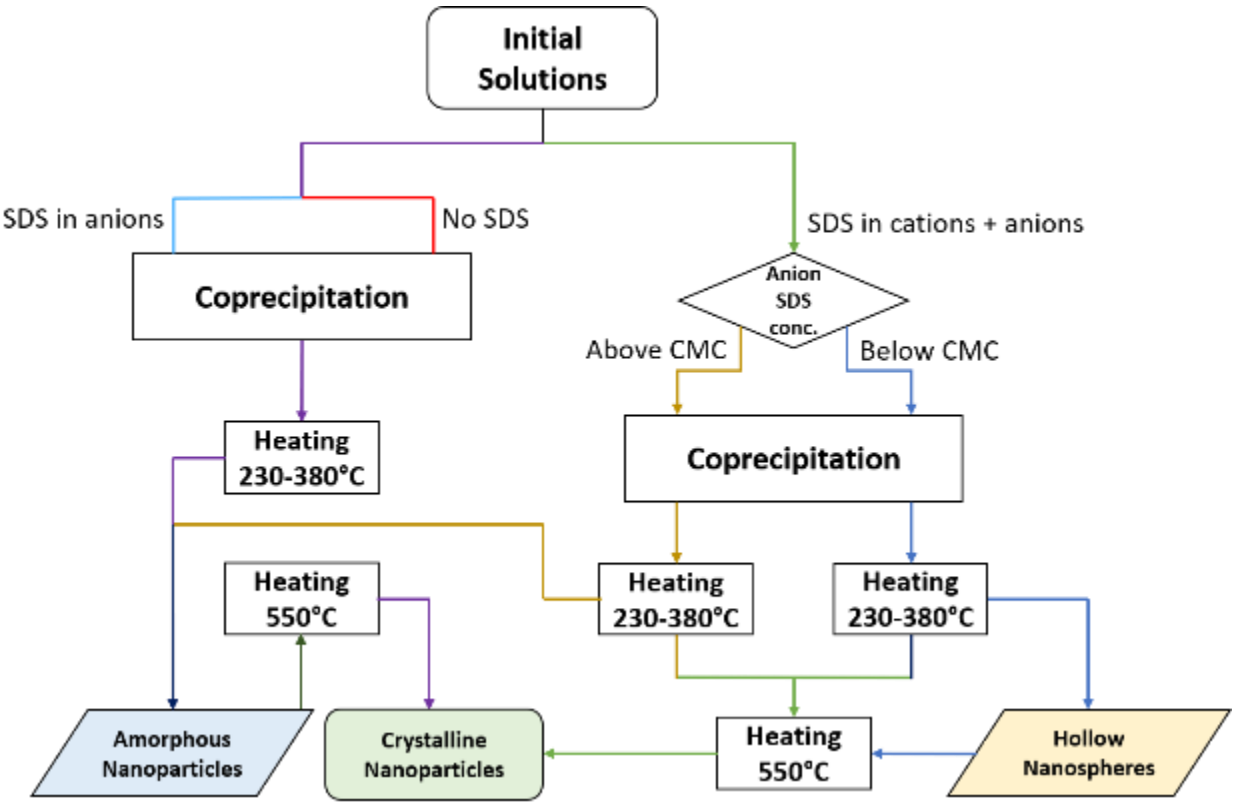

Figure 14: Scheme for synthesis of different silver doped $NiWO_4$ morphologies

3.1.1 – Hollow Nanospheres

For batch 4 described above, hollow nanospheres were formed through what is believed to be a soft-templated nucleation. The anionic head of the surfactant SDS has an affinity toward metal cations[60]. In Xie's study, hollow spheres of a similar size ~100nm were reported through a double-vesicle template formed by SDS. Below is an illustration of the proposed structure of these vesicles:

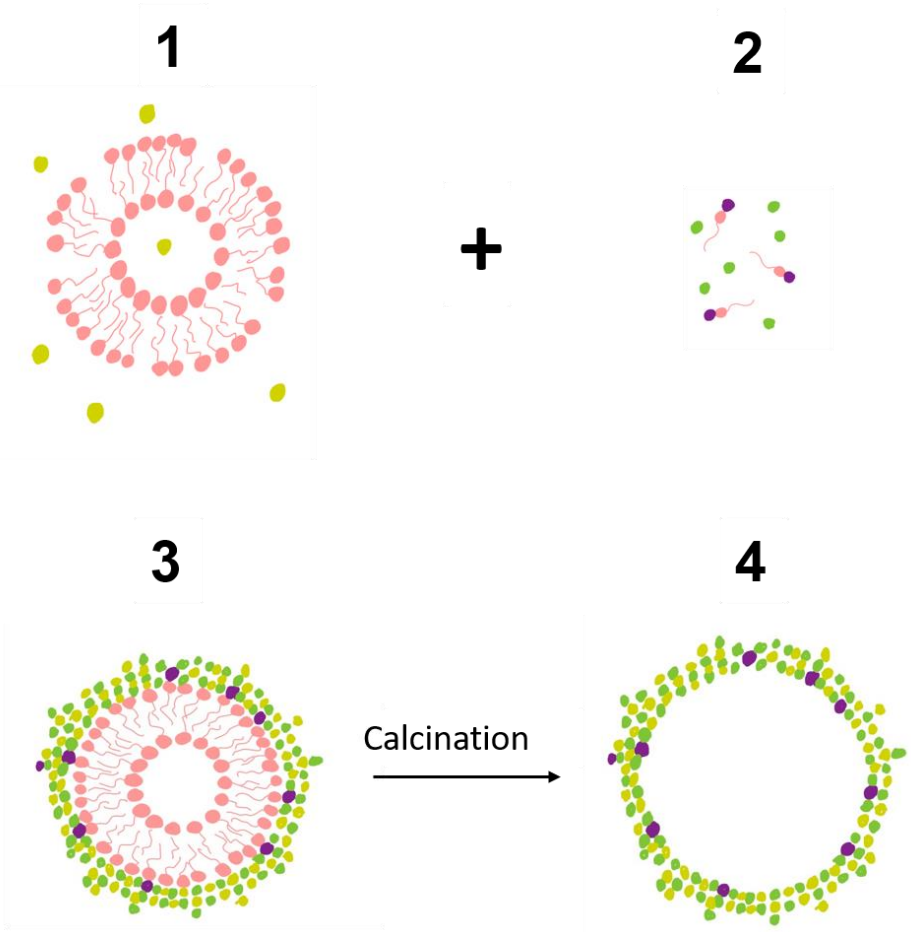

Figure 15: A double vesicle system formed by SDS in solution. Sulfate heads are hydrophilic and can interact with cations in solution to form a soft template. WO_4^{2-} is shown in yellow, SDS in pink, Ag^+ in purple, and Ni^{2+} in green.

To achieve this template, multiple preliminary steps are taken in the scope of the synthesis to ensure its formation. In the samples with confirmed hollow spheres, first silver and nickel (II) cations were dispersed in an SDS solution below its critical micelle concentration (CMC), leading to the interaction of silver and nickel with the sulfate heads. Next, the solution of SDS-complexes is added to the tungstate solution which has a concentration of SDS many times higher than the CMC. Once these double vesicles form, the tungstate ions precipitate with the silver and nickel cations still in solution to form a precipitated metal-oxide material. It is assumed that this template is decomposed upon calcinating at high temperatures, leaving behind the nanoparticles.

Figure 16 shows TEM images of the hollow spheres formed by this soft template method:

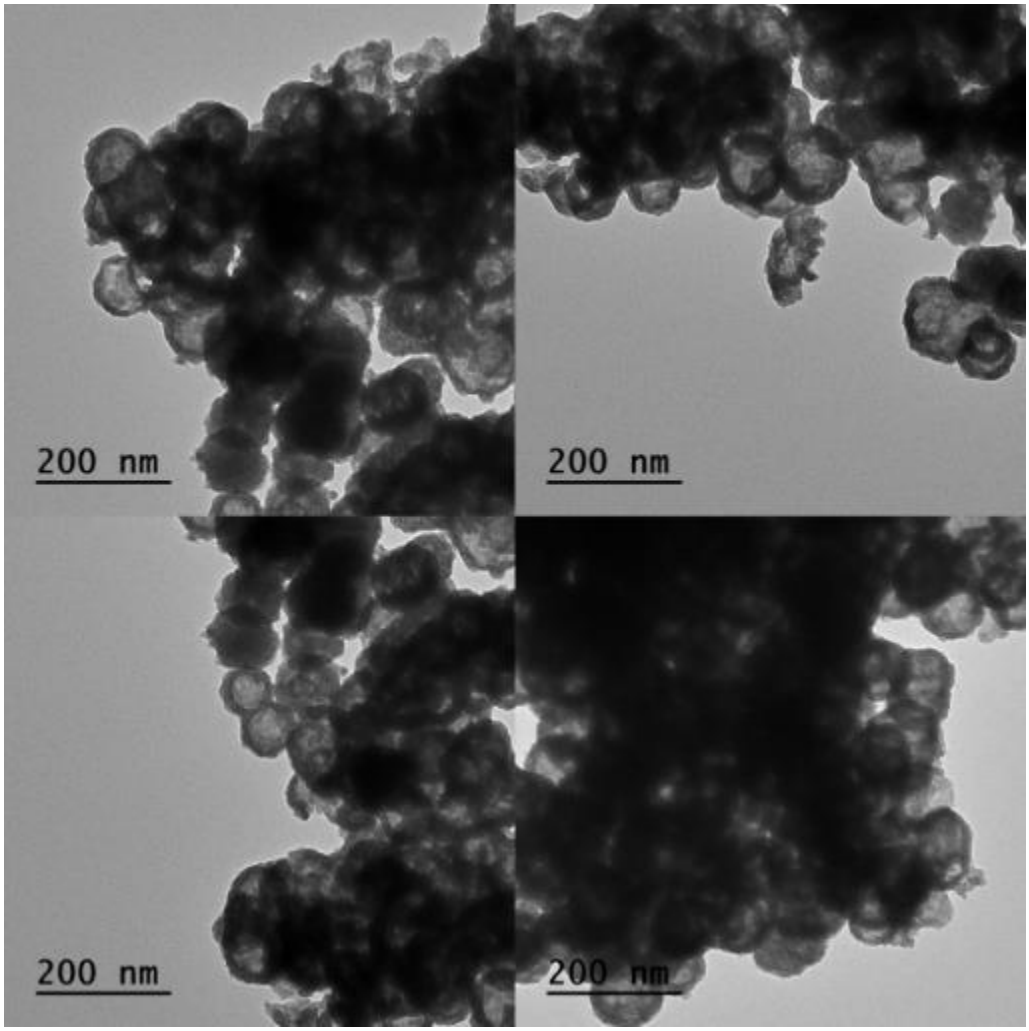

Figure 16: TEM images of batch 4, showing aggregations of hollow nanospheres ~80-120 nm in size

The dark edges but light centers of the nanoparticles are classic features of hollow bodies. While a strong argument can be made toward the spherical nature of these particles simply from TEM images, an AFM study done by Cody Leasor in the group provides further evidence to the morphology of these nanoparticles.

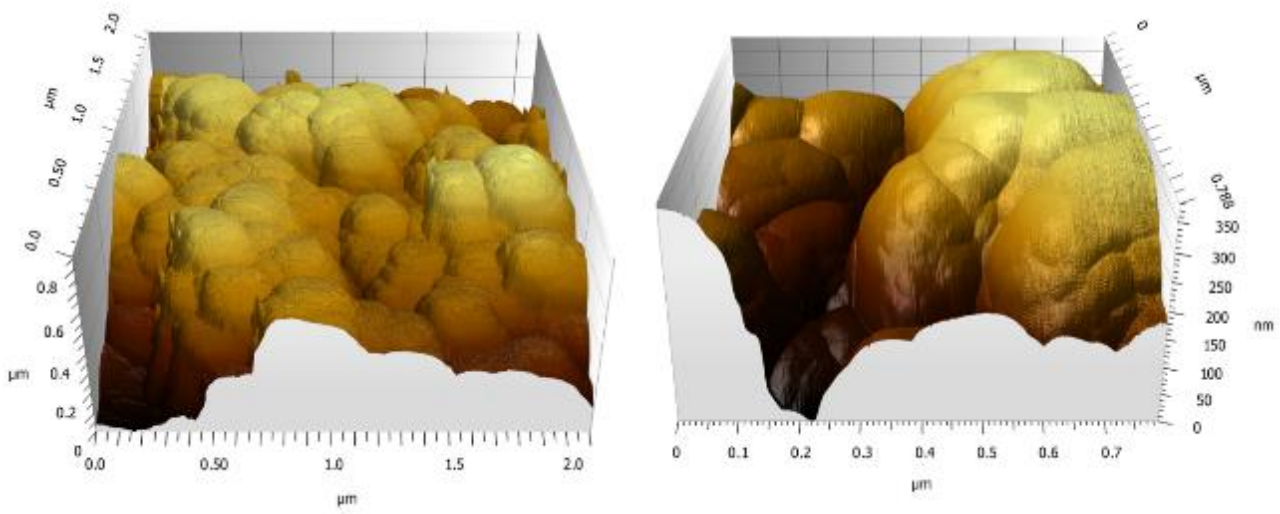

Figure 17: Acoustic AFM images of hollow nanoparticles, axes are to scale

AFM imaging of the hollow nanoparticle aggregates further demonstrates uniform size distribution, as well as relatively smooth surfaces. A complete distribution of rounded surfaces provides remaining evidence that nanoparticles are spherical in nature. XRD analysis of these hollow nanospheres shows a predicted amorphous structure:

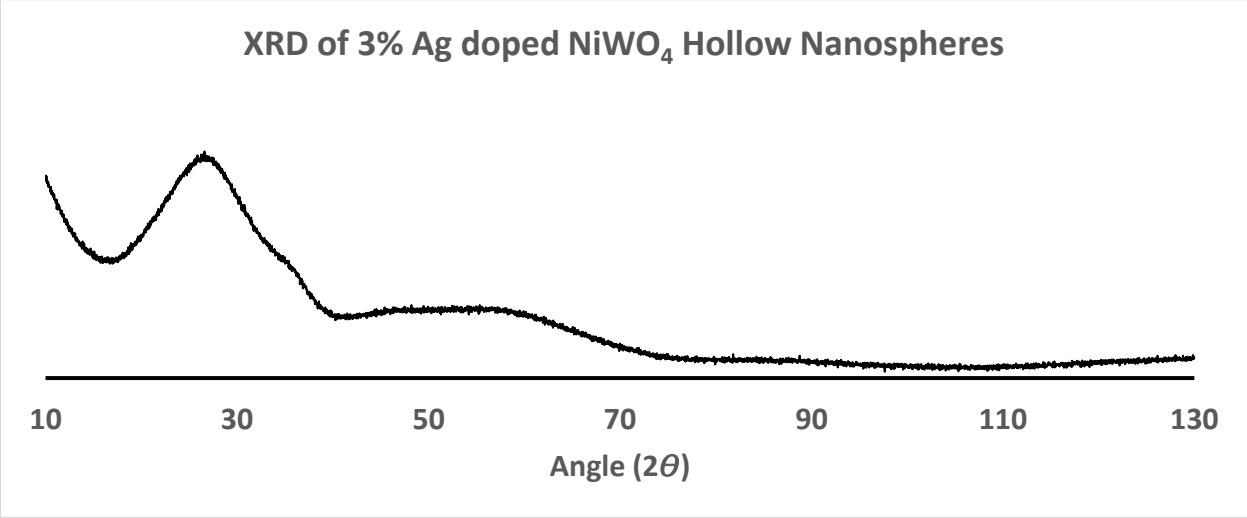

Figure 18: XRD analysis of hollow nanospheres. The nanospheres show amorphous characteristics

A series of experiments were performed on these hollow nanoparticles to observe how they form, and at what temperature they decompose. In a separate analysis performed with batch 5, under the same synthetic conditions but different calcination conditions, solid nanocrystals are

formed as opposed to hollow nanospheres. Temperatures were varied by 50 degrees C from 230-430 until decomposition of the hollow spheres occurred. Below are TEM images of each sample:

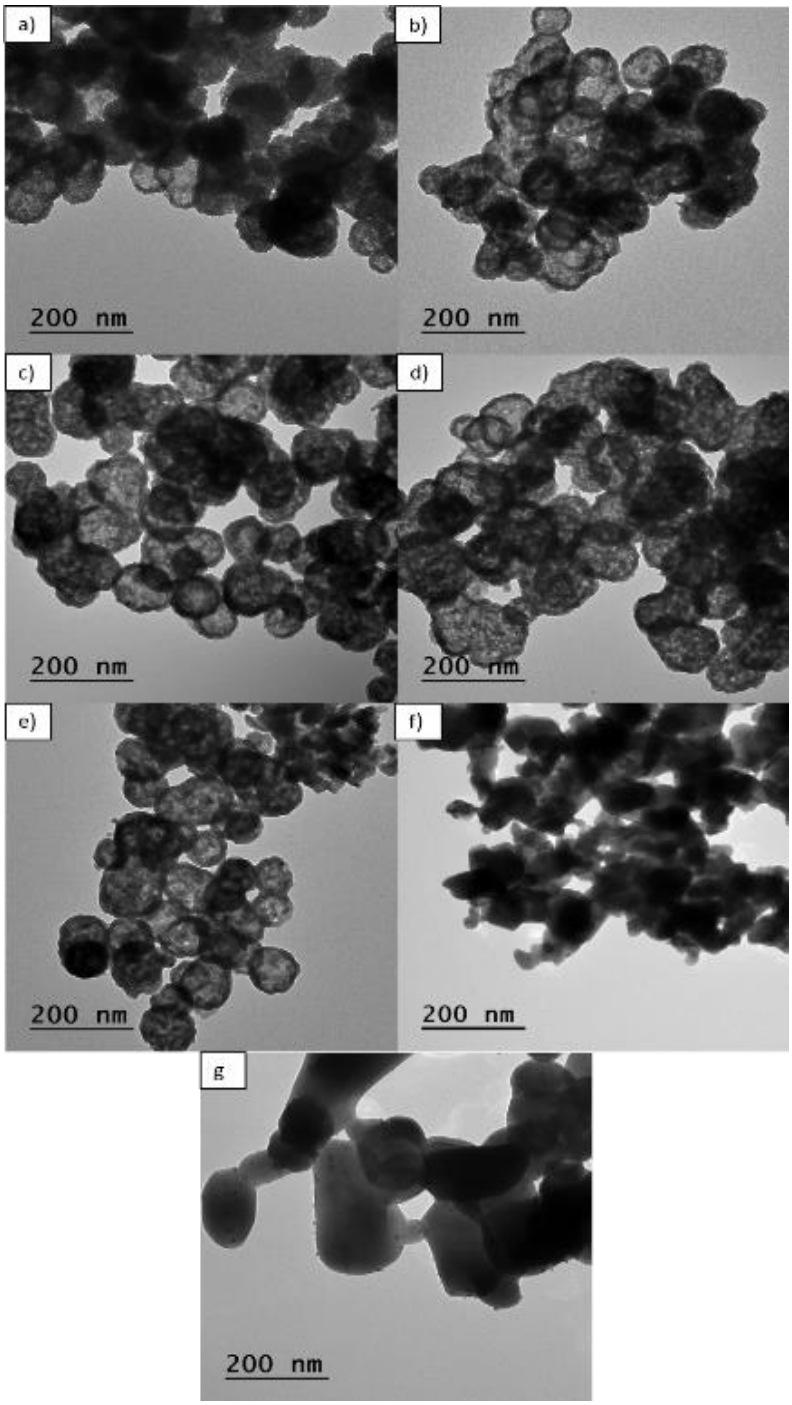

Figure 19: Silver doped nickel tungstate from batch 4. Each sample was calcinated at a different temperature: a) no calcination; b) 230°C; c) 280°C; d) 330°C; e) 380°C; f) 430°C, g) 480°C

The TEM analysis shows that hollow spheres form in solution, as opposed to part of a process activated by a large amount of external energy. One notable feature of the sample which was not calcinated is that although the hollow spheres form, they have extremely rough surfaces. This roughness disappears as higher temperatures are approached, representing the possible decomposition of Ni-OH and Ni-O on the surface. This can also be seen in the color of the samples themselves, which transition from a mint green to a sandy beige. The nanoparticles do not appear to change drastically between 230-330°C. At 380°C, an altered surface appearance can be observed in which the surface becomes less varied and the edges of the nanoparticles become more pronounced. Finally, at 430°C, collapse of the nanoparticles occurs and silver spots can be observed clearly on the surface of the new particles. These nanoparticles exhibit a wide range of shapes and sizes, which finally form larger and more uniform particles at 480°C.

An IR-spectrum was taken for each of these samples to assess the surface presence of different species and the changing of their presence with differing calcination temperatures. IR studies were performed with a Perkin Elmer Frontier FT-IR Spectrophotometer using the Universal ATR Sampling Accessory. The samples were left in an unaltered powder form.

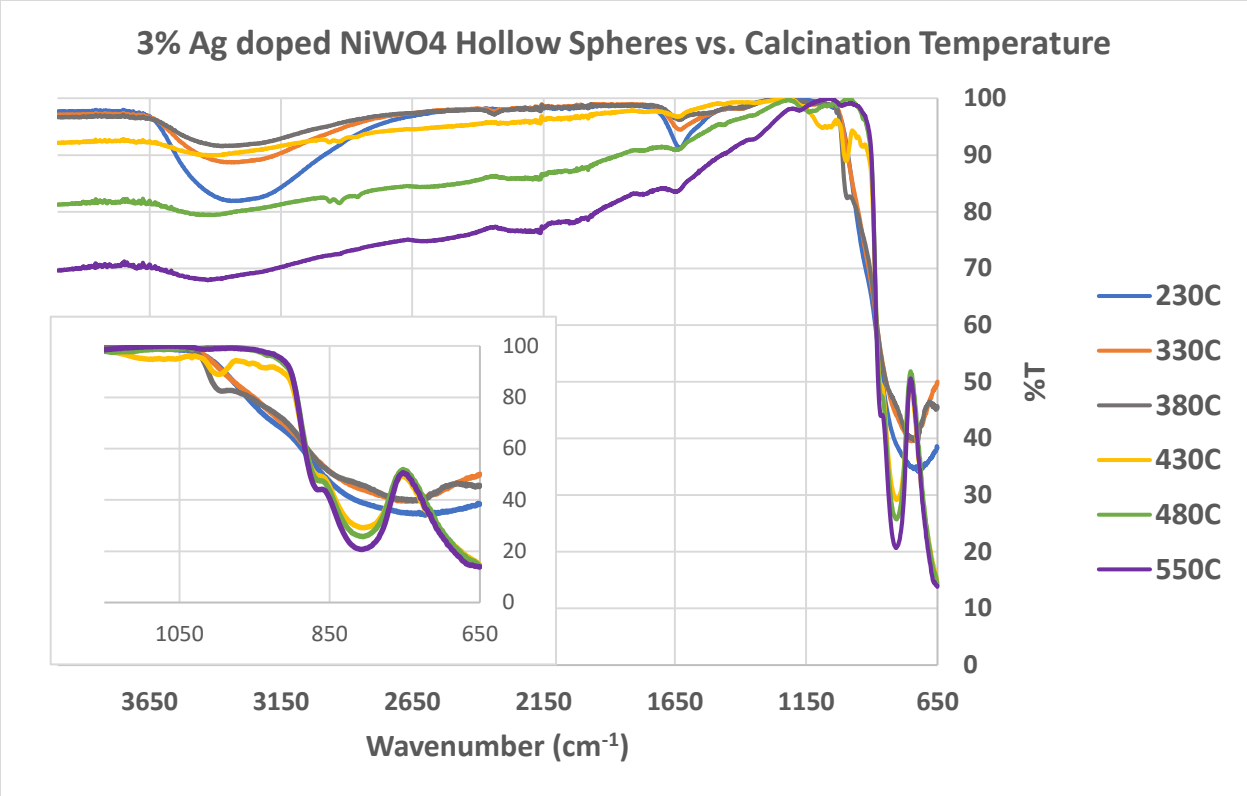

Figure 20: IR spectra of hollow nanospheres based on calcination temperatures

As shown in the TEM images previously, the hollow nanospheres persist until 430°C, and IR-spectrum (Figure 22) shows there are a few features which begin to disappear at that temperature. The O-H stretch in the IR spectra between 3000-3600 cm^{-1} can be indicative of moisture in the sample[16]. A sharp peak at 1625 cm^{-1} also corresponds to weak O-H vibrations from water. As temperature of calcination increases, the peaks associated with moisture begin to disappear. A broad peak at 730 cm^{-1} appears in samples with low calcination temperatures but disappears at higher temperatures. This is potentially a mixed state of multiple W-O-W environments between WO_4 and WO_3, which could exist at low temperatures due to incomplete coordination between nickel/silver and tungstate[21,61].

As calcination temperature increases, the band at 730 cm^{-1} begins to become less broad and develop new features, which could indicate that the metals are beginning to coordinate with

tungstate at a high enough temperature. At a threshold temperature of 430°C, sharp peaks at 810 cm^{-1} and 650 cm^{-1} replace the broad peak at 730 cm^{-1}, and the spheres collapse into crystals. The peak at 810 cm^{-1} corresponds to a W-O stretch in WO_4^{2-}, while the peak at 650 corresponds to the O-W-O vibration[16]. A peak which may be buried in the signal at 830 cm^{-1} would also relate to the O-W-O vibration. Unlike the samples between 230°C and 380°C, these bands do not change further upon more drastic heating.

A distinct peak at 999 cm^{-1} appears in two samples, which are 380°C and 430°C, which is the transition point between spheres and nanoparticles. This peak corresponds to a $(WO_6)^{6-}$ vibration[25]. In lower calcination temperatures, this peak may be buried due to the mixed state, but this peak becomes distinct only in the 430°C sample. The TEM image of this sample reveals an extremely varied environment, indicating that the sample may not be totally crystalline.

To experiment with the optimal amount of silver to form the spheres, 3%, 6%, and 9% samples were synthesized with the same procedure from batch 4:

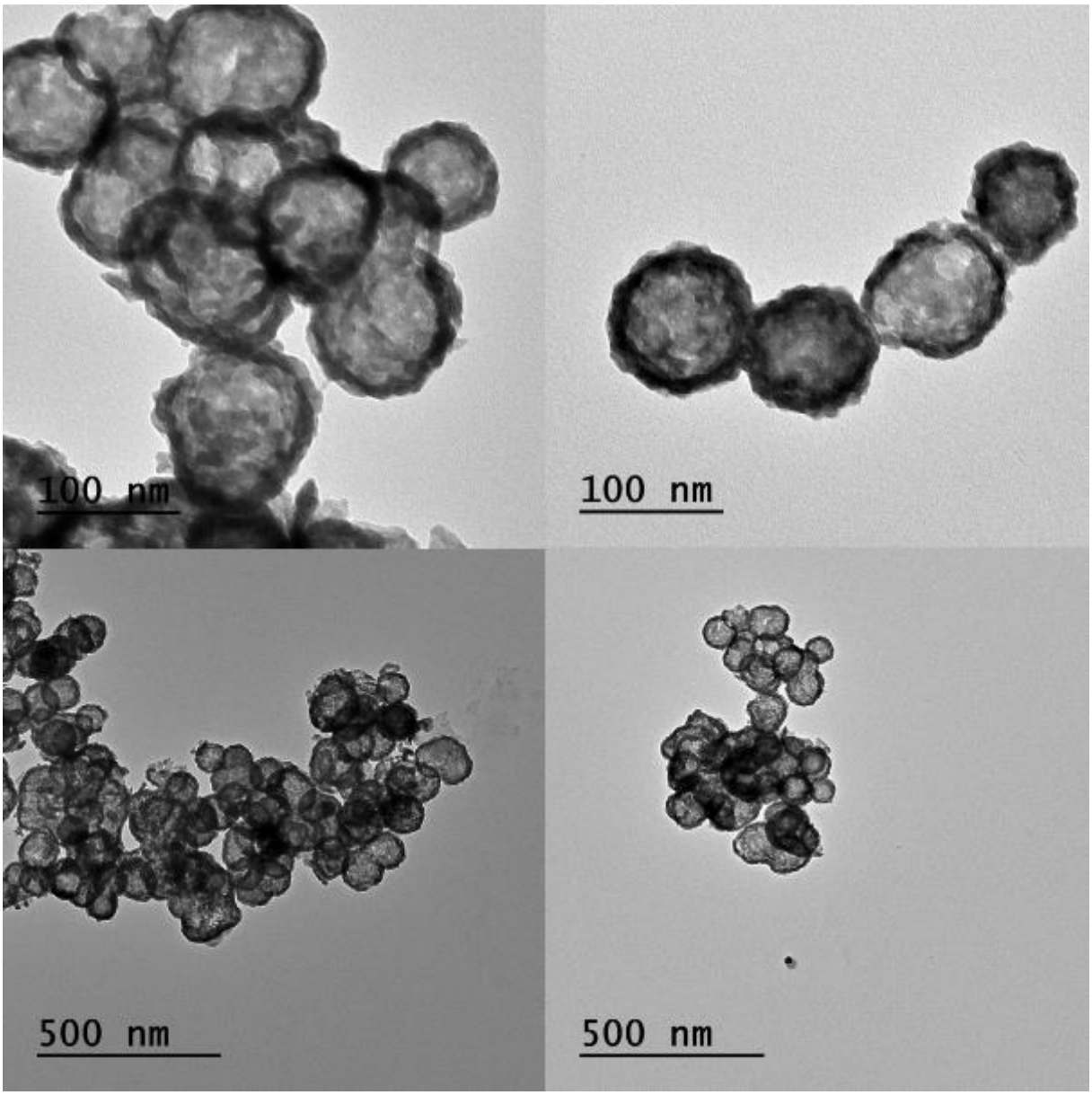

Figure 21: 3% silver doped $NiWO_4$ hollow spheres

The spheres synthesized in the 3% batch show a fairly uniform size and shape distribution, though a histogram was not created. The samples were deposited on the carbon film coated copper grids (Electron Microscopy Sciences, Carbon Film 400 Mesh-Cu) and then characterized by transmission electron microscopy (TEM, JEOL JEM-1400, 120 kV) to characterize particle shape, size and morphology for each sample below.

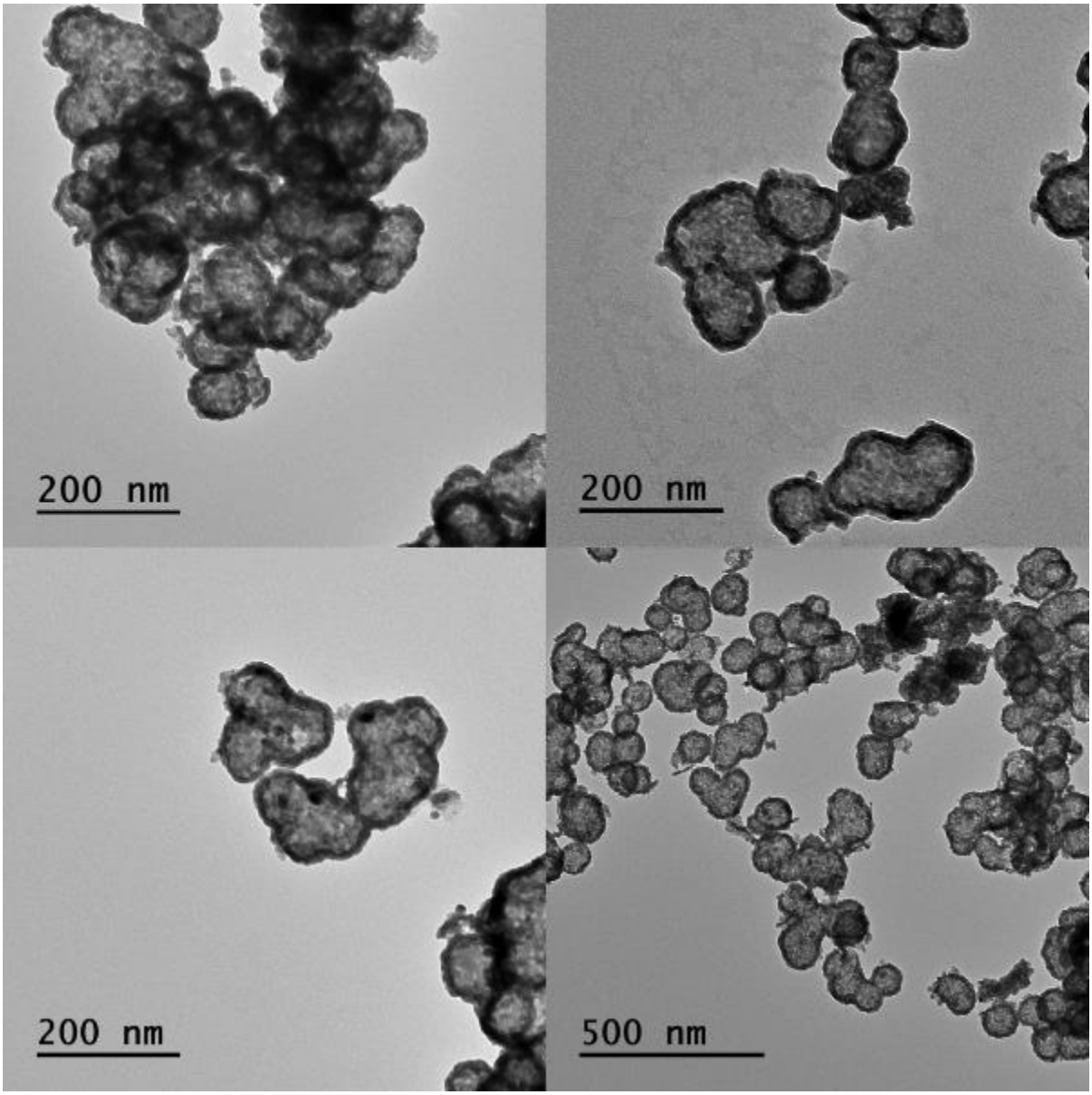

Figure 22: 6% silver doped $NiWO_4$ hollow spheres

The 6% batch begins to show signs of advanced aggregation. The 'spheres' are now more like amorphous hollow vessels, though still show rounded features as though there has been a merging of the materials. As it has been confirmed earlier that even before calcination the spheres are present, this can only have occurred during the initial mixing step, showing a

dependence on the ratio of silver to SDS in solution. This can also be confirmed by the 9% sample shown below:

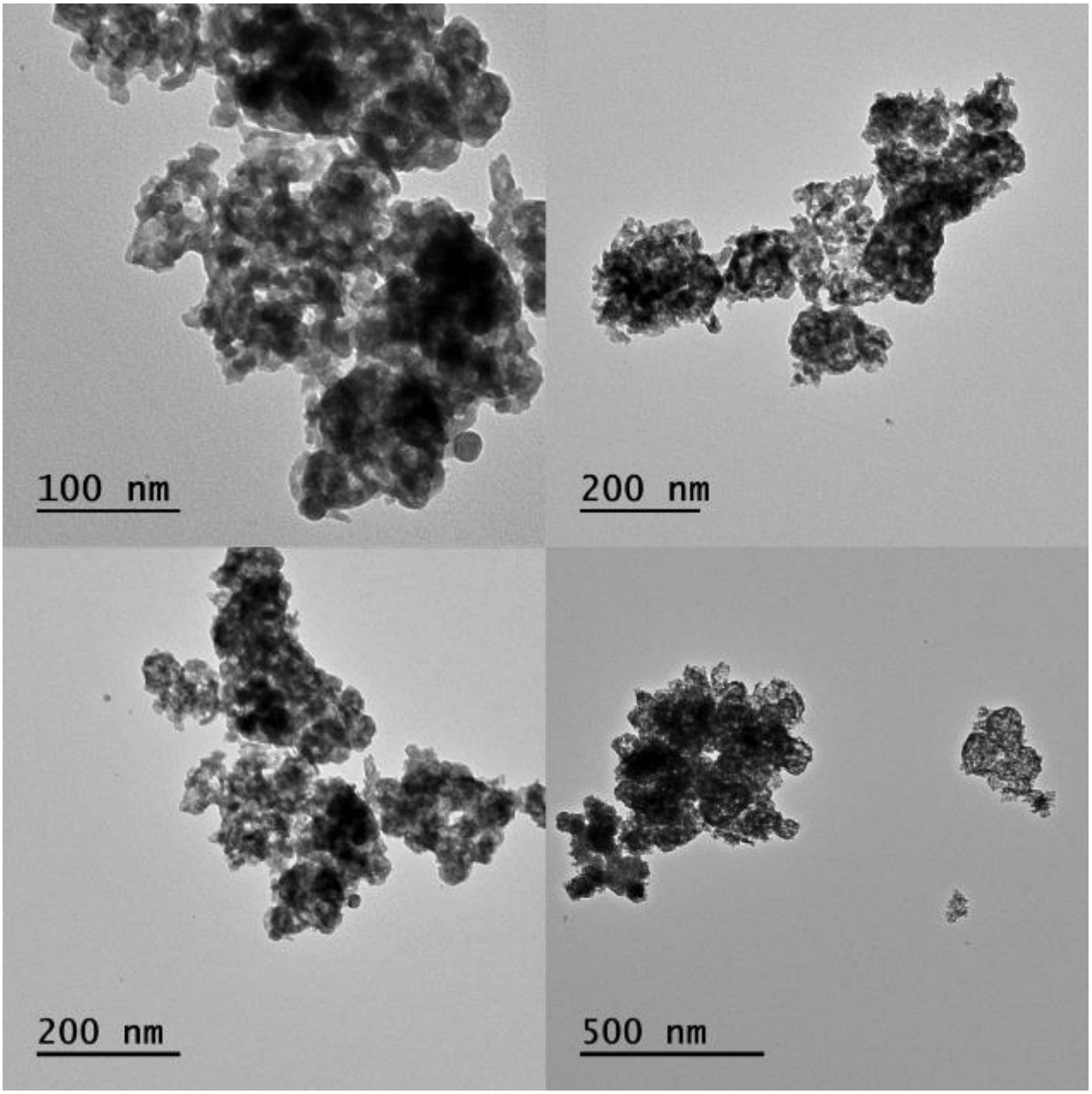

Figure 23: 9% silver doped $NiWO_4$ hollow spheres

At 9% silver addition, there is no longer a discernable shape for the nanoparticles. Certain spherical features can be made out, indicating that proto-spheres may have been beginning to form in solution, but were unstable.

With no silver, hollow spheres are not present, though with too much silver the hollow spheres also are not present. It is shown that a 3% ratio of silver to nickel is an optimal configuration for the stable formation of these hollow spheres, along with low calcination temperatures below 380°C. One reason why 0% silver may be incapable of forming hollow spheres is that nickel sulfate has a relatively high solubility in water, while silver sulfate has a relatively low solubility[62]. This would suggest that the soft template mainly coordinates with silver atoms to form a dispersed layer of silver across a double membrane of SDS. The SDS does not precipitate out of solution with silver, as it is coordinated to many other SDS molecules to maintain its stability in solution. Once this solution is added to the tungstate solution, the dispersed layers of silver on SDS can precipitate with tungstate, which also precipitates nickel in the form of a silver-nickel tungstate.

3.1.2 – Crystalline Silver Doped $NiWO_4$

While the procedure for forming crystalline silver doped nickel tungstate is identical to that of undoped nickel tungstate, the resulting crystals have an unexpected feature. As will be described later, it is suspected that under intense heating at 550°C, the greatly outnumbered silver ions are ejected from the nickel tungstate crystal in a phenomenon referred to as dopant migration. Dopant migration is a thermodynamic process which occurs when an energy barrier is crossed[63], though even mild calcination temperatures of the silver doped nickel tungstate results in a heterostructure, as illustrated in Figure 24.

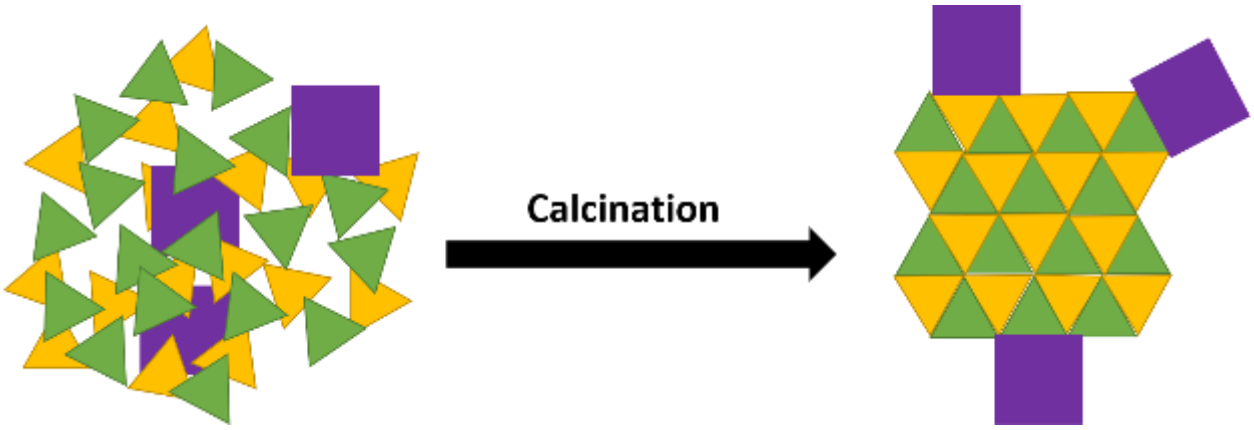

Figure 24: An illustration of dopant migration post-calcination. Yellow represents NiO groups, green represents WO_3 groups, and purple represents silver

This results in crystals which are identical to bulk nickel tungstate, but which have an additional feature as can be seen in TEM images in Figure 25.

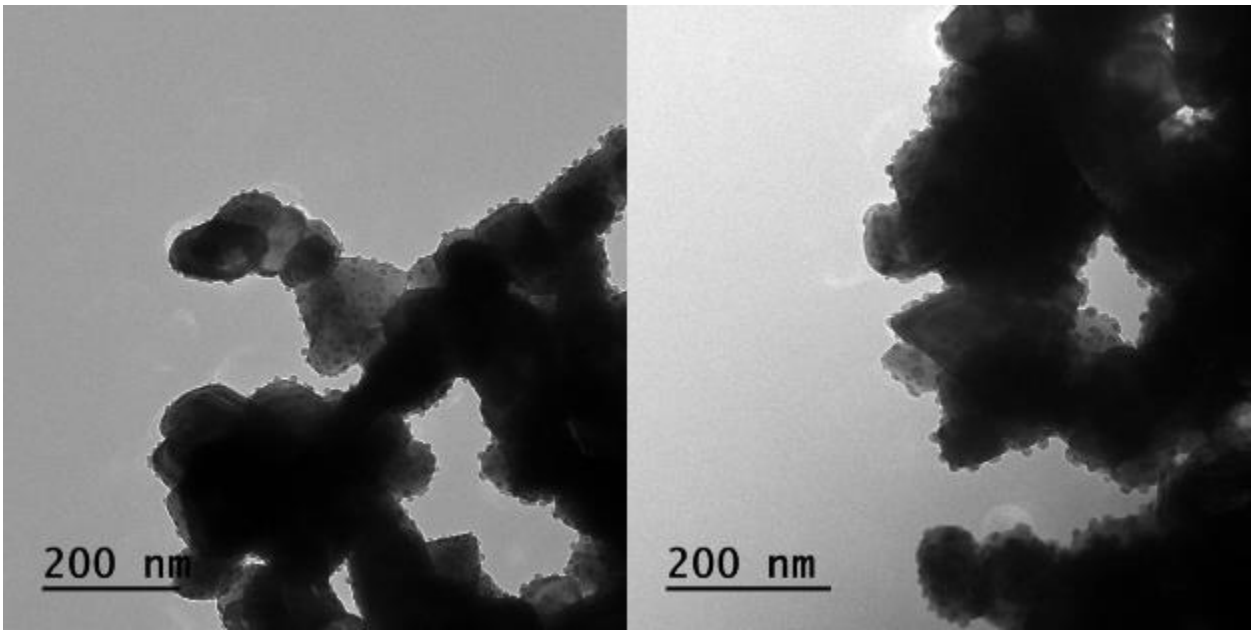

Figure 25: TEM images of batch 5 nanoparticles showing a heterostructure. Dark structures are silver on the surface of the nickel tungstates.

The structures above demonstrate a heterostructure, though TEM is not sufficient to classify the structure of these crystals. To further assess these materials, XPS was performed to look at atomic ratios of silver and nickel at the surface of the tungstate nanoparticles. In an ideal doped system, we would see an elemental ratio of 2x:1-x:1 of Ag:Ni:W. In the highest doping

amount studied, which is 9%, an elemental ratio of 16.5:83.5 of Ag:Ni would be a maximum expected value. Figure 26 shows XPS analysis of 3 samples from batch 5, and SDS assisted synthesis, showing an unusually high and unexpected presence of silver on the surface of the crystals. All data was processed through the Multi Pack software.

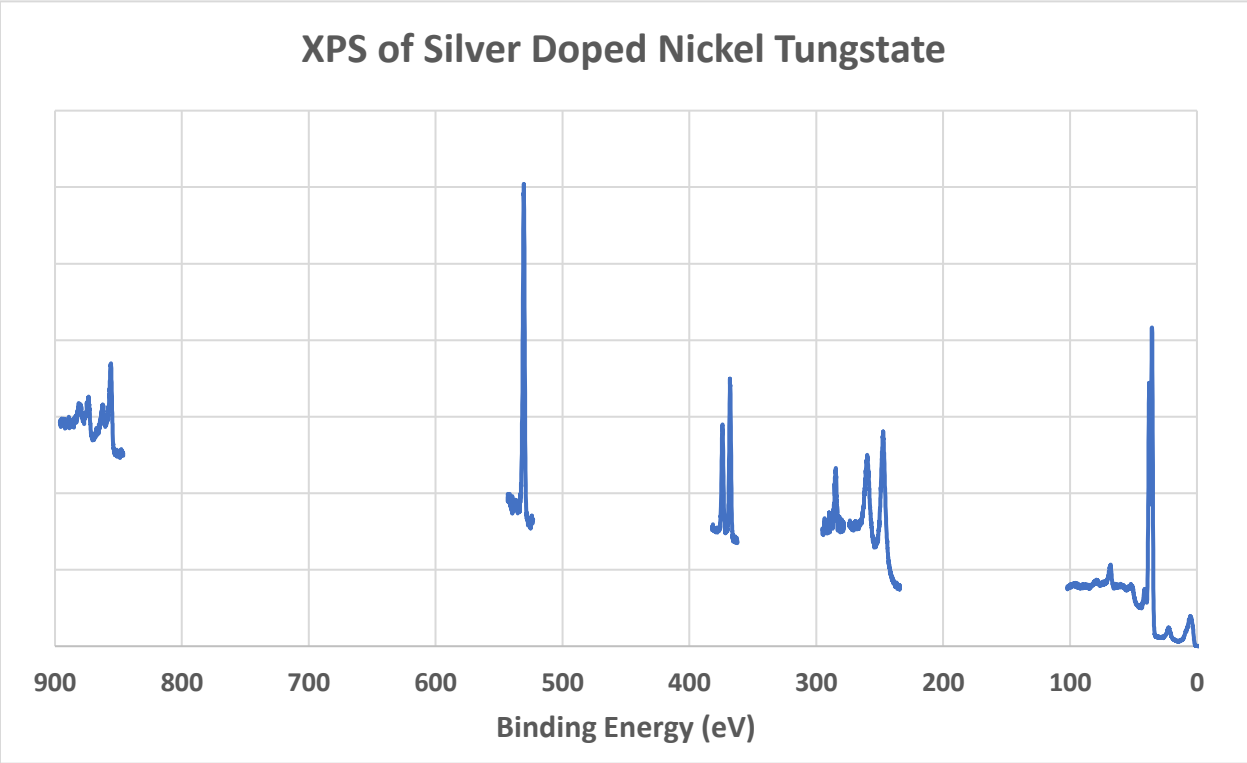

Figure 26: XPS graph showing atomic ratios of silver and nickel for 3%, 6%, and 9% silver doped nickel tungstate from batch 5.

The y-axis represents counts per second (cps), and can be considered an arbitrary unit. All values in the scan are normalized to each other, so that a baseline correction can be made to the peaks and an integration can be performed. The relative area underneath each peak allows us to assess atomic ratios on the surface of the crystals. All values for binding energy have been corrected to an "adventitious carbon" C1s value with a peak at 284.8 eV.

Table 4: XPS based elemental ratios on surface of silver doped $NiWO_4$

Doping of Silver	O1s	W4f	Ni2p	Ag3d
3%	67.97%	13.83%	14.38%	3.82%
6%	66.70%	15.43%	13.83%	4.04%
9%	65.41%	14.14%	14.19%	5.76%

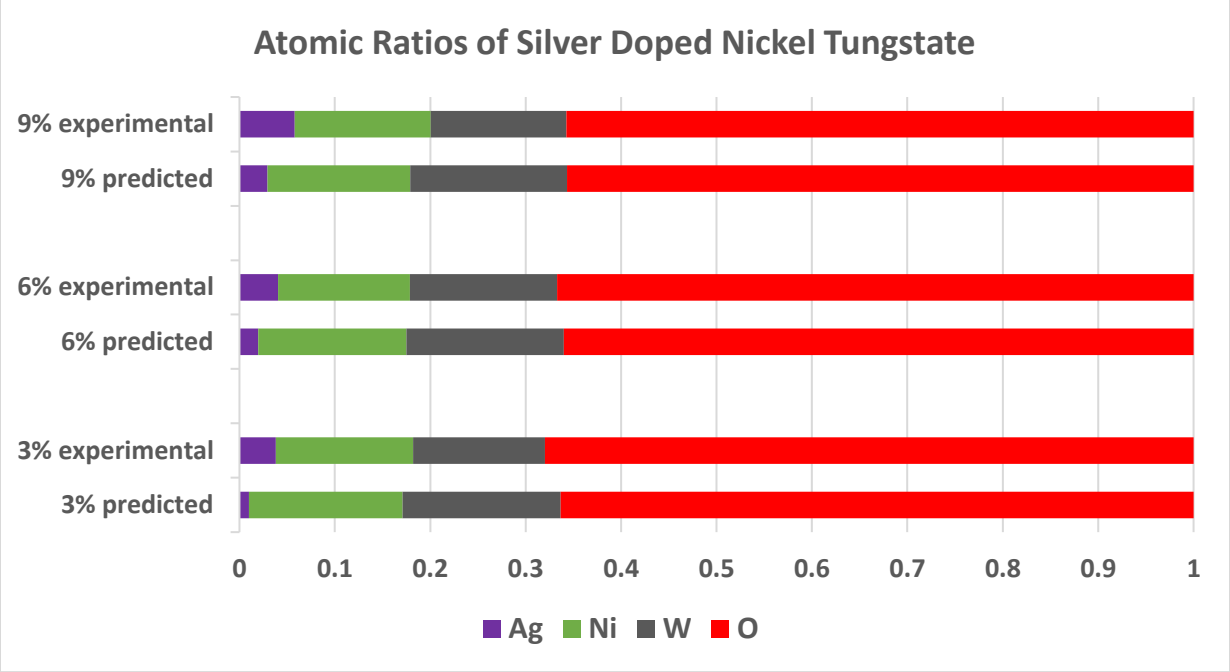

Figure 27: Relative atomic presence of elements in doped $NiWO_4$ sample

Given the high ratio of silver and nickel, while there is also an observable near 1:1 ratio of nickel to tungsten, it is more probable that silver has moved to the surface and is no longer coordinated with tungsten, instead forming metallic silver. A comparison of the ratio of silver on the surface also sheds light on the extent of the dopant migration:

Table 5: Theoretical vs. Experimental ratios of nickel and silver in silver doped $NiWO_4$

Doping of Silver	Theoretical Ni : Ag	Experimental Ni : Ag
3%	94.17 : 5.83	79.01 : 20.99
6%	88.68 : 11.32	77.39 : 22.61
9%	83.49 : 16.51	71.13 : 28.87

One additional observation which supports this possibility is the observable shift in color of the nanoparticles when exposed to light. After several hours of normal light exposure, these nanoparticles become a dull gray and sometimes purple color. This can indicate the reduction of silver by light, non-silver samples do not demonstrate this shift.

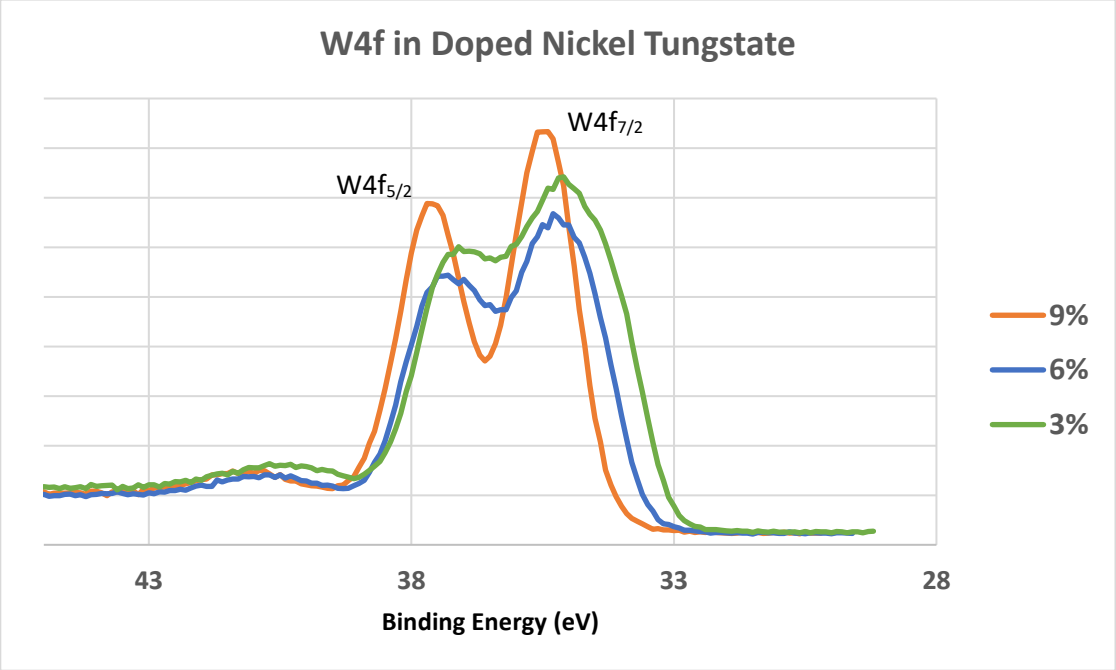

Figure 28: XPS of W4f electrons in silver doped $NiWO_4$

The W4f orbital helps assign the oxidation state of tungsten, either being W^{+5} indicating the presence of WO_3 or W^{+6} indicating the presence of WO_4^{2-}. In the cases of the 3% and 6% samples, we have a mixture of the two states, shifting the peaks to a slightly higher energy level

and filling in the gap between the peaks[64]. The W^{5+} peak is hidden beneath the W^{6+} peak, causing a distortion. In the 9% sample, two sharp symmetrical bands appear with a low valley between them. It has been noted in other studies that unreacted WO_3 can sometimes form a film on the surface of a tungstate semiconductor[61], which is what is observed in this case. As the amount of silver on the surface increases, the amount of WO_3 increases, which correlates to the lower amount of nickel in the sample able to coordinate to form $NiWO_4$. The relatively equal amount of Ni and W atoms on the surface indicates that NiO may also be present in small quantities.

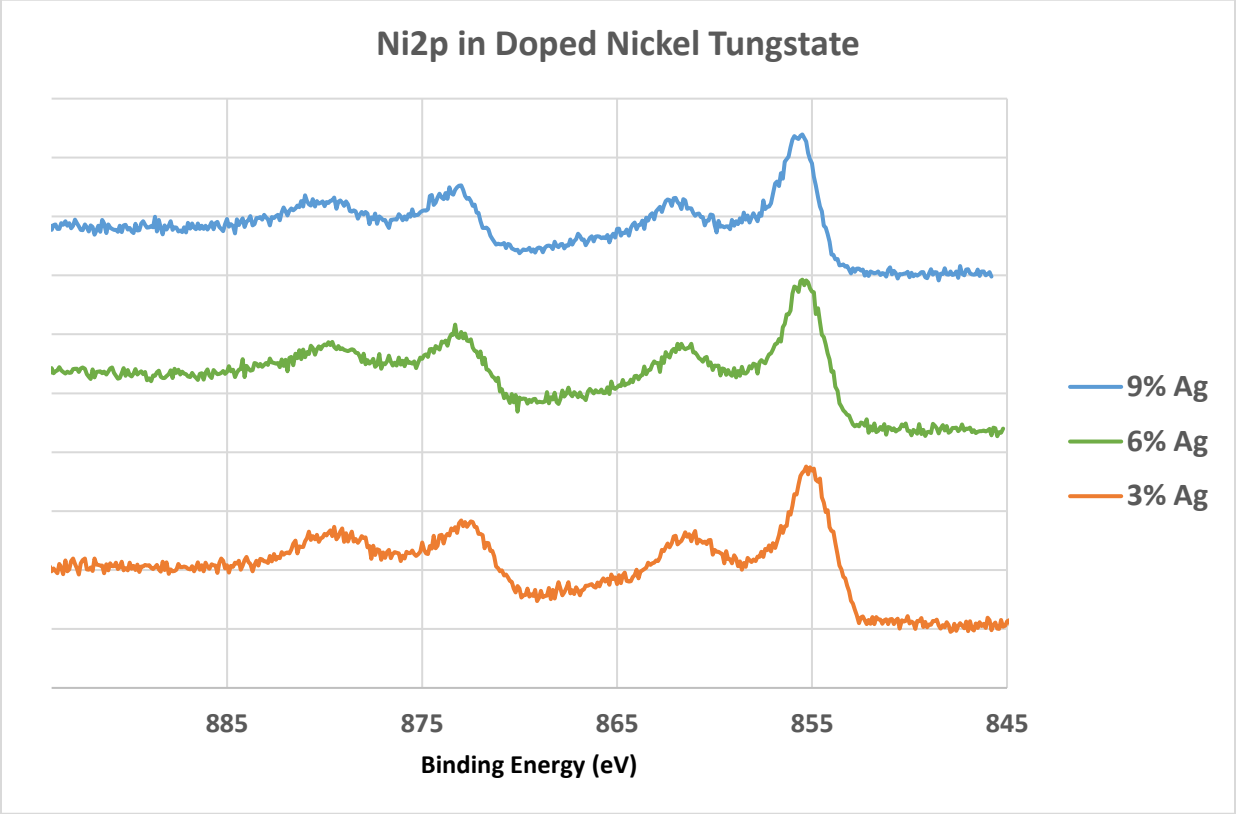

Figure 29: XPS of Ni2p electrons in silver doped $NiWO_4$

The Ni2p orbital represents the electrons responsible for coordinating with the tungstate's oxygens, and is used to compare relative abundance to tungsten. In the case of all 3 samples, the ratio of nickel to tungsten on the surface is close to 1:1, indicating a proper mixture and

formation of $NiWO_4$. A peak around 855-856 eV is consistent with literature for Ni^{2+} in tungstates[61].

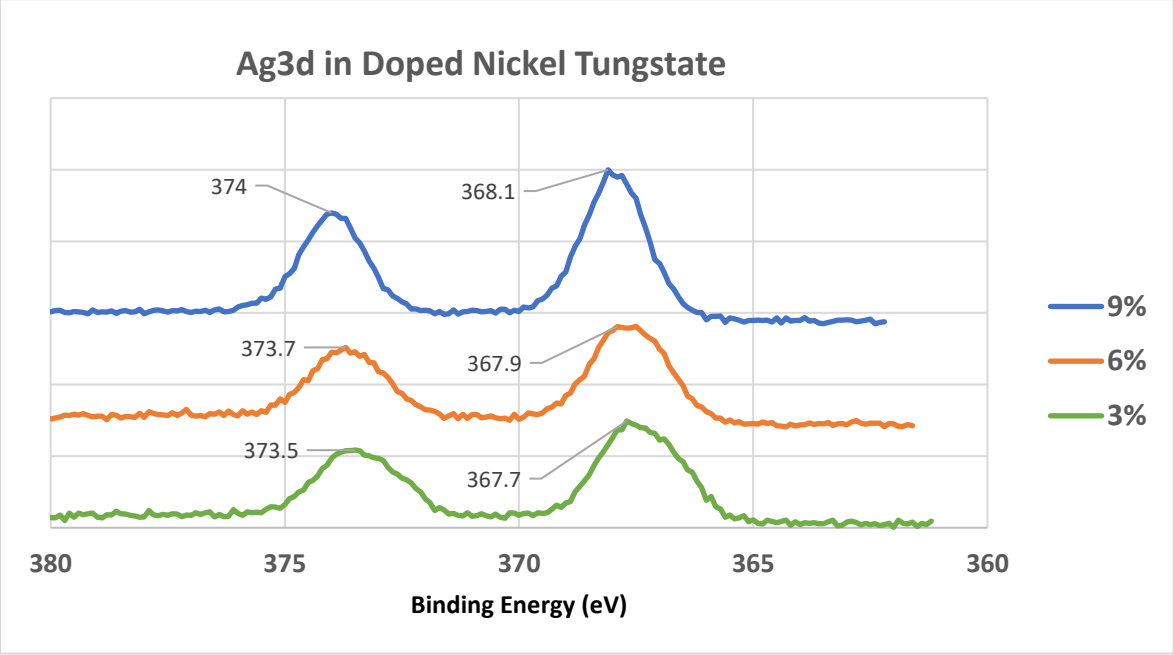

Figure 30: XPS of Ag3d electrons in silver doped $NiWO_4$

Silver's 3d orbital shows two peaks in an XPS spectra, one corresponding to $Ag3d^{5/2}$ and one corresponding to $Ag3d^{3/2}$. The peak locations of silver are in good agreement with Ag^0 nanoparticles, which should appear at values of 374 and 368 eV[57]. The resolution of this instrument is 0.1 eV.

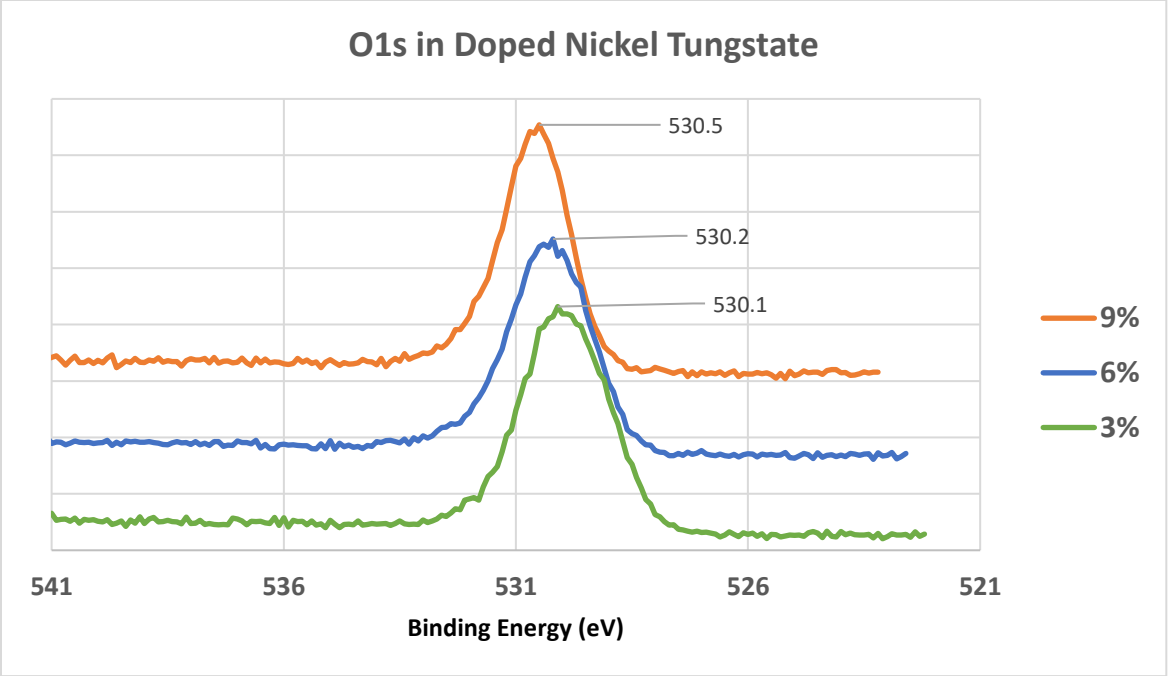

Figure 31: XPS of O1s electrons in silver doped $NiWO_4$

The O1s orbital would normally apply to the oxygen bonded between the Ni and W atoms, but since the sample has been doped we can see how the energy values of the oxygen atoms change based on the amount of dopant present. In this case, we observe that there is very little silver in the matrix of the nickel tungstate, as much has moved to the surface. Furthermore, looking at the atomic ratios of silver and nickel when compared to tungsten at the surface, it is very unlikely that Ag_2WO_4 is present in large quantities. Instead, what is likely is that some silver species is on the surface. In this case, the observed shift of the O1s peak with increasing amounts of silver suggests that a species of Ag_2O exists in varying quantities on the surface, though this decreases as silver doping increases.

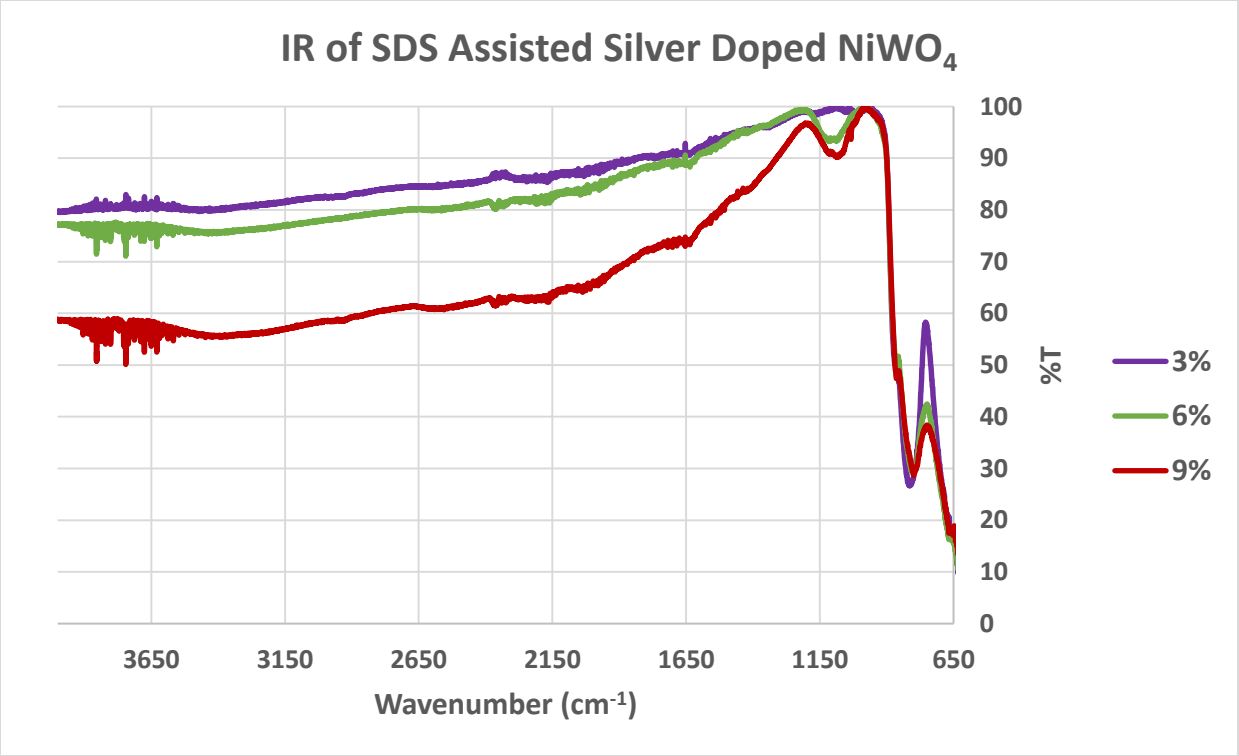

Figure 32: IR of SDS assisted silver doped $NiWO_4$

An important feature which differentiates batch 5 from batch 6 is the presence of SDS, which has been shown to affect silver in solution. In the TEM images of this batch, heavy deposition of silver can be observed in some "hotspots" of crystals, but other crystals are bare. It is likely that during the washing process, the SDS and silver which has not precipitated from solution deposits itself on the surface of some nanoparticles, and during calcination the SDS is removed leaving silver on random nanoparticles. In higher doped amounts of $NiWO_4$, the IR indicates the presence of S=O bonds, showing that while the SDS may have hydrolyzed to dodecanol and sulfate, not all of the sulfate may have been removed.

The IR-spectrum also indicates that there is potentially a mixed state of WO_4 and WO_3 in the higher doped samples due to the lack of coordination of silver with WO_3 which would form WO_4. This can be explained by the fact that since there is less silver in the matrix due to its

presence in solution with SDS, many sites in WO_4^{2-} are left uncoordinated, and transition to WO_3 during calcination treatment.

To investigate the effect of SDS on the presence of silver on the surface, and confirm the dopant migration process, another batch was prepared without any SDS, an IR-spectrum is shown in Figure 33.

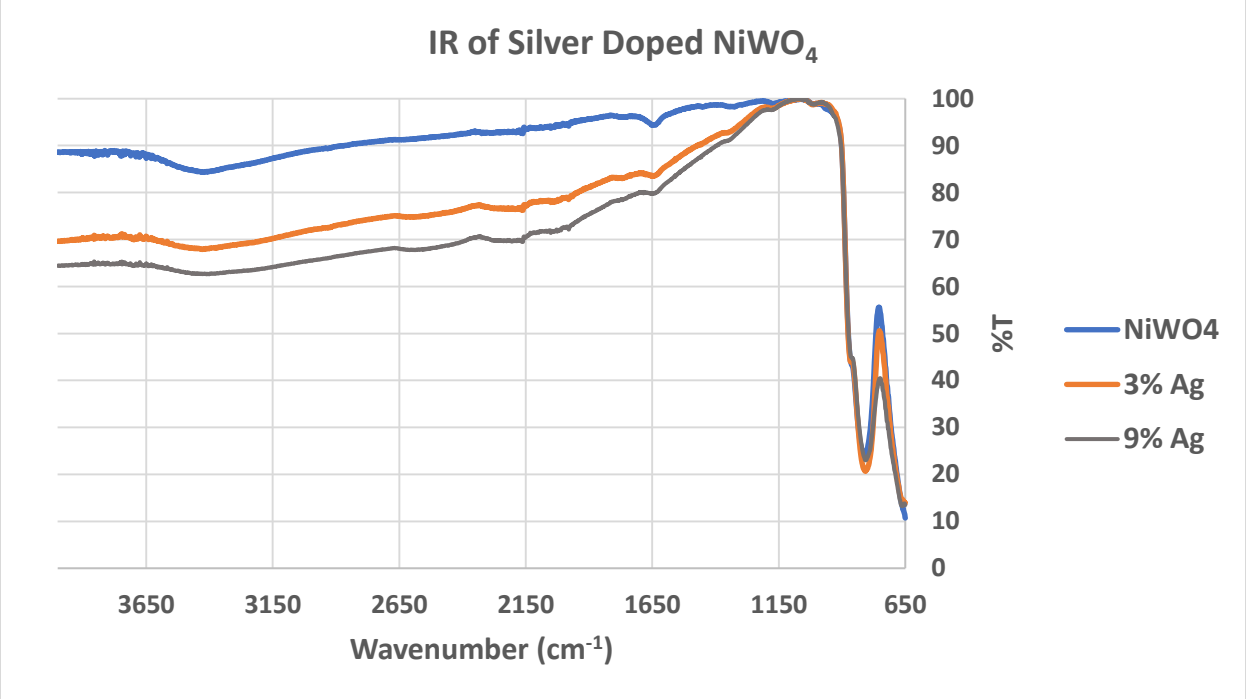

Figure 33: IR spectra of silver doped $NiWO_4$ nanoparticles

The features of the doped nanoparticles are largely the same, though the downward shift of the spectra at higher wavenumbers indicates an increased amount of scattering, which can be attributed to the increased presence of metals on the surface, which increases the roughness and surface area of the nanoparticles. The scattering in the 3% and 9% samples is not a drastically different as the 3% and bulk sample, though TEM and XPS data shows that the silver surface coverage of the 3% and 9% samples is very similar.

A combination of these three analytical methods confirm that we do not see proper doping of the bulk structure with silver, but rather that silver can act in very different ways depending on the synthetic method. However, the exploration of doping $NiWO_4$ with silver lead us to the discovery of a new route to synthesize metal-at-semiconductor nanoparticles.

The study of cocatalysts which exist as a junction between a semiconductor and a metal is a field which is often employed for photochemistry. Currently, some studies employ a deposition of metal nanoparticles onto the surface of a crystalline semiconductor in solution. The function of these cocatalysts depends partially on the interface between the two materials, which must have a relatively large area in order to allow for electron transfer between the two materials.

While some formations of cocatalysts require a sophisticated method to ensure a strong interface between the two materials, the method for these silver/nickel tungstate cocatalysts allows for a simple one-pot synthesis of a material with an intrinsic junction. Further studies may be warranted to investigate other systems which may be able to be formed through similar mechanisms.

3.1.3 – Mild Condition Synthesis

With the above results showing the possible outcomes of a failed doping of silver nanoparticles, a new set of conditions was explored to assess the structure of the nanoparticles under mild heating. Since dopant migration is a thermodynamic process[65], calcination temperature was a key factor to manipulate to try to prevent this outcome. Calcination is a process to form a more ordered structure, and to transform the materials from an amorphous phase to a crystalline phase. Furthermore, IR spectra of the $NiWO_4$ at low calcination

temperatures (Figure 20) indicates the probable presence of uncoordinated metal oxides such as nickel and silver oxide on the surface. Pre-calcinated samples indicate presence of nickel hydroxide by the mint green color of the catalyst. This color completely disappears after heating beyond 280°C.

A Thermogravimetric Analysis (TGA) by the Trushnikova group reveals that the temperature of decomposition in standard atmospheric conditions occurs around 260°C[66]. This represents the minimum temperature required for calcination of the doped samples. During the study on the thermal stability of the hollow nanospheres, collapse was not observed until well above 350°C. The most pronounced and clear nanospheres were formed at 380°C while also avoiding the appearance of silver nanoparticles on the surface. Using this information, the nanoparticles were synthesized with an SDS surfactant-mediated procedure described by batch 7, where they were calcinated at 380°C.

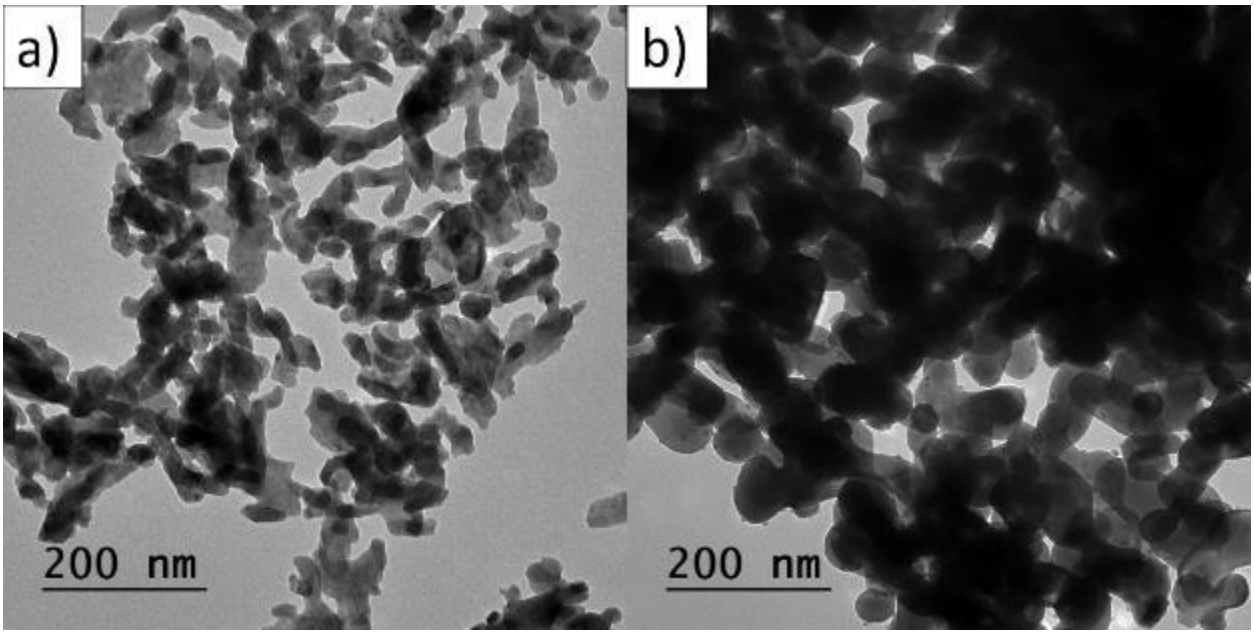

Figure 34: TEM images of batch 7 samples. a) Calcinated at 380°C; b) Calcinated at 550°C

At 380°C (a) nanoparticles can be observed with no agglomeration of smaller particles on the surface. An amorphous shape is observed, though some ordered structure and uniform

particle thickness is also apparent. To verify the presence of silver somewhere within the sample, a second portion of the same sample was calcinated at 550°C (b), a temperature which previous experiments have guaranteed to force any internal silver to the surface of the tungstate nanoparticle. It was observed that silver did indeed migrate to the surface at higher temperatures, while there was no apparent formation of silver nanoparticles observed on the surface of sample (b).

XPS and XRD analysis was performed to verify the elemental distribution and crystallinity. For reference, the doping percentage of the sample analyzed was 3%, which can be written as $Ag_{0.06}Ni_{0.97}WO_4$. The expected XPS elemental ratios for a 3% doped sample are shown in Table 6.

Table 6: Predicted relative presence of elements on surface of amorphous 3% silver doped $NiWO_4$

Electron	Relative Presence
W4f	16.6%
Ni2p	16.1%
O1s	66.3%
Ag3d	1.0%

Additionally, it can be calculated that an appropriate atomic ratio of Ni2p electrons to W4f electrons would be 0.48:0.52. Below is the actual XPS spectra of sample (a):

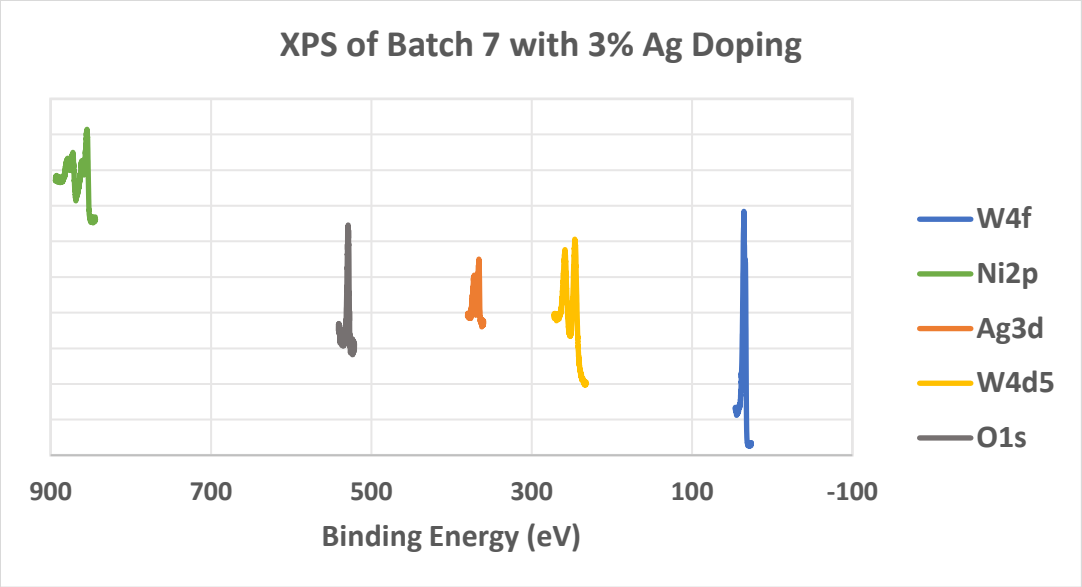

Figure 35: XPS data for 3% silver doped $NiWO_4$ calcinated at 380°C

This spectrum consists of an average 3 different samples of the same material to assess uniformity. A table of integrated values to represent the relative atomic percentages is shown below:

Table 7: Experimental relative presence of elements on surface of amorphous 3% silver doped $NiWO_4$

	Relative Presence		
	1	**2**	**3**
W4f	15.9%	14.9%	15.2%
Ni2p	15.6%	14.8%	14.4%
O1s	65.7%	67.2%	66.6%
Ag3d	2.8%	3.1%	3.9%
Ni:W	0.495:0.505	0.498:0.502	0.486:0.514

The data shows a silver presence between 3x and 4x higher than predicted, while Ni:W ratios are also higher than predicted. The high surface presence demonstrates a clear migration of the dopant, while high atomic ratio of Ni:W shows that most W is coordinated to Ni, and the Ag which is present is mostly uncoordinated to the W. Another way to interpret the relative surface presence of tungstate species vs. possible silver/silver oxide species is to look at the expected number of oxygen atoms per tungsten atom. Ideally, every tungsten atom should account for 4 oxygen atoms. In this case, the relative presence should be represented by the following table, under the assumption that each percentage would equal one "count" of an atom. The table below approximates expected oxygen counts based on the tungsten counts for each sample. The O unaccounted atoms are calculated by comparing the relative presence of O on table 7 and table 8.

Table 8: Relative tungsten and oxygen presence on surface of amorphous 3% silver doped $NiWO_4$

	Relative Presence		
	1	2	3
W	15.9	14.9	15.2
O	63.6	59.6	60.8
O Unaccounted	2.1	6.6	5.8

One additional consideration for the excess oxygen on the surface is the presence of nickel oxide species on the surface which may have reformed post-calcination[67].

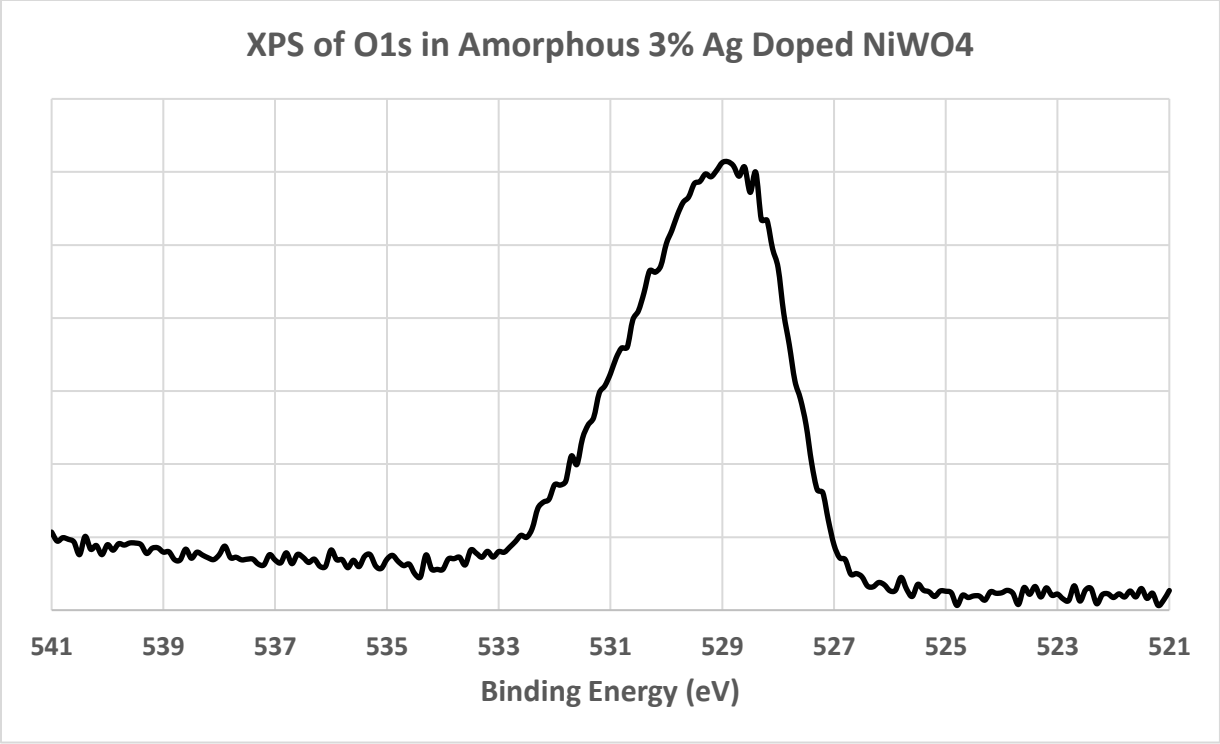

Figure 36: XPS of O1s electrons in amorphous silver doped $NiWO_4$

The O1s orbital shows a mixed state of oxygen environments, which is trademarked by a peak with a sharp end and a broad end on either side[61]. This indicates at least two separate states contributing to the peak. In the IR analysis of doped $NiWO_4$ at 380°C, multiple O-H related peaks were present in the spectrum, as well as a distorted W-O stretch. This XPS data along with the IR analysis supports the presence of a mixed oxygen environment, probably originating from a mixed amount of WO_3 and WO_4^{2-}.

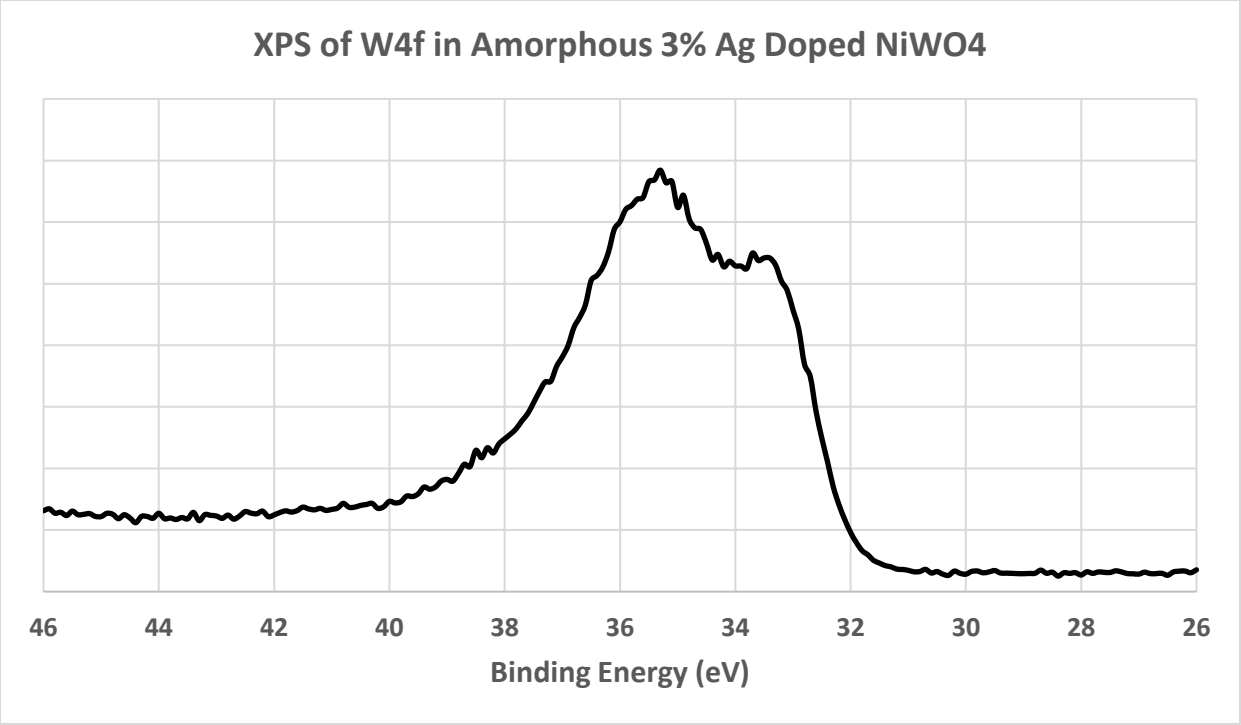

Figure 37: XPS of W4f electrons in amorphous silver doped $NiWO_4$

The W4f orbital also shows a mixed state of tungsten environments, confirming the mixture of WO_3 and WO_4^{2-}. The IR spectra of these samples at different temperatures suggest that the transition at 430°C is most likely promoted by the coordination of metal oxides to form tungstates, which is supported by this XPS data. This data shows a majorly mixed state, while as discussed earlier WO_4^{2-} should show two very sharp peaks with a deep valley between them, with the lower energy peak being the higher one.

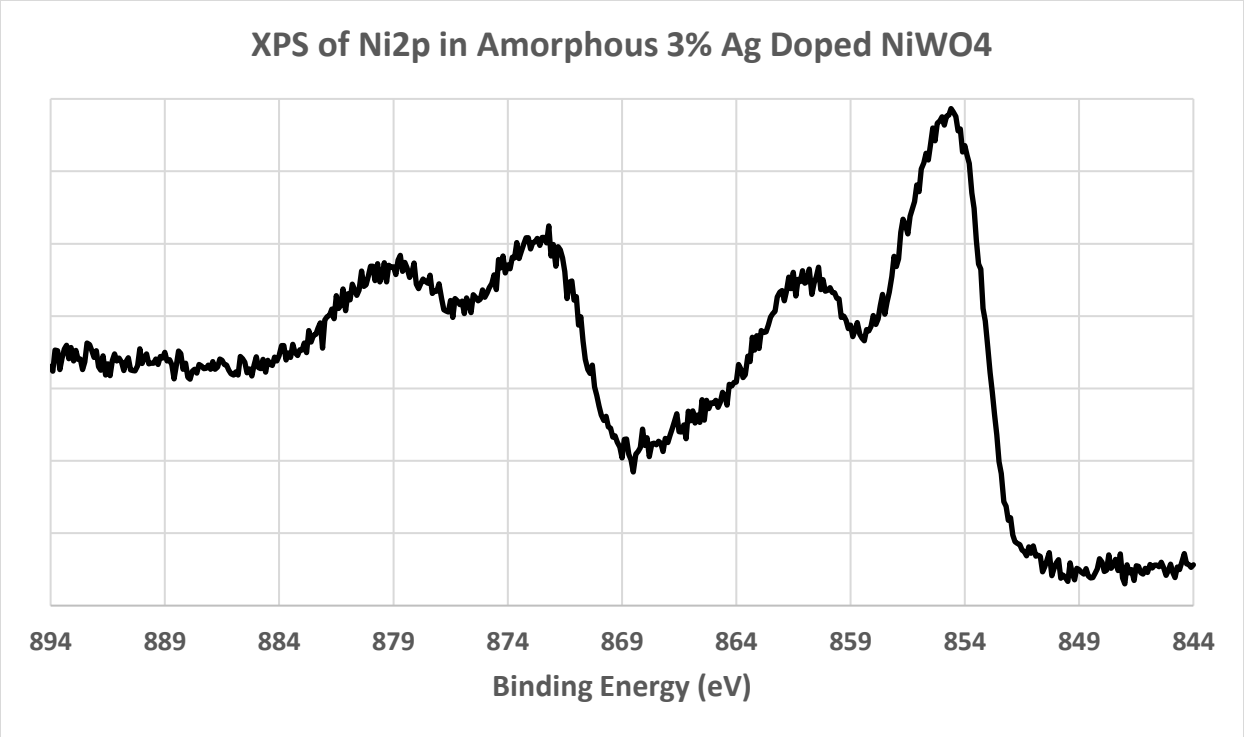

Figure 38: XPS of Ni2p electrons in amorphous silver doped $NiWO_4$

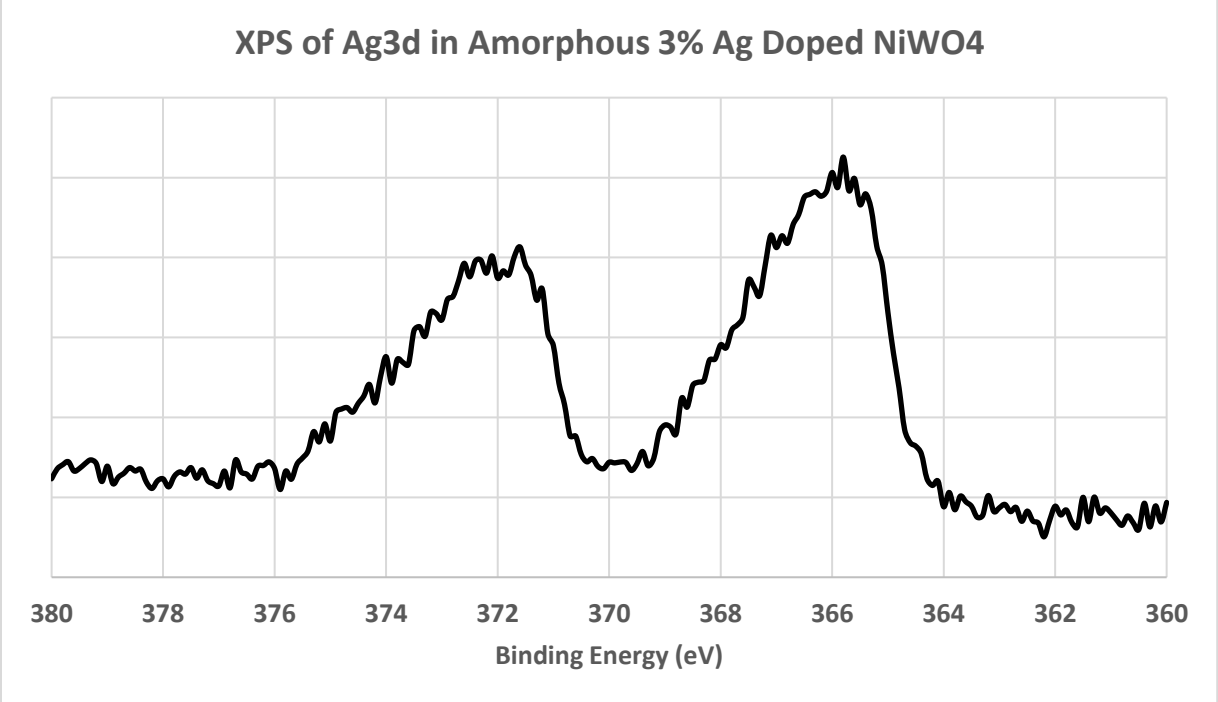

Figure 39: XPS of Ag3d electrons in amorphous silver doped $NiWO_4$

The Ni2p and Ag3d XPS graphs both show mixed states with a broad edge at higher binding energies, suggesting that there are mixed amounts of Ag_2O and NiO and potentially Ag^0, Ag_2WO_4, and $NiWO_4$. This also suggests that the O-H bands in the IR (Figure 20) are not solely due to moisture on the surface of the sample, but could indicate metal oxide and hydroxide vibrations.

Two silver peaks represent the 3d orbital, and a trailing toward a higher binding energy in both peaks indicates a mixed state for silver in the matrix. Multiple silver/silver oxide species are likely to exist on the surface. Below is a comparison of the silver states of crystalline $NiWO_4$ with silver on the surface vs. the amorphous $Ag/NiWO_4$ composite.

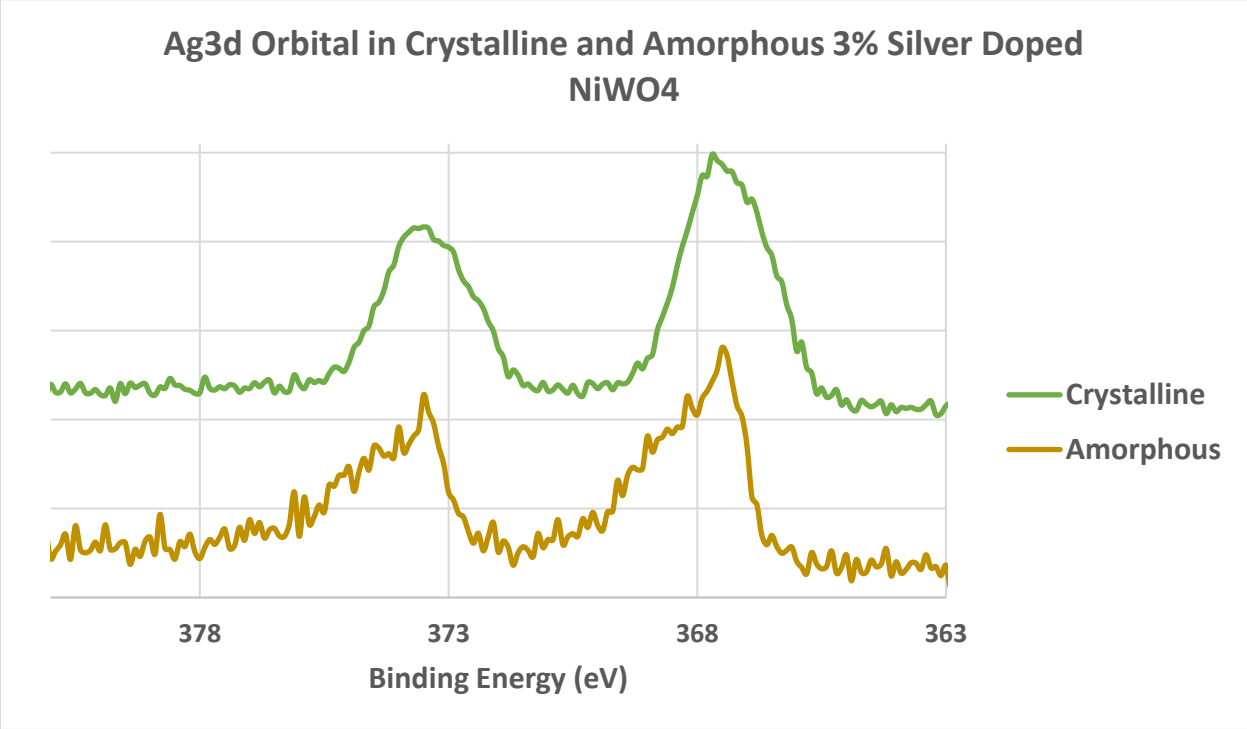

Figure 40: XPS of Ag3d orbital for amorphous vs. crystalline silver doped $NiWO_4$

Comparison between the Ag3d orbital for the amorphous samples calcined at 380°C versus the crystalline samples calcined at 550°C help to contrast the peaks of silver dominated by a single state, rather than multiple.

XRD was performed to assess crystallinity of the structure. A Cu-Kα X-ray source was used for all measurements. The y-axis values should be understood as arbitrary units. The x-axis represents angle of incidence for the rays, and is in the units of 2θ. The data shows multiple structures, with peaks not corresponding to $NiWO_4$ present.

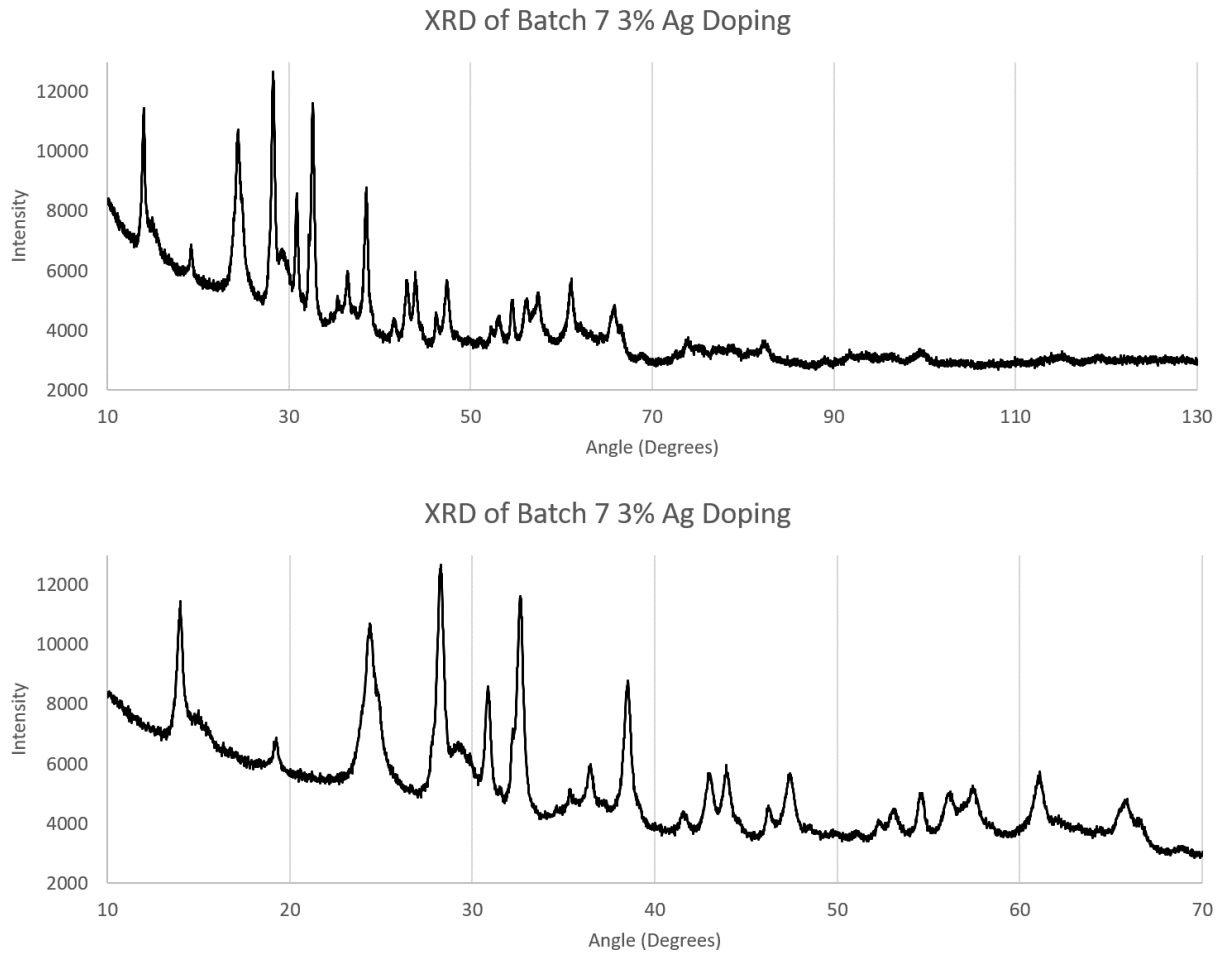

Figure 41: XRD of amorphous 3% silver doped $NiWO_4$

3.2 – Zinc Tungstate

To assess the effectiveness of doping zinc tungstate with copper, XRD, XPS, and TEM were performed. XRD and TEM allow for an assessment of crystallinity and uniformity of each

species, while XPS allows for a quantitative analysis of the relative abundance of each species on the surface of the semiconductor.

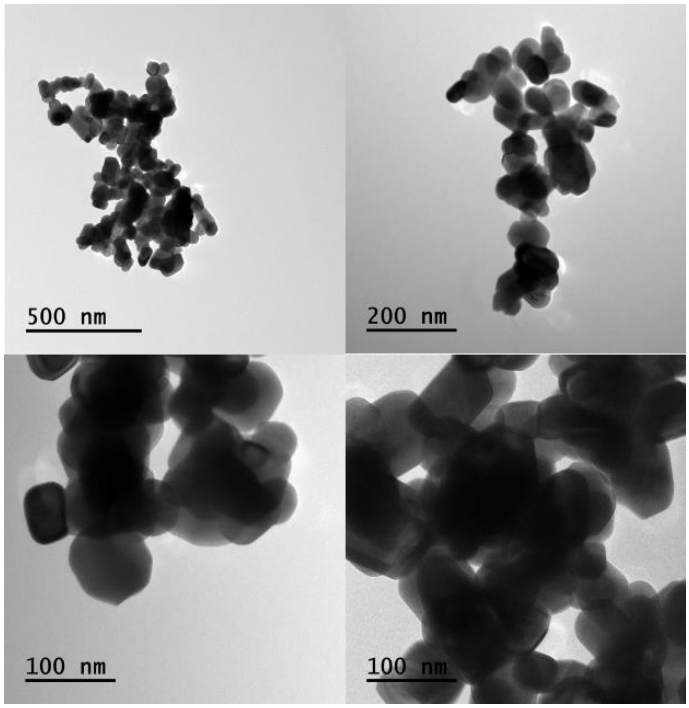

Figure 42: TEM images of undoped $ZnWO_4$

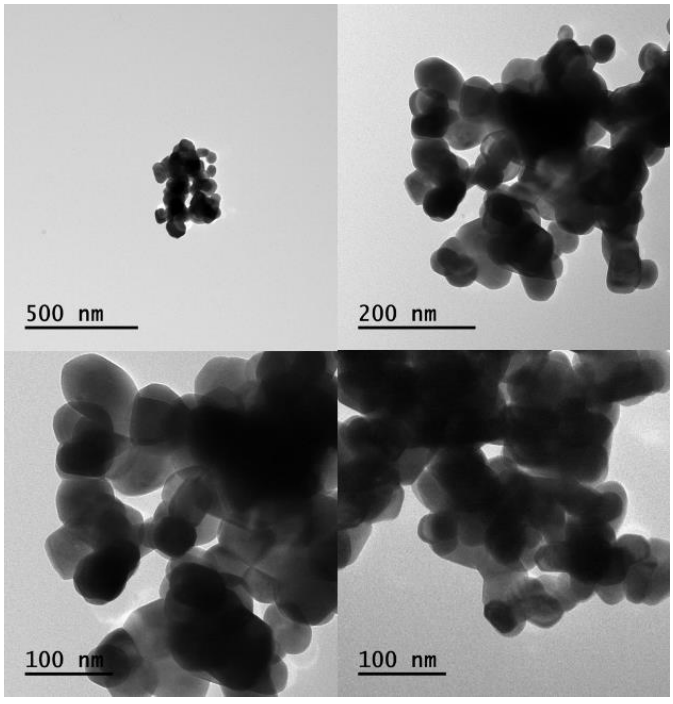

Figure 43: TEM images of 3% copper doped $ZnWO_4$

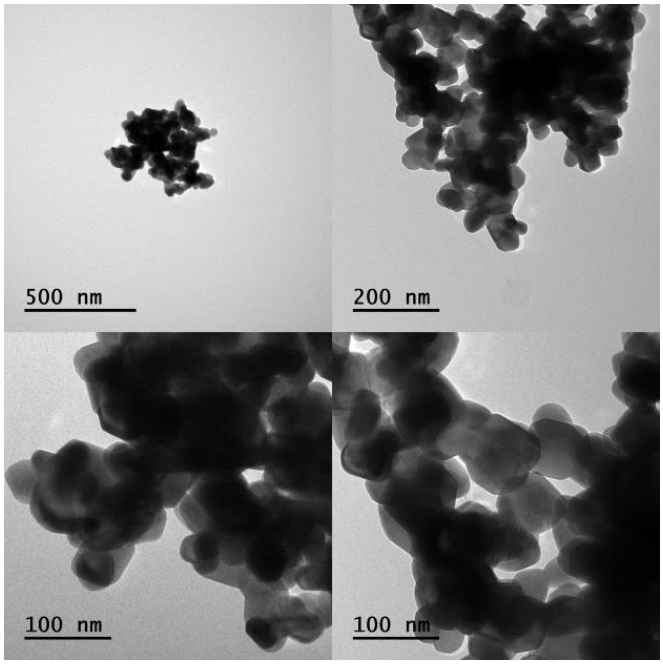

Figure 44: TEM images of 6% copper doped $ZnWO_4$

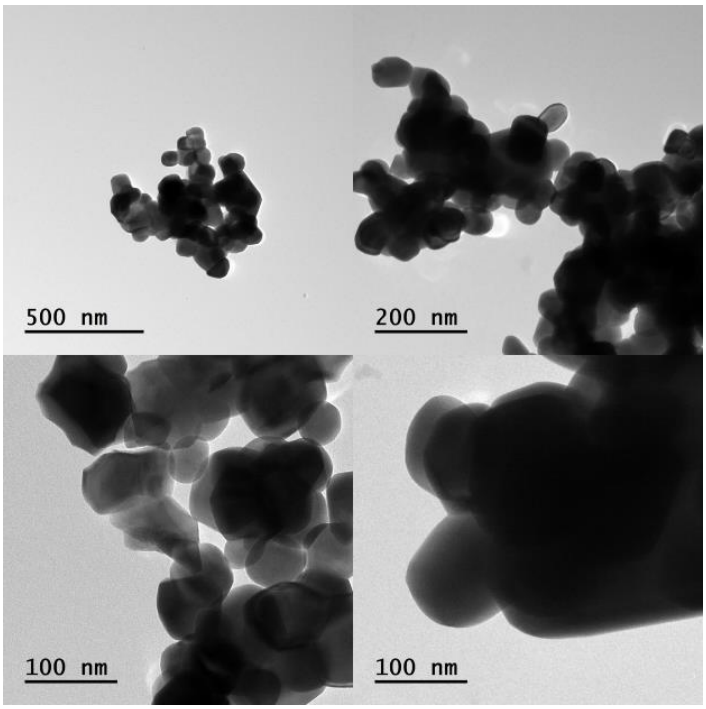

Figure 45: TEM images of 9% copper doped $ZnWO_4$

Unlike doping $NiWO_4$ with the silver, doping $ZnWO_4$ with copper results in crystalline samples with no discernable heterostructures. Even at high doping levels, the copper does not migrate out to the surface and form independent nanoparticles. All surfaces of the bulk and doped nanoparticles are clean, indicating a uniform surface. TEM is a qualitative analysis, therefore XRD was performed to probe deeper into the crystalline nature of the sample.. The y-axis values are unlabeled, but should be understood as arbitrary units.

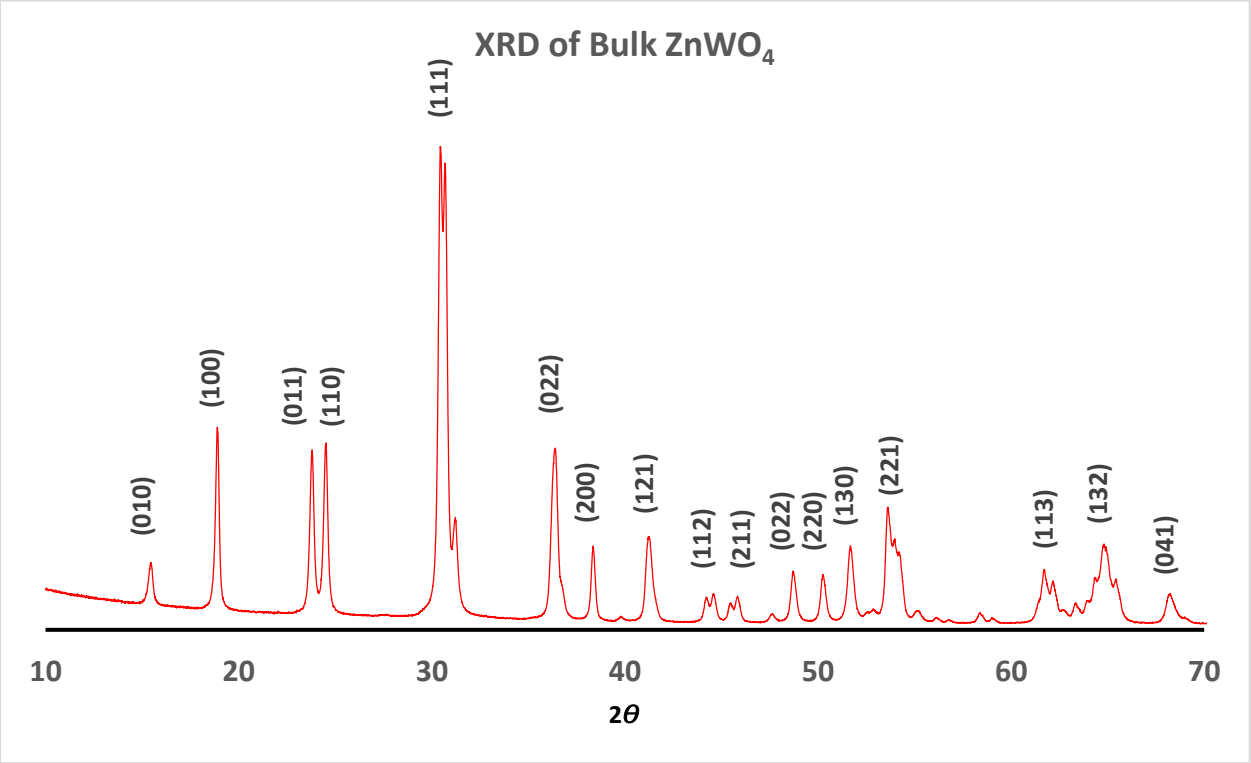

Figure 46: XRD of undoped $ZnWO_4$

In comparison to literature[68] it can be seen that all major peaks associated with $ZnWO_4$ are accounted for, and we observe good crystallinity. The respective miller indices for the material have been assigned to each peak. In subsequent spectra (Fig. 47-49) peaks are unassigned as they remain the same as in Figure 46.

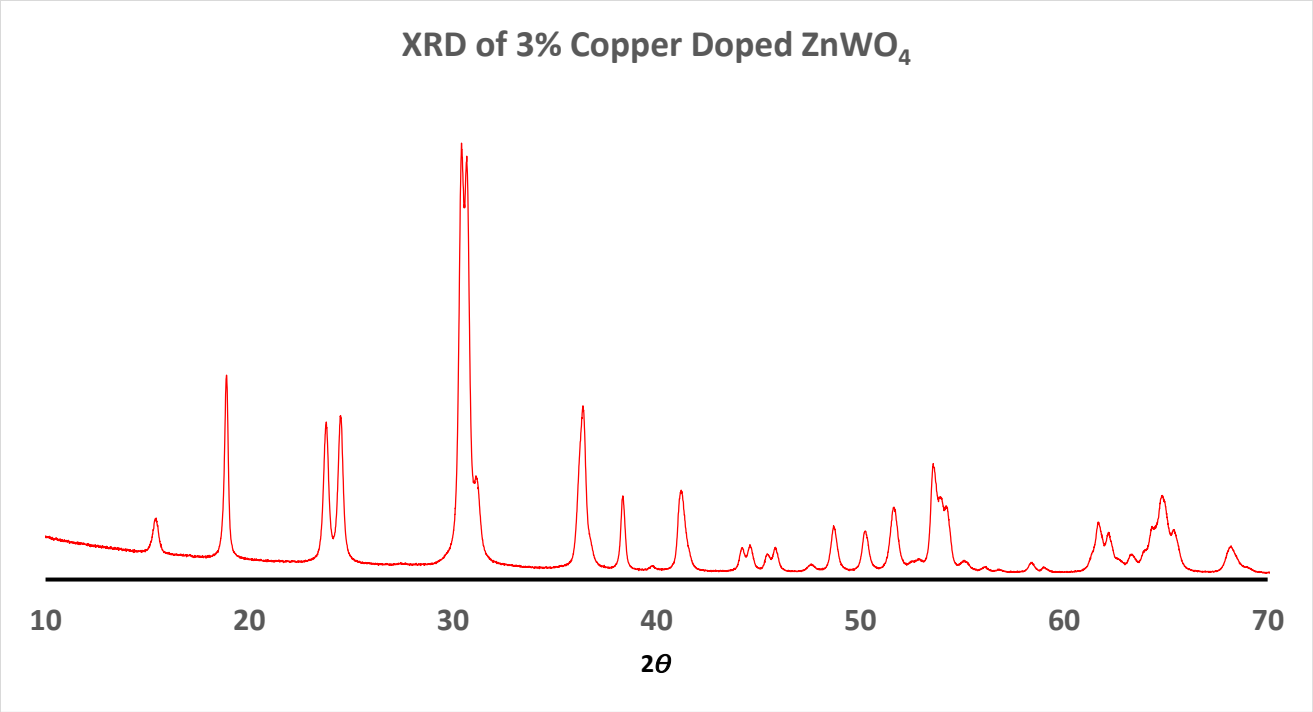

Figure 47: XRD of 3% copper doped $ZnWO_4$

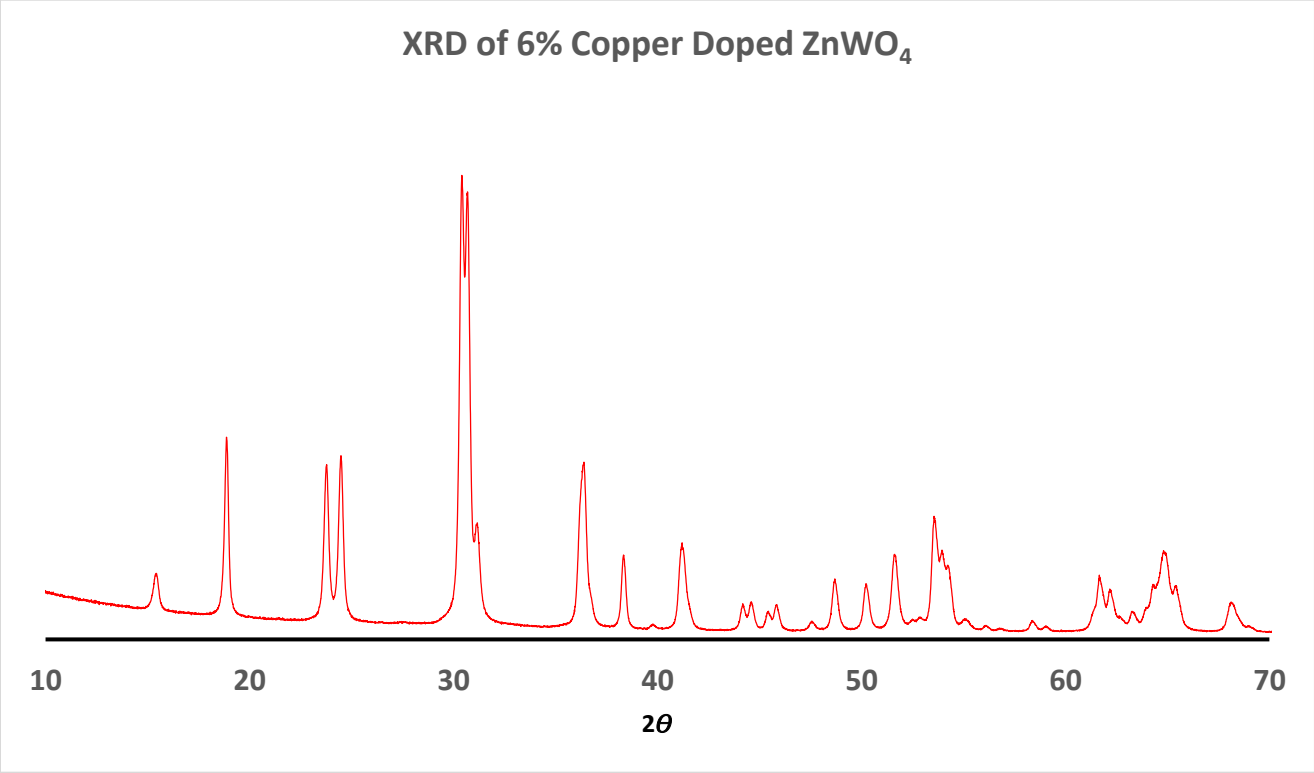

Figure 48: XRD of 6% copper doped $ZnWO_4$

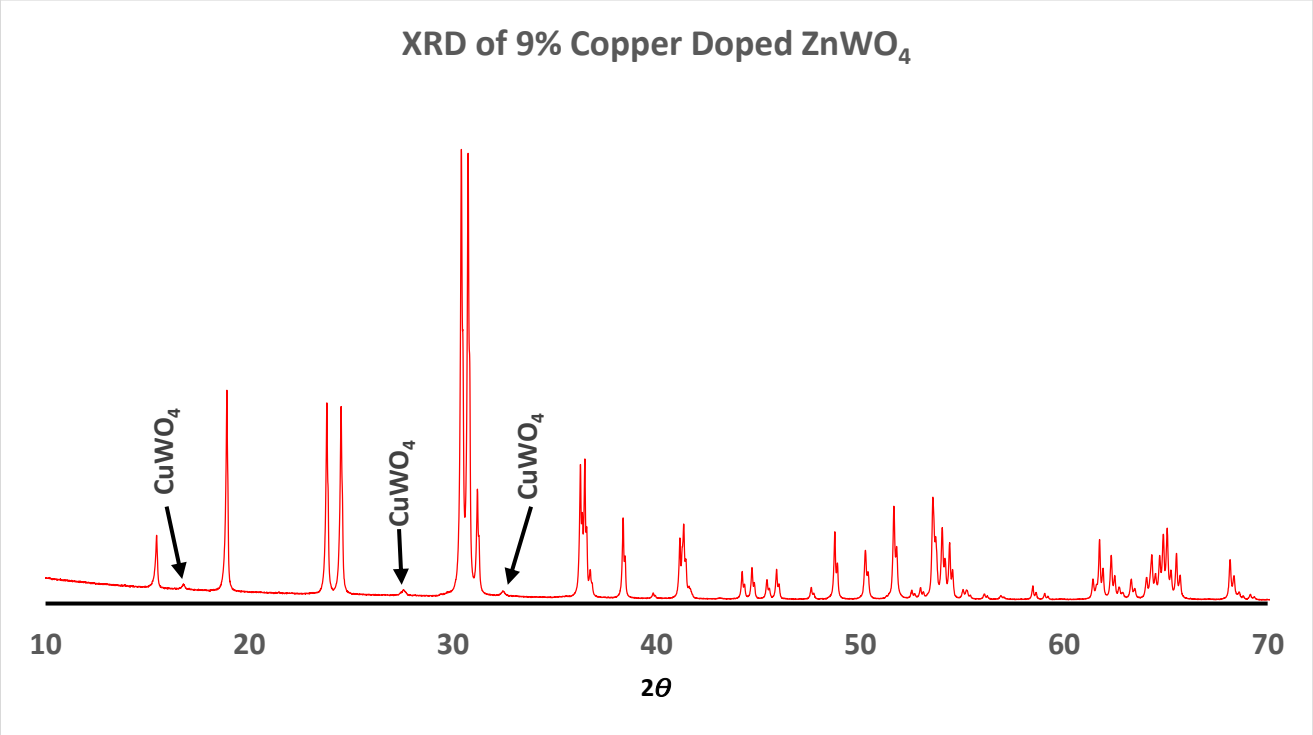

Figure 49: XRD of 9% copper doped $ZnWO_4$. $CuWO_4$ features are labeled

The 3% and 6% copper doped samples show no discernable traces of $CuWO_4$, which suggests that it sits within the crystal distributed with a degree of homogeneity, it is not until the 9% doping sample where peaks which correspond to $CuWO_4$ emerge. This may indicate incomplete coordination of Cu within the sample, leading to some independent $CuWO_4$ structures.

To probe the elemental nature of the material, XPS analysis was done in order to quantify the relative abundance of each species on the surface of the nanoparticles. Similar to $NiWO_4$, the XPS focuses on the W4f, O1s, Zn2p, and Cu2p electrons. The height of the peaks corresponds to the counts per second (cps) and can be regarded as an arbitrary unit. In order to appraise the relative presence of each atom, integrals of the peaks were performed after baseline correction. For the following spectra, the peaks have been offset in the y-direction for clarity.

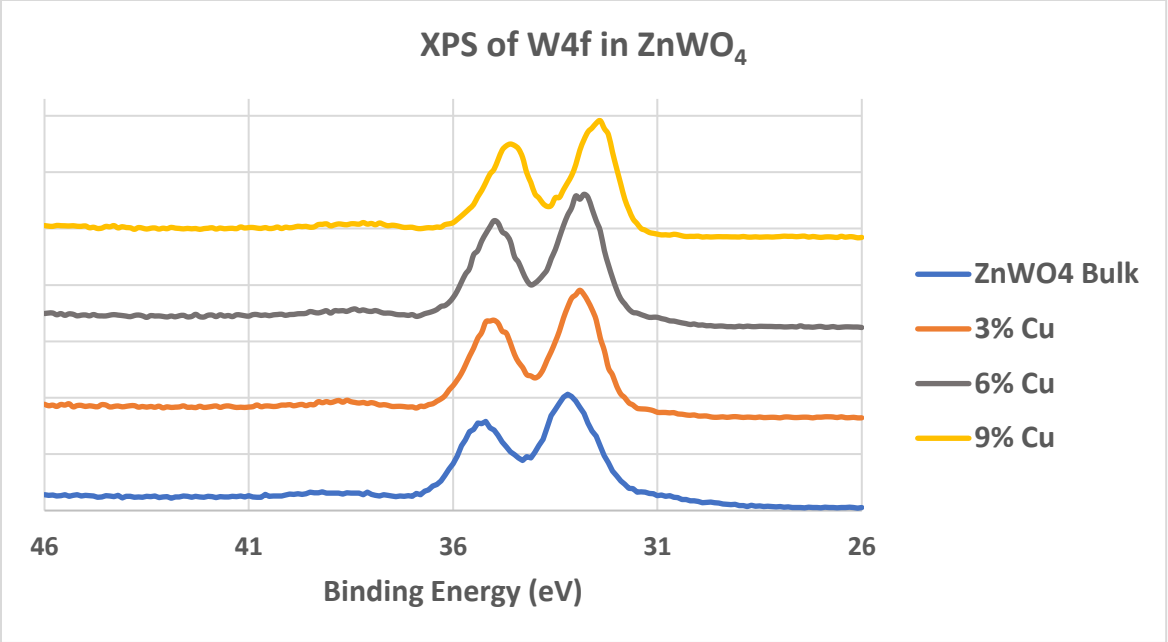

Figure 50: XPS of W4f electrons in doped $ZnWO_4$

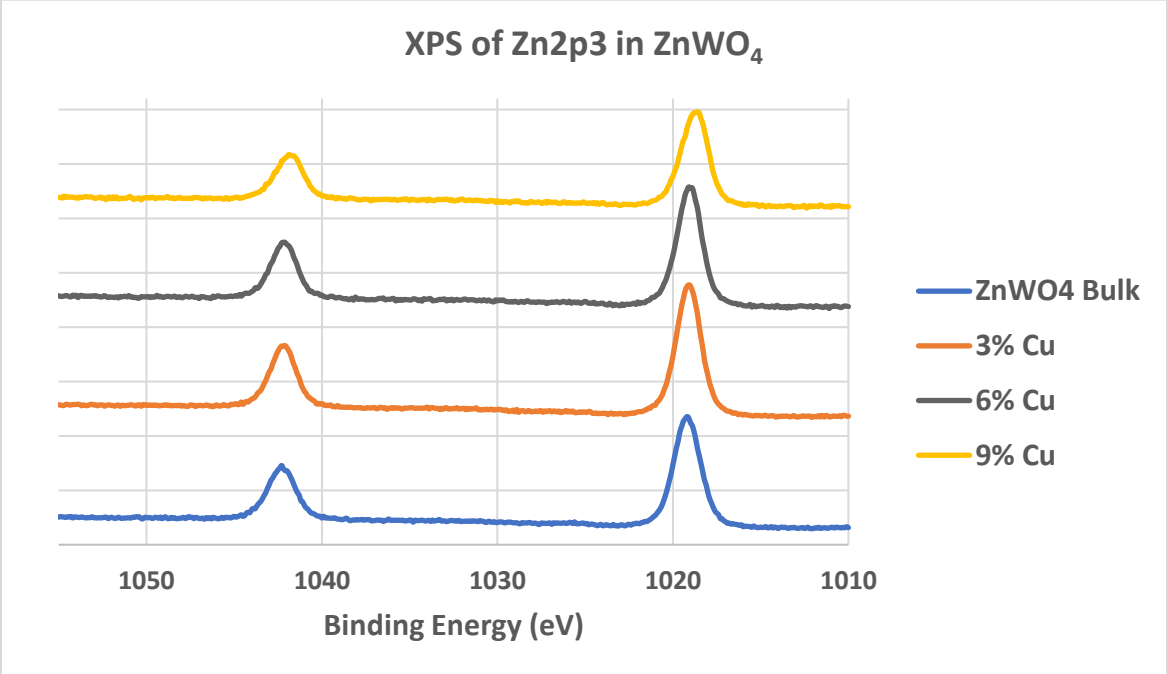

Figure 51: XPS of Zn2p3 electrons in doped $ZnWO_4$

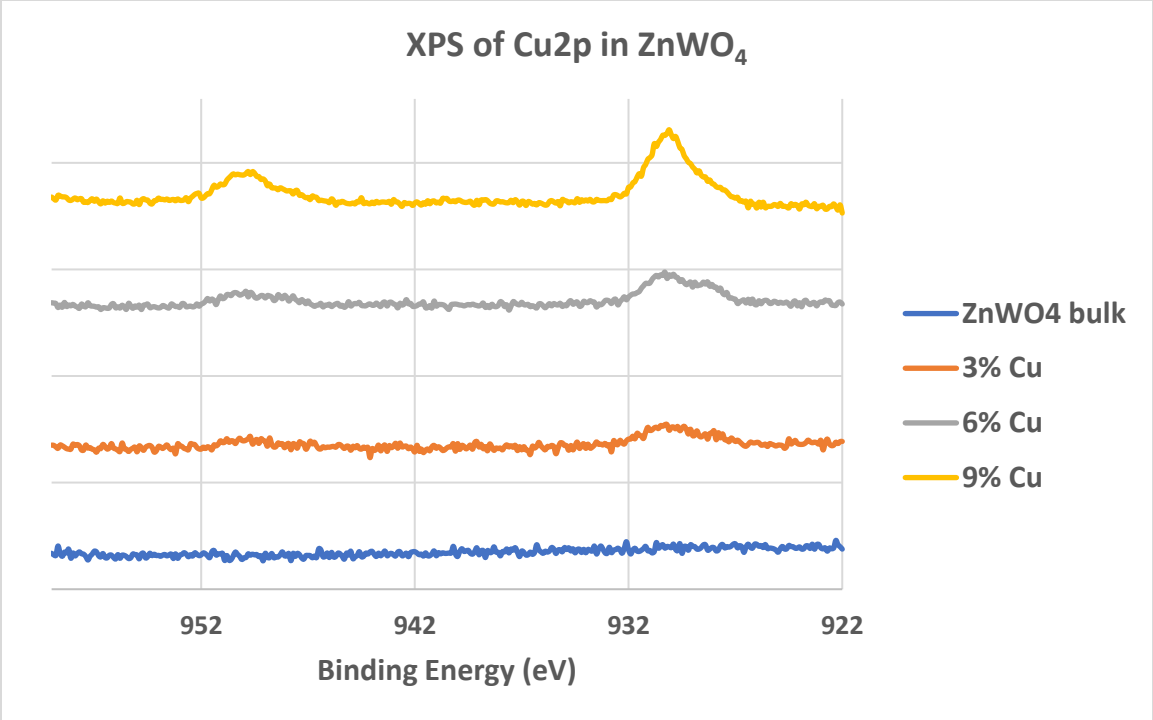

Figure 52: XPS of Cu2p electrons in doped $ZnWO_4$

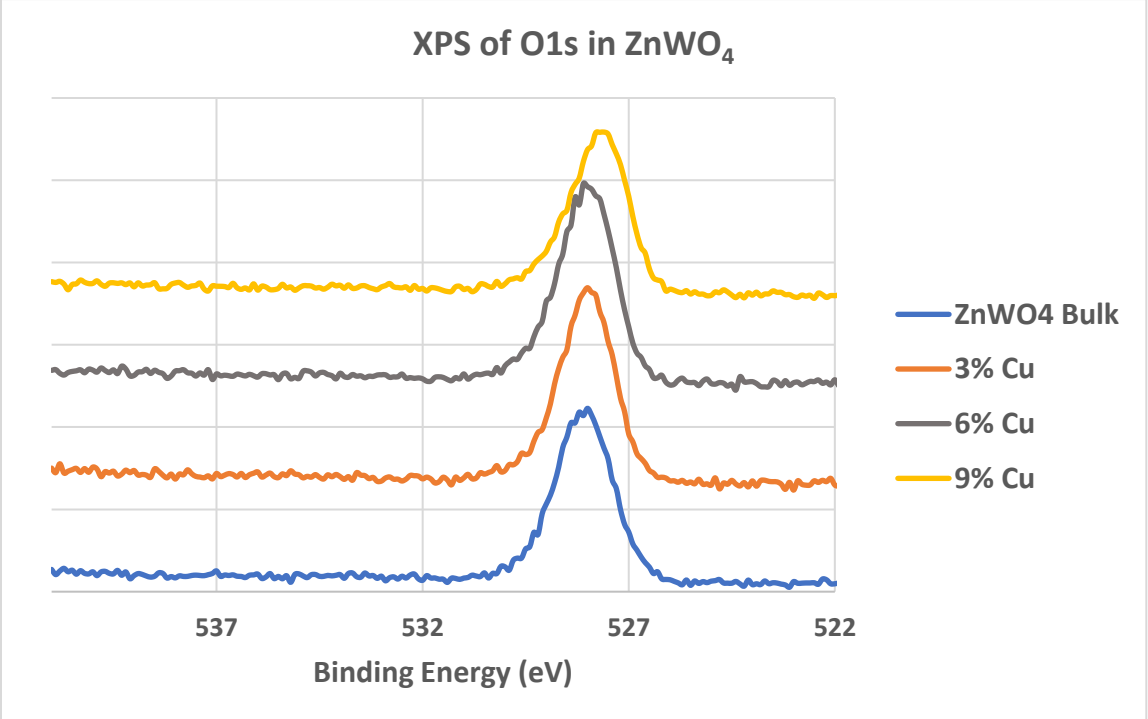

Figure 53: XPS of O1s electrons in doped $ZnWO_4$

Unlike the silver doped samples of $NiWO_4$, sharp W4f peaks are maintained in all samples, indicating a majority presence of W^{6+} oxidation state. The Cu2p peaks grow in an expected manner according to the increased amount of doping, while the Zn2p3 peaks shrink by comparison. The O1s peak broadens, indicating multiple electronic environments felt by the oxygen atoms. This corresponds to the increased abundance of Cu in the matrix, which has a higher electronegativity than Zn and causes the electrons in the oxygen atoms to have slightly different binding energies.

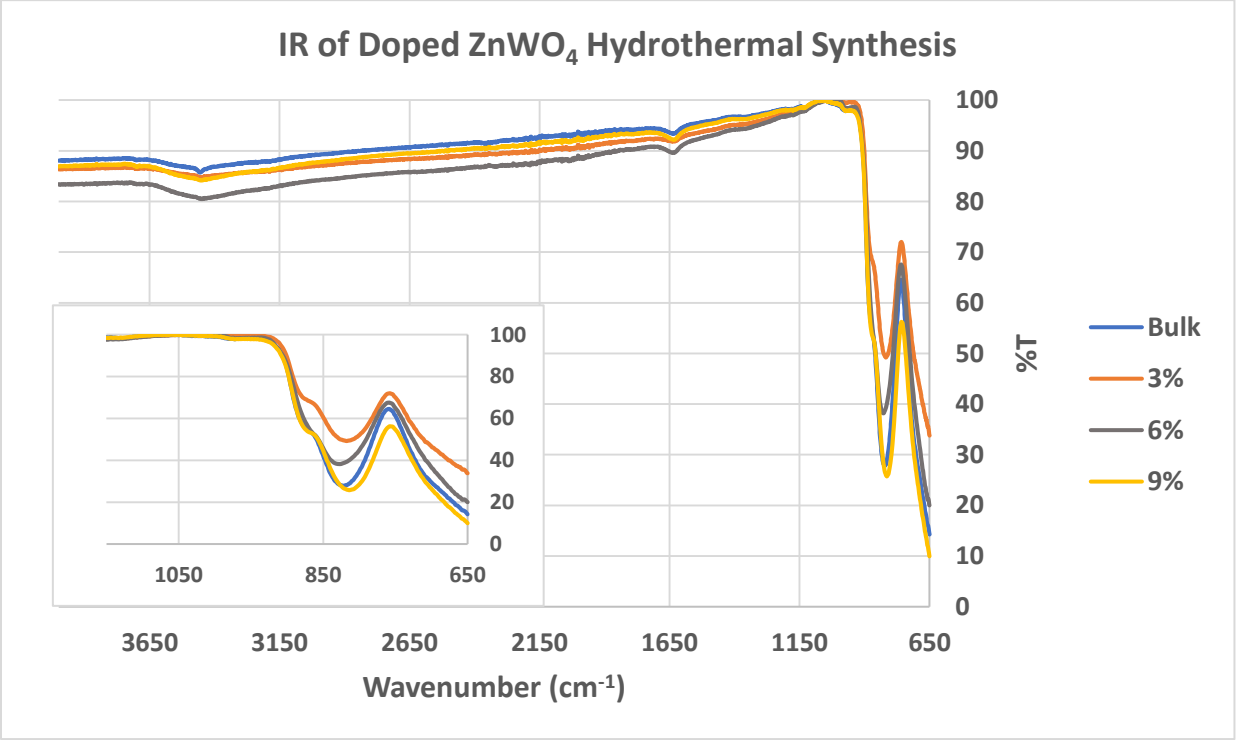

Figure 54: IR spectra of copper doped zinc tungstate samples

The IR spectra for the doped samples show a very similar surface environment for all 4 samples, and very similar amounts of scattering indicating a uniform structure between all samples. The peaks and bends at 3435 cm^{-1} and 1645 cm^{-1} correspond to water on the surface of the nanoparticles, which is minimal.

UV-DRS was performed in order to assess the band gap of the copper doped materials.

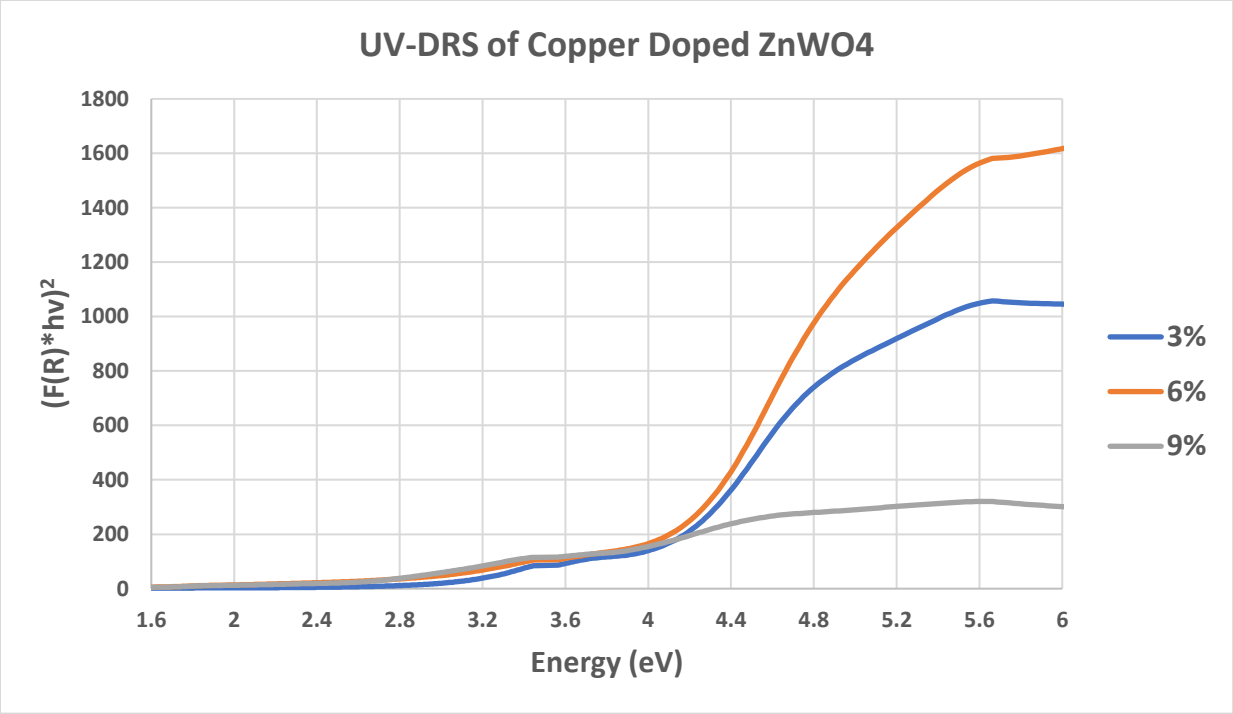

Figure 55: UV-DRS Data for Copper Doped $ZnWO_4$

The data above shows a Kubelka-Munk corrected graph for the extrapolation of the direct band gap of the samples. Extrapolation of band gap can be taken by performing a linear fit of the downward sloping portion of the graph, and finding an interception point for the subsequent leveled portion of the graph. The x-value of the interception point represents the direct band gap value. The band gaps calculated for the 3%, 6%, and 9% doped samples are 4.0, 4.2, and 4.2 eV respectively.

Multiple samples have been synthesized for both nickel and zinc tungstate with modifications by silver and copper. While a properly doped silver-nickel tungstate sample was prepared, multiple alternate samples with potentially high activity were created instead. A cocatalyst and hollow sphere system both show potential for higher activity when compared to the bulk material. It has been shown that a size dependence may exist for the doping of $NiWO_4$ with group 11 elements. This is supported by the observation that both nickel and zinc tungstate can

be properly doped with copper, which shares a similar atomic radius. Copper doped zinc tungstate was prepared and XPS and XRD data provided by Seyyedamirhossein Hosseini shows even atomic presence of copper at the surface of zinc tungstate while preserving zinc tungstate's crystallinity.

4 – Photocatalysis of Methylene Blue with Tungstate Samples

A series of photodegradation reactions were performed to assess the change in efficiency based on the morphology and doping level of the samples. In the case of the nickel tungstate and the co-catalyzed nickel tungstate, an assessment for the effect of the co-catalyst was analyzed. For the copper doped zinc tungstate, the effect of the copper dopant was under analysis.

Methylene blue was chosen as the dye to be studied, as it is prevalent in literature dealing with metal tungstates[2,48]. For this reason, the results of the papers could be independently confirmed, as well as used as a guide for the preparation of the experiments to be performed. All photocatalysis experiments with methylene blue were performed under a 300W Xenon lamp in the arrangement shown below:

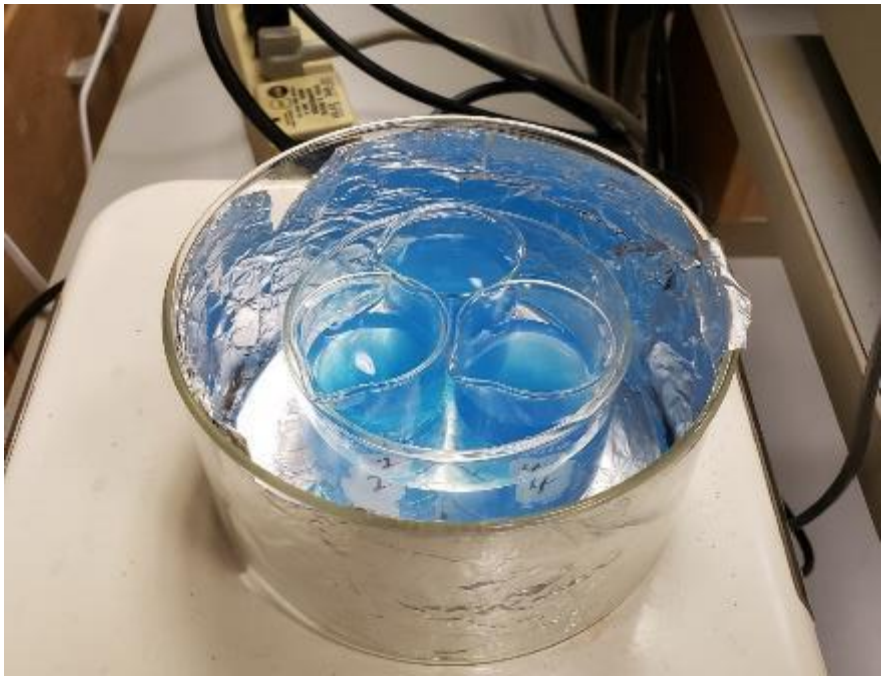

Figure 56: Photodegradation experimental setup

Pictured is three samples with stir bars held in a crystallizer dish filled with water. Upon every measurement of the sample, the water in the crystallizer was replaced to maintain a low temperature. Finally, a reflective box was placed around the lamp and aimed at the sample to

maximize the amount of light exposed to the sample. In some tests, a 295 nm cutoff filter was employed to limit the amount of high energy light from hitting samples.

Samples were covered with a Pyrex dish to prevent loss of solvent. 25mL of a 1.4 x 10^{-5}M solution of methylene blue was combined with 5mL of Millipore water containing an amount of the catalyst, and then sonicated and stirred for 30 minutes to ensure complete adsorption of the dye to the catalyst surface and complete dispersion of the catalyst in solution. Figure 56 shows a graph of the percent transmittance of light through the Pyrex dish by wavelength. This data was collected by placing the pyrex dish in front of the UV-source in the same spectrometer used for the subsequent experiments.

The maximum transmittance is 38.34% of light intensity at 340 nm. The cutoff wavelength, defined as the point where 50% of the maximum light is transmitted, is at 301 nm. When the filter is added to the setup, the maximum transmittance decreases to 33.43% at 351 nm of light, and the cutoff wavelength shifts up to 309 nm.

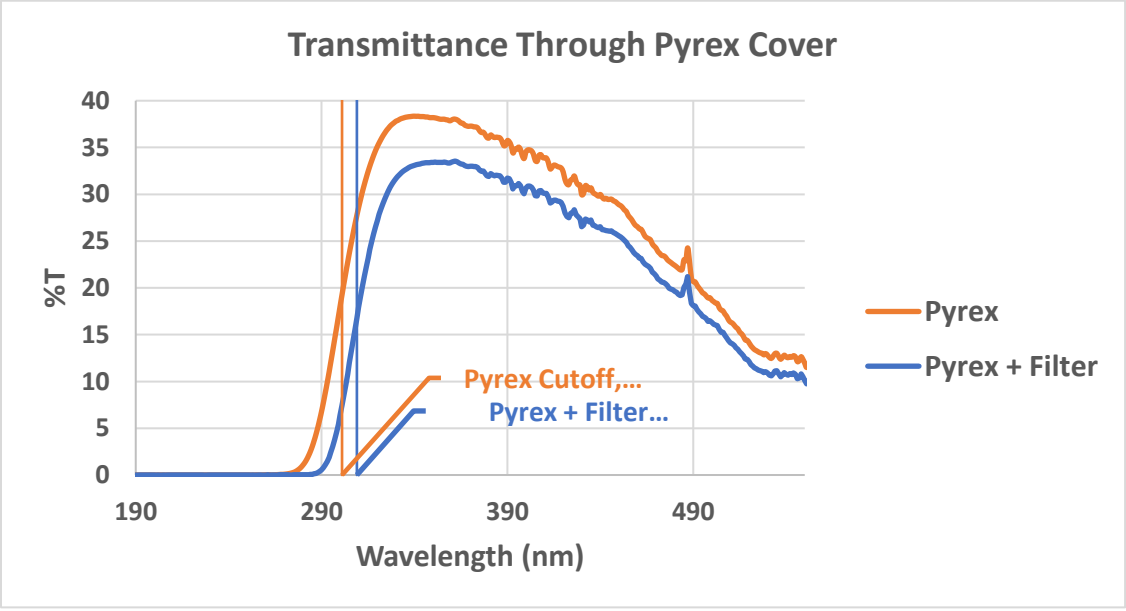

Figure 57: Transmittance of light through lamp filters

Prior to exposure to the xenon lamp, a 3mL aliquot of each sample was taken and centrifuged to remove the catalyst. UV measurements were performed with an Agilent G1103A UV Spectrophotometer. Every subsequent measurement followed the same procedure of removing a 3mL aliquot of solution and centrifuging out the catalyst. A preliminary catalyst loading experiment was performed without the filter to find the optimal concentration of catalyst in solution. This experiment involved illuminating the samples for 60 minutes and comparing relative degradation with each load.

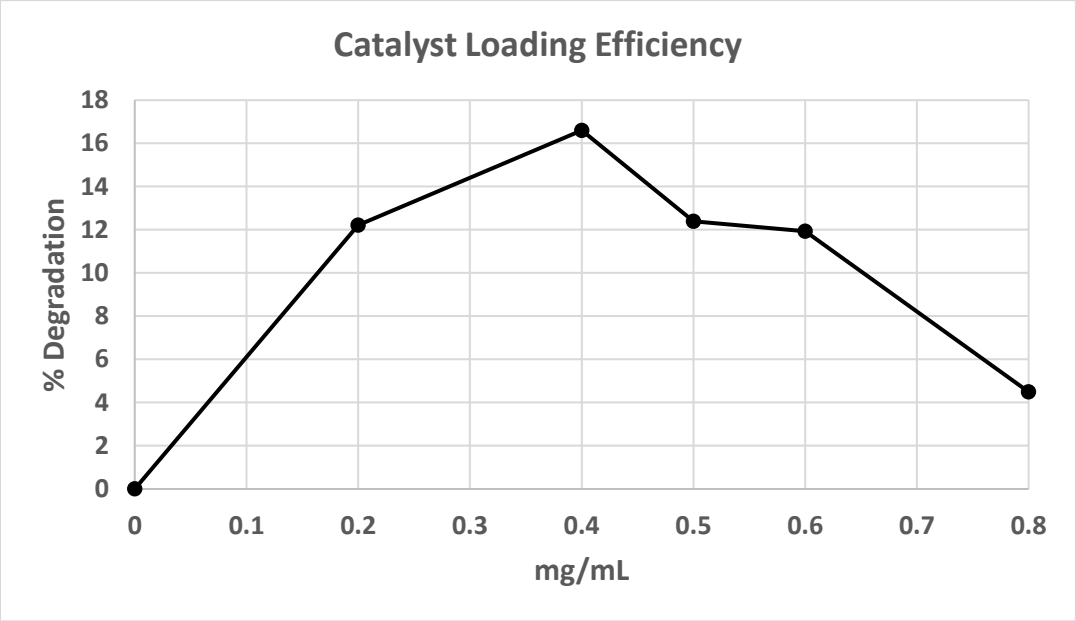

Figure 58: Catalyst loading curve for methylene blue tungstate experiments

Figure 60 is corrected to show no photodegradation of methylene blue under the xenon lamp. The true uncatalyzed degradation percentage was calculated to be 1.25%, which was subtracted from all other values to correct the graph. A loading concentration of 0.4 mg $NiWO_4$ catalyst per mL of the methylene blue solution was found to be the optimal value, and it was observed that more concentrated solutions became very opaque and most likely suffered from a shadowing effect. Another issue with higher concentrations occurs when the particles can no longer be properly dispersed. Clumps of nanoparticles can see aggregated at the bottom of the

beaker even with moderate stirring. This aggregation decreases the exposed surface area of the catalysts.

Methylene Blue has two peaks of interest, absorbing most strongly at 664nm and more weakly at 615nm. Photodegradation measurements were taken by measuring the absorbance at 664nm. If the peak shifted during degradation, the maximum absorbance closest to 664nm was used. In some measurements, scattering from still-suspended particles caused an apparent increase in absorbance. Where centrifugation was not sufficient to remove all particles, absorbances at 800nm and 420 nm were taken, and a slope was established to subtract scattering-related absorbances from the 664 peak. These two wavelengths were used, as methylene blue showed no absorbance there. Below is an example of the shift in absorbance during the photodegradation process.

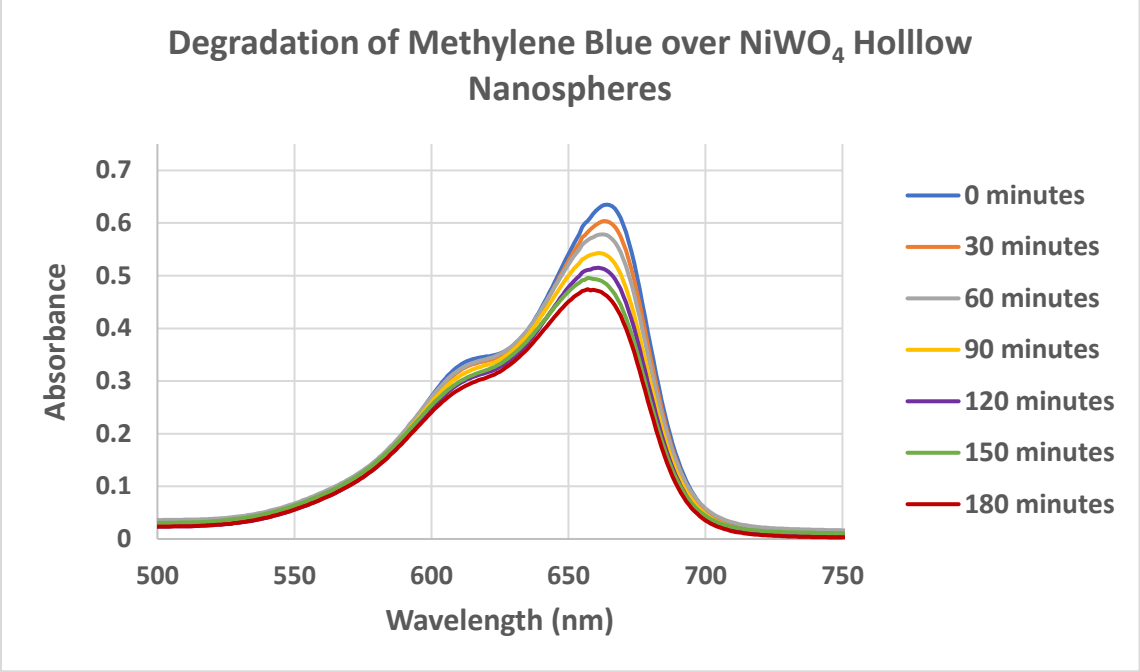

Figure 59: UV-Vis of methylene blue during photodegradation

4.1 – $NiWO_4$ Degradation of Methylene Blue

Multiple unique samples of $NiWO_4$ were synthesized during the attempt to dope it with silver. A properly doped sample was never created, a series of cocatalysts were prepared for degradation test of methylene blue. The hollow spheres of $NiWO_4$ with silver and the heterostructure of $NiWO_4$ with silver on its surface (co-catalyst) both have potential for high photocatalytic yield compared to the unmodified material. A bulk sample of $NiWO_4$ was prepared, along with a 3% and 9% doped sample. A sample of hollow spheres with 3% Ag per Ni was prepared as well.

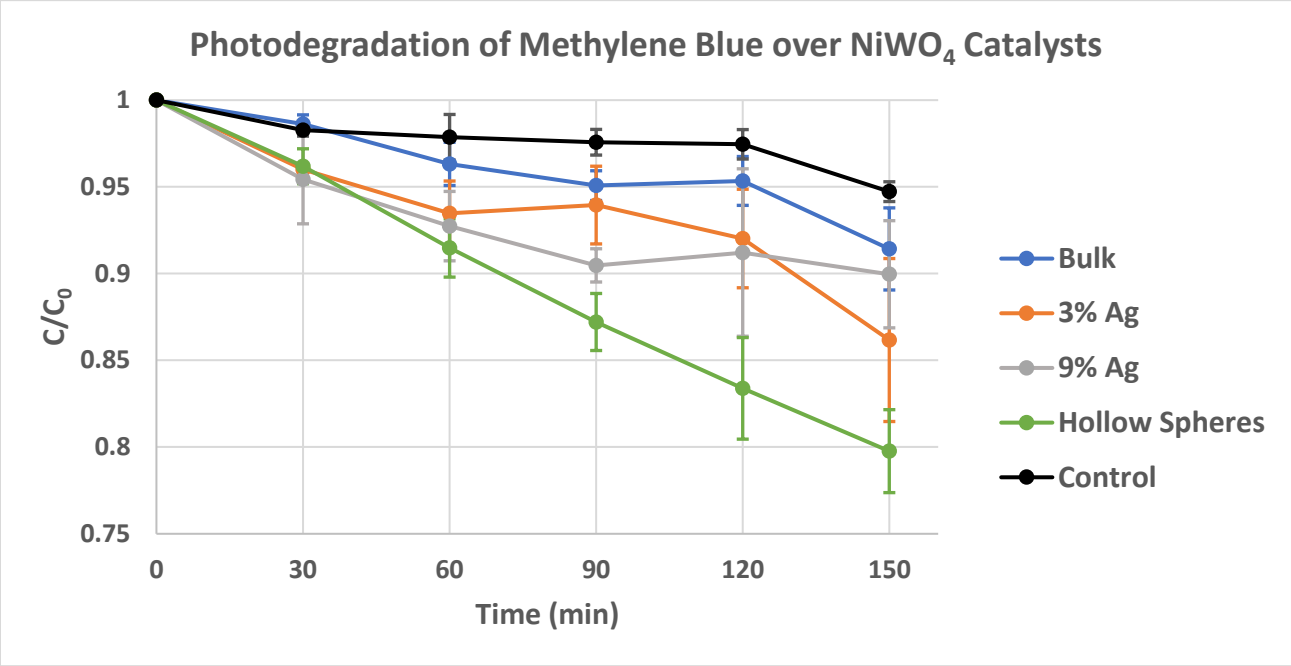

Figure 60: Photodegradation of methylene blue over $NiWO_4$ samples

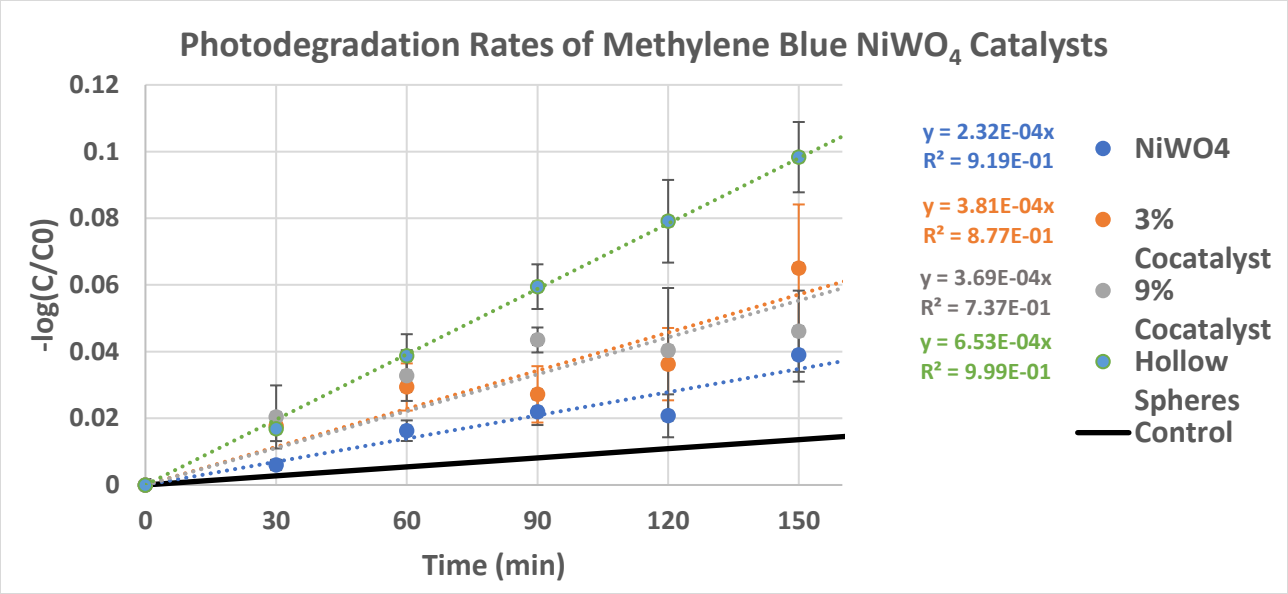

Figure 61: Photodegradation rates of methylene blue over $NiWO_4$ samples

All samples were shown to be active under the light of the xenon lamp, showing increased rate of degradation over the control sample. Three experiments were run for each sample to provide a statistical fit, though certain samples had large error due to multiple factors including particle dispersion and solvent loss. One sample which showed a highly consistent trend was the hollow sphere sample, which might be attributed to its colloidal nature. This ensured a complete dispersion of all nanoparticles within the solution. A first order kinetics fit was performed on the data, as reactive oxygen species and methylene blue are assumed to be abundant within the solution.

The silver doped nanoparticles showed an increased rate of photodegradation over the bulk $NiWO_4$, though the exact ratio cannot be defined due to error. The trend is observable with the fact that multiple experiments with multiple samples all still show a higher rate of degradation. There is little difference, however, between the 3% and 9% samples. This may be due to a sufficient surface presence of silver in the 3% sample, where additional silver provides

little to no benefit. Further experimentation is warranted to uncover a possible trend between the amount of silver doping and photodegradation rate.

The hollow sphere sample showed the highest rate of photodegradation per mass. There are many possible factors at play, which include its unique colloidal nature, or its potentially high surface area. Further study with BET to normalize activity to surface area is warranted. Unlike the other nanoparticles synthesized, the hollow nanospheres were the only ones which remained suspended in solution for long periods of time (>5min) without constant stirring. Figure 20 shows the IR of these samples, and indicates that there is a larger surface adsorption of water on these samples when compared to the other tungstates synthesized. This affinity to water may be one explanation as to why the hollow nanospheres remain suspended for longer periods of time. The sample is amorphous in nature, and contains many different environments at its surface which makes it difficult to reach a definitive contributor for its higher activity.

4.2 – $ZnWO_4$ Degradation of Methylene Blue

Like the $NiWO_4$ experiment, the $ZnWO_4$ experiment utilized a 300W Xenon lamp. Initially a test was run with a 295nm cutoff filter and the Pyrex. This combination cutoff filter ensures that at 309nm, or 4.01 eV, 50% of photons are blocked. At close to 298 nm only 1% of high energy photons pass through. This is an extremely important parameter, as $ZnWO_4$'s band gap is very high, and classically above 4 eV. As shown below, with the cutoff filter the rate of photodegradation for methylene blue dye over $ZnWO_4$ is effectively zero:

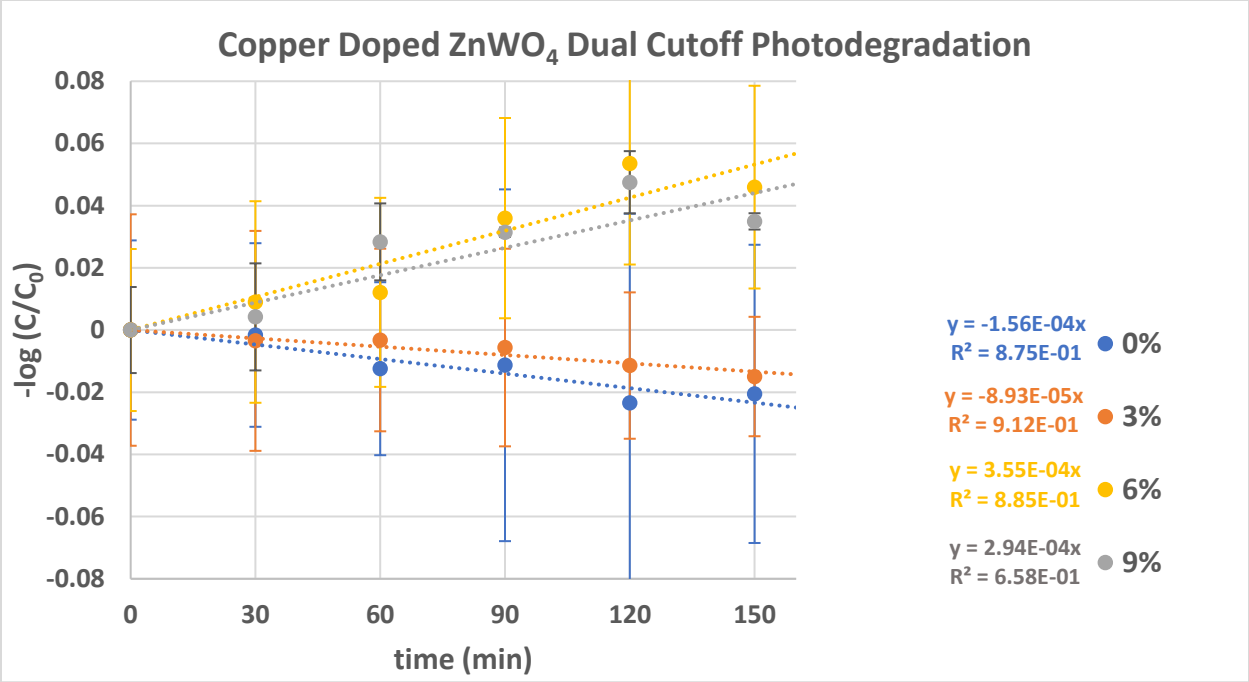

Figure 62: Photodegradation rates of methylene blue over $ZnWO_4$ samples with cutoff filter

While the photodegradation rate of the dye is extremely low, a slight downward slope appears, indicating that the solution is becoming more concentrated. It is likely that solvent loss outweighs any catalytic action of the $ZnWO_4$, shifting the apparent rate to a negative value.

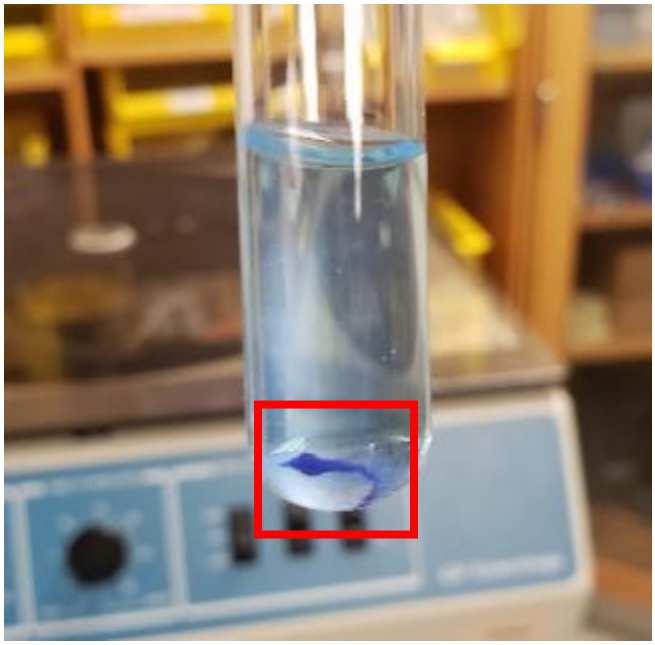

Figure 63: Methylene blue dye adsorbed to the $ZnWO_4$ catalyst

With the addition of copper to the $ZnWO_4$, once a doping threshold is crossed the material begins to degrade the dye at wavelengths above 309 nm. This is first observed at a doping percentage of 6%, yet seems to decrease at a percentage of 9%. This possibly shows the limit of doping for $ZnWO_4$ before the beneficial effects reach their peak. Below is a graph showing only the samples which had a positive rate of photodegradation for methylene blue at wavelengths above 295nm:

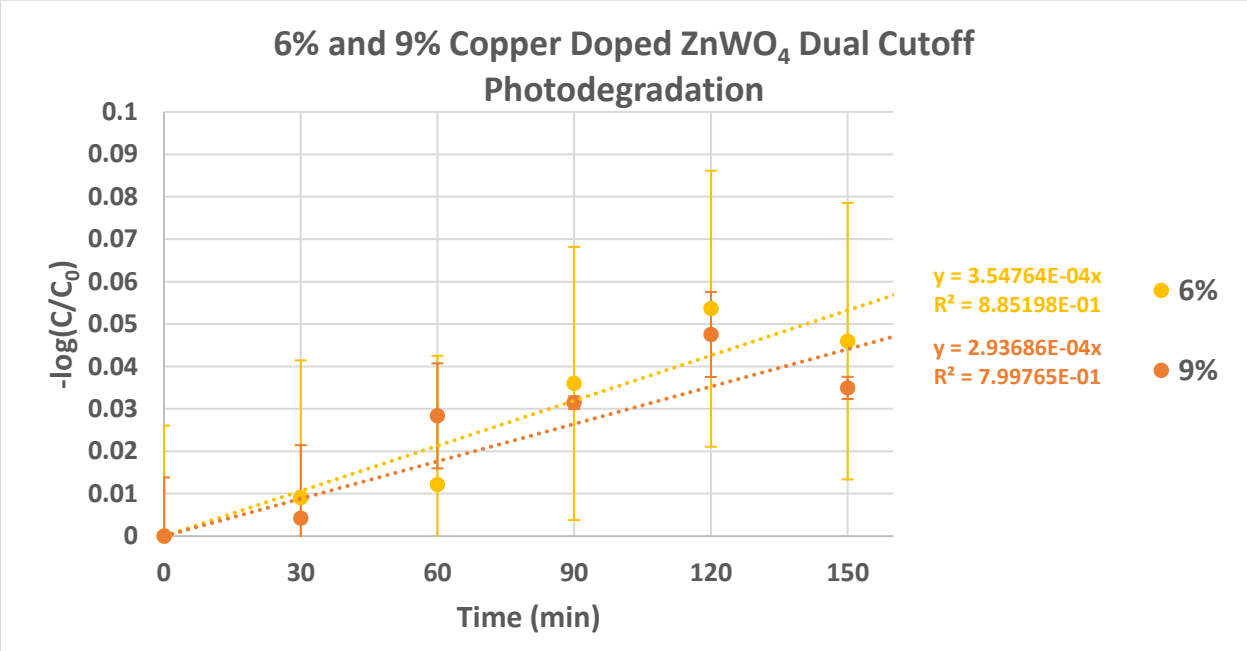

Figure 64: A graph of the relative performance of doped $ZnWO_4$ samples with cutoff filter

To assess the relative activity of undoped $ZnWO_4$ to the doped samples, the cutoff filter was removed, exposing the catalyst to photons with wavelengths up to 288 nm, with a cutoff wavelength of 301 nm (4.12 eV). It is important to note that the emission flux in this range from the Xenon lamp is relatively weak, and the rates of degradation are low as a result. These rates can be used as benchmarks against each other to probe relative efficiency.

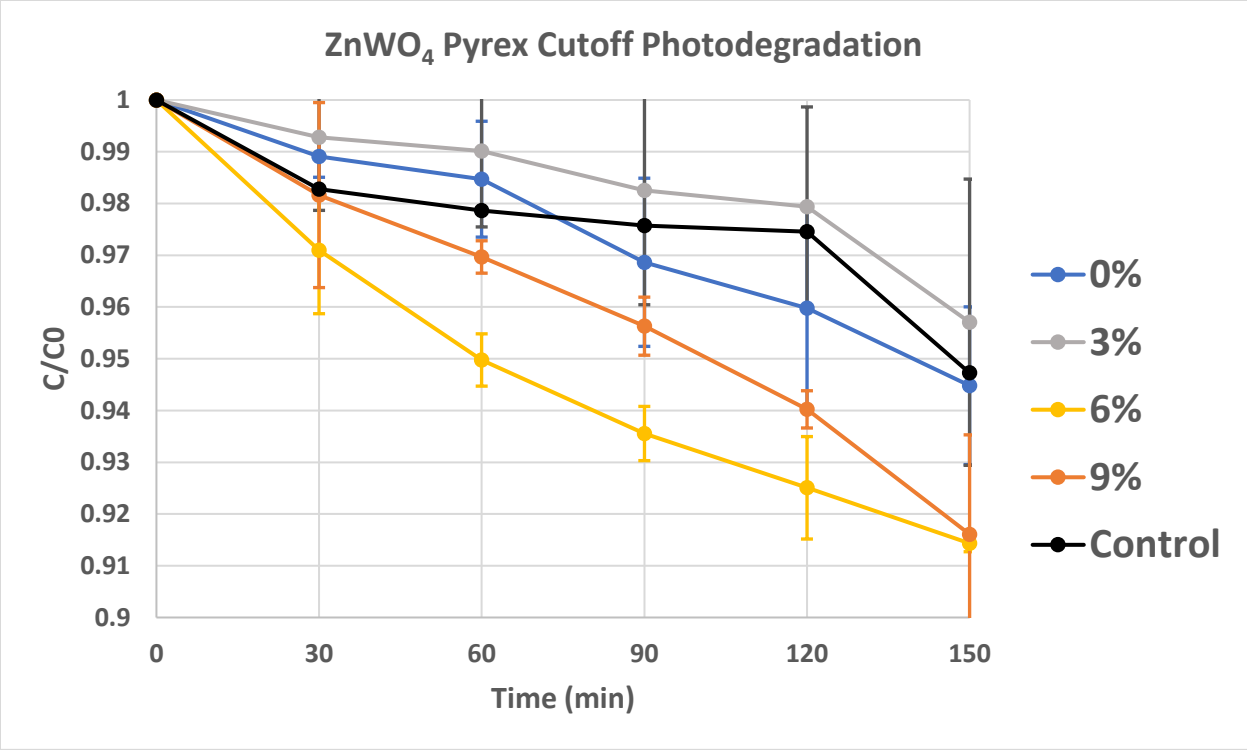

Figure 65: Photodegradation of methylene blue dye over copper doped $ZnWO_4$

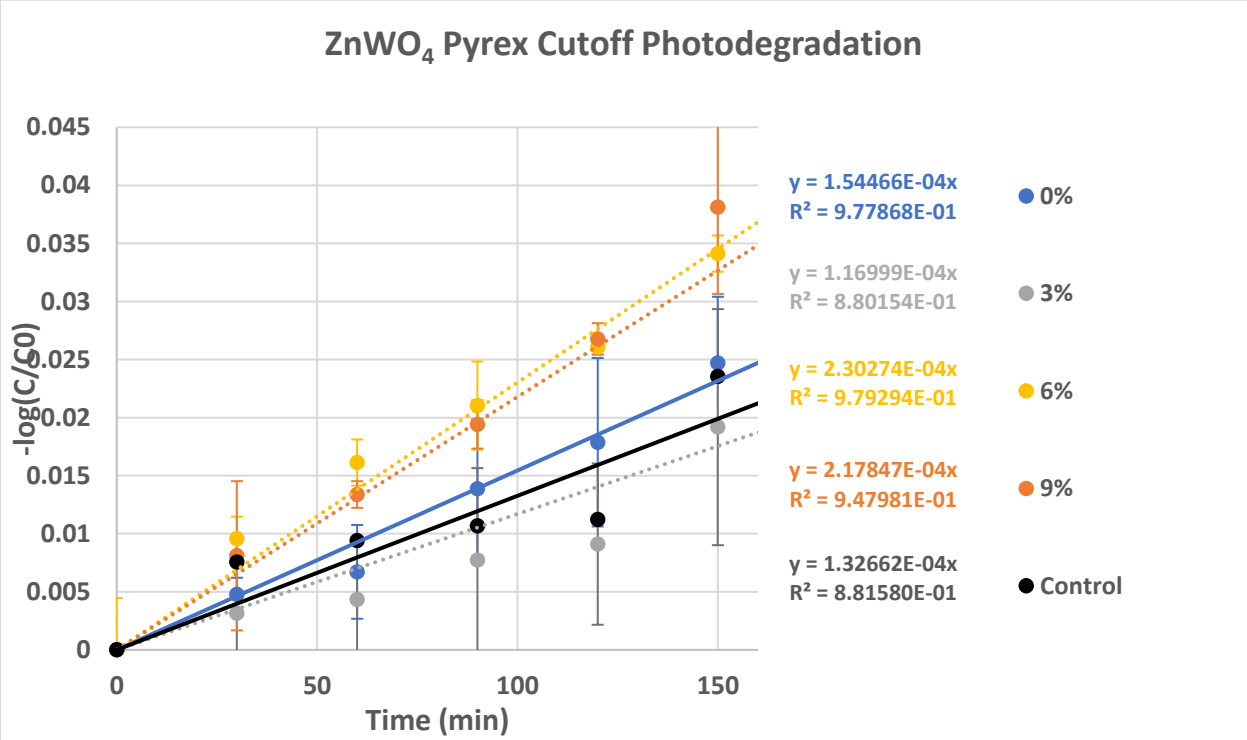

Figure 66: Photodegradation rates of methylene blue dye over $ZnWO_4$ with dual cutoff filters

With the full spectrum of the Xenon lamp shining on the $ZnWO_4$ samples, it can be seen that most samples degrade the methylene blue dye when excited by sufficient energy. With the undoped sample as a baseline, the 6% and 9% doped samples show a higher catalytic activity, while the 3% sample shows reduced activity. The reduced activity of the 3% sample can be explained when we consider the electronic structure of the $CuWO_4$ in the matrix. Copper has a d^9 electron configuration, which gives it a p-type dopant effect in $ZnWO_4$ as Zn has a d^{10} configuration. We must also consider that oxygen deficiencies may exist in small amounts in the $ZnWO_4$, existing as n-type dopants. This conflict of small doping amounts for both p and n type in the 3% sample may result in the reduced activity of the semiconductor. In larger amounts of doping, the p-type copper dopant may outnumber the oxygen deficiencies, allowing for higher activity as a result.

At 9% doping, however, the benefit of the dopant begins to decline, showing an activity very close to the undoped sample. $ZnWO_4$ conduction band[19] may lie very close to the reduction potential of $O_2/O_2^{-\bullet}$, and the reduction of the band gap may result in the shifting of the conduction band below the potential for this oxygen species, resulting in a lower activity.

5 – Conclusions and Future Work

Doping $NiWO_4$ with silver is not possible through conventional coprecipitation methods but using silver in this synthesis affords other potential catalysts, including a cocatalyst and a hollow sphere catalyst. Work with both of these materials is warranted to study their full potential. For the cocatalyst, a one-pot synthesis has been proposed, but the properties and catalytic activity of this material could be compared to a conventionally synthesized cocatalyst where the bulk $NiWO_4$ has silver deposited on the surface through a photo or electrodeposition.

The hollow sphere samples should be more closely studied to confirm the proposed mechanism of their formation and degradation, as well as the limits of their colloidal properties. An interesting experiment would be to attempt to fill the hollow spheres with a magnetic core material in order to impart magnetic properties to the inactive sites of the material, while still preserving their ability to perform chemistry on the outer shell surface.

It can be seen that there are at least two inflection points for catalytic rate with respect to doping amount of $ZnWO_4$ with copper, which justifies a more in-depth exploration to find the optimal doping level.

Finally, the photocatalysis experiments deserve a more optimized setup both with a more transparent material for the glassware in order to allow higher energy light into the sample, as well as a better setup to control solvent loss and vessel temperature.

References

(1) Bott, A. W.; Avenue, K. Electrochemistry of Semiconductors. *Curr. Sep.* **1998**, 5.

(2) Farsi, H.; Hosseini, S. A. The Electrochemical Behaviors of Methylene Blue on the Surface of Nanostructured NiWO4 Prepared by Coprecipitation Method. *J. Solid State Electrochem.* **2013**, *17* (7), 2079–2086. https://doi.org/10.1007/s10008-013-2068-5.

(3) Pandey, P. K.; Bhave, N. S.; Kharat, R. B. Structural, Optical, Electrical and Photovoltaic Electrochemical Characterization of Spray Deposited NiWO4 Thin Films. *Electrochimica Acta* **2006**, *51* (22), 4659–4664. https://doi.org/10.1016/j.electacta.2005.12.042.

(4) Grätzel, M. Solar Energy Conversion by Dye-Sensitized Photovoltaic Cells. *Inorg. Chem.* **2005**, *44* (20), 6841–6851. https://doi.org/10.1021/ic0508371.

(5) Charfi, W.; Chaabane, M.; Mhiri, H.; Bournot, P. Performance Evaluation of a Solar Photovoltaic System. *Energy Rep.* **2018**, *4*, 400–406. https://doi.org/10.1016/j.egyr.2018.06.004.

(6) He, J.; Li, B.; Chen, F.; Xu, Z.; Yin, G. Tungstates: Novel Heterogeneous Catalysts for the Synthesis of 5-Substituted 1H-Tetrazoles. *J. Mol. Catal. Chem.* **2009**, *304* (1–2), 135–138. https://doi.org/10.1016/j.molcata.2009.01.037.

(7) Rostamizadeh, S.; Ghaieni, H.; Aryan, R.; Amani, A. Zinc Chloride Catalyzed Synthesis of 5-Substituted 1H-Tetrazoles under Solvent Free Condition. *Chin. Chem. Lett.* **2009**, *20* (11), 1311–1314. https://doi.org/10.1016/j.cclet.2009.06.020.

(8) Macedo, N. G.; Gouveia, A. F.; Roca, R. A.; Assis, M.; Gracia, L.; Andrés, J.; Leite, E. R.; Longo, E. Surfactant-Mediated Morphology and Photocatalytic Activity of α-Ag_2WO_4 Material. *J. Phys. Chem. C* **2018**, *122* (15), 8667–8679. https://doi.org/10.1021/acs.jpcc.8b01898.

(9) Al-Amshany, Z. M.; Hussein, M. A. Novel Pd/ZnWO4 Nanocomposite Materials for Photocatalytic Degradation of Atrazine. *Appl. Nanosci.* **2018**, *8* (3), 527–536. https://doi.org/10.1007/s13204-018-0694-z.

(10) Tang, J.; Durrant, J. R.; Klug, D. R. Mechanism of Photocatalytic Water Splitting in TiO_2. Reaction of Water with Photoholes, Importance of Charge Carrier Dynamics, and Evidence for Four-Hole Chemistry. *J. Am. Chem. Soc.* **2008**, *130* (42), 13885–13891. https://doi.org/10.1021/ja8034637.

(11) Colinge, J.-P.; Colinge, C. A. Physics Of Semiconductor Devices. 441.

(12) Fu, Y.; Sun, D.; Chen, Y.; Huang, R.; Ding, Z.; Fu, X.; Li, Z. An Amine-Functionalized Titanium Metal-Organic Framework Photocatalyst with Visible-Light-Induced Activity for CO2 Reduction. *Angew. Chem. Int. Ed.* **2012**, *51* (14), 3364–3367. https://doi.org/10.1002/anie.201108357.

(13) Mead, C. A.; Spitzer, W. G. Fermi Level Position at Metal-Semiconductor Interfaces. *Phys. Rev.* **1964**, *134* (3A), A713–A716. https://doi.org/10.1103/PhysRev.134.A713.

(14) Morin, F. J.; Maita, J. P. Electrical Properties of Silicon Containing Arsenic and Boron. *Phys. Rev.* **1954**, *96* (1), 28–35. https://doi.org/10.1103/PhysRev.96.28.

(15) Mani, S.; Vediyappan, V.; Chen, S.-M.; Madhu, R.; Pitchaimani, V.; Chang, J.-Y.; Liu, S.-B. Hydrothermal Synthesis of NiWO4 Crystals for High Performance Non-Enzymatic Glucose Biosensors. *Sci. Rep.* **2016**, *6* (1). https://doi.org/10.1038/srep24128.

(16) Helaïli, N.; Boudjamaa, A.; Kebir, M.; Bachari, K. Efficient Photo–Catalytic Degradation of Malachite Green Using Nickel Tungstate Material as Photo–Catalyst. *Environ. Sci. Pollut. Res.* **2017**, *24* (7), 6481–6491. https://doi.org/10.1007/s11356-016-8296-3.

(17) Quintana-Melgoza, J. M.; Gómez-Cortés, A.; Avalos, M. REDUCTION OF NO BY CO OVER NiWO4, NiO, AND WO3 CATALYSTS. 10.
(18) Pavithra, N. S.; Nagaraju, G.; Viswanatha, R. Surfactant Assisted Sonochemical Synthesis of Zinc Tungstate Nanoparticles: Anode for Li-Ion Battery and Photocatalytic Activities. *Eur. Phys. J. Plus* **2018**, *133* (12). https://doi.org/10.1140/epjp/i2018-12248-x.
(19) Montini, T.; Gombac, V.; Hameed, A.; Felisari, L.; Adami, G.; Fornasiero, P. Synthesis, Characterization and Photocatalytic Performance of Transition Metal Tungstates. *Chem. Phys. Lett.* **2010**, 9.
(20) Shepard, S.; Smeu, M. Ab Initio Study of Structural and Electronic Properties of Copper and Nickel Tungstate. *Comput. Mater. Sci.* **2018**, *143*, 301–307. https://doi.org/10.1016/j.commatsci.2017.11.021.
(21) Masteri-Farahani, M.; Saemi, M. Microemulsion-Mediated Synthesis, Characterization and Optical Properties of Spherical Nickel Tungstate Nanocrystals. *J. Mater. Sci. Mater. Electron.* **2017**, *28* (2), 1328–1335. https://doi.org/10.1007/s10854-016-5664-1.
(22) Karthiga, R.; Kavitha, B.; Rajarajan, M.; Suganthi, A. Photocatalytic and Antimicrobial Activity of NiWO4 Nanoparticles Stabilized by the Plant Extract. *Mater. Sci. Semicond. Process.* **2015**, *40*, 123–129. https://doi.org/10.1016/j.mssp.2015.05.037.
(23) Talebi, R. Simple Sonochemical Synthesis and Characterization of Nickel Tungstate Nanoparticles and Its Photocatalyst Application. *J. Mater. Sci. Mater. Electron.* **2016**, *27* (4), 3565–3569. https://doi.org/10.1007/s10854-015-4192-8.
(24) Pourmortazavi, S. M.; Rahimi-Nasrabadi, M.; Khalilian-Shalamzari, M.; Zahedi, M. M.; Hajimirsadeghi, S. S.; Omrani, I. Synthesis, Structure Characterization and Catalytic Activity of Nickel Tungstate Nanoparticles. *Appl. Surf. Sci.* **2012**, *263*, 745–752. https://doi.org/10.1016/j.apsusc.2012.09.153.
(25) de Oliveira, A. L. M.; Ferreira, J. M.; Silva, M. R. S.; de Souza, S. C.; Vieira, F. T. G.; Longo, E.; Souza, A. G.; Santos, I. M. G. Influence of the Thermal Treatment in the Crystallization of NiWO4 and ZnWO4. *J. Therm. Anal. Calorim.* **2009**, *97* (1), 167–172. https://doi.org/10.1007/s10973-009-0244-8.
(26) Dkhilalli, F.; Borchani, S. M.; Rasheed, M.; Barille, R.; Guidara, K.; Megdiche, M. Structural, Dielectric, and Optical Properties of the Zinc Tungstate ZnWO4 Compound. *J. Mater. Sci. Mater. Electron.* **2018**, *29* (8), 6297–6307. https://doi.org/10.1007/s10854-018-8609-z.
(27) Hosseinpour-mashkani, S. M.; Sobhani-Nasab, A. Simple Synthesis and Characterization of Copper Tungstate Nanoparticles: Investigation of Surfactant Effect and Its Photocatalyst Application. *J. Mater. Sci. Mater. Electron.* **2016**, *27* (7), 7548–7553. https://doi.org/10.1007/s10854-016-4735-7.
(28) Forsyth, J. B.; Wilkinson, C.; Zvyagin, A. I. The Antiferromagnetic Structure of Copper Tungstate, $CuWO_4$. *J. Phys. Condens. Matter* **1991**, *3* (43), 8433–8440. https://doi.org/10.1088/0953-8984/3/43/010.
(29) López, X. A.; Fuentes, A. F.; Zaragoza, M. M.; Díaz Guillén, J. A.; Gutiérrez, J. S.; Ortiz, A. L.; Collins-Martínez, V. Synthesis, Characterization and Photocatalytic Evaluation of MWO4 (M = Ni, Co, Cu and Mn) Tungstates. *Int. J. Hydrog. Energy* **2016**, *41* (48), 23312–23317. https://doi.org/10.1016/j.ijhydene.2016.10.117.
(30) George, T.; Joseph, S.; Mathew, S. Synthesis and Characterization of Nanophased Silver Tungstate. *Pramana* **2005**, *65* (5), 793–799. https://doi.org/10.1007/BF02704077.

(31) Pavithra, N. S.; Nagaraju, G.; Viswanatha, R. Surfactant Assisted Sonochemical Synthesis of Zinc Tungstate Nanoparticles: Anode for Li-Ion Battery and Photocatalytic Activities. *Eur. Phys. J. Plus* **2018**, *133* (12). https://doi.org/10.1140/epjp/i2018-12248-x.
(32) Pourmortazavi, S. M.; Rahimi-Nasrabadi, M.; Khalilian-Shalamzari, M.; Ghaeni, H. R.; Hajimirsadeghi, S. S. Facile Chemical Synthesis and Characterization of Copper Tungstate Nanoparticles. *J. Inorg. Organomet. Polym. Mater.* **2014**, *24* (2), 333–339. https://doi.org/10.1007/s10904-013-9970-2.
(33) Pourmortazavi, S. M.; Rahimi-Nasrabadi, M.; Khalilian-Shalamzari, M.; Zahedi, M. M.; Hajimirsadeghi, S. S.; Omrani, I. Synthesis, Structure Characterization and Catalytic Activity of Nickel Tungstate Nanoparticles. *Appl. Surf. Sci.* **2012**, *263*, 745–752. https://doi.org/10.1016/j.apsusc.2012.09.153.
(34) Kumari, U. S.; Suresh, P.; Rao, A. V. P. Grinding-Assisted Solid-State Metathetic Synthesis of Divalent Transition Metal Tungstates. *Appl. Chem.* **2013**, 9.
(35) Parhi, P.; Karthik, T. N.; Manivannan, V. Synthesis and Characterization of Metal Tungstates by Novel Solid-State Metathetic Approach. *J. Alloys Compd.* **2008**, *465* (1–2), 380–386. https://doi.org/10.1016/j.jallcom.2007.10.089.
(36) Nadaraia, L.; Jalabadze, N.; Chedia, R.; Antadze, M.; Khundadze, L. Preparation of Tungstate Nanopowders by Sol-Gel Method. *IEEE Trans. Nucl. Sci.* **2010**, *57* (3), 1370–1376. https://doi.org/10.1109/TNS.2009.2034003.
(37) Zalga, A.; Moravec, Z.; Pinkas, J.; Kareiva, A. On the Sol–Gel Preparation of Different Tungstates and Molybdates. *J. Therm. Anal. Calorim.* **2011**, *105* (1), 3–11. https://doi.org/10.1007/s10973-011-1367-2.
(38) Thomas, A.; Janµky, C.; Samu, G. F.; Huda, M. N.; Sarker, P.; Liu, J. P.; van Nguyen, V.; Wang, E. H.; Schug, K. A.; Rajeshwar, K. Time- and Energy-Efficient Solution Combustion Synthesis of Binary Metal Tungstate Nanoparticles with Enhanced Photocatalytic Activity. **2015**, 13.
(39) Hosseini, S.; Farsi, H.; Moghiminia, S.; Zubkov, T.; Lightcap, I. V.; Riley, A.; Peters, D. G.; Li, Z. Nickel Tungstate ($NiWO_4$) Nanoparticles/Graphene Composites: Preparation and Photoelectrochemical Applications. *Semicond. Sci. Technol.* **2018**, *33* (5), 055008. https://doi.org/10.1088/1361-6641/aab938.
(40) Lopes, T.; Andrade, L.; Ribeiro, H. A.; Mendes, A. Characterization of Photoelectrochemical Cells for Water Splitting by Electrochemical Impedance Spectroscopy. *Int. J. Hydrog. Energy* **2010**, *35* (20), 11601–11608. https://doi.org/10.1016/j.ijhydene.2010.04.001.
(41) Yu, J.; Qi, L.; Jaroniec, M. Hydrogen Production by Photocatalytic Water Splitting over Pt/TiO_2 Nanosheets with Exposed (001) Facets. *J. Phys. Chem. C* **2010**, *114* (30), 13118–13125. https://doi.org/10.1021/jp104488b.
(42) Yu, J.; Low, J.; Xiao, W.; Zhou, P.; Jaroniec, M. Enhanced Photocatalytic CO_2 -Reduction Activity of Anatase TiO_2 by Coexposed {001} and {101} Facets. *J. Am. Chem. Soc.* **2014**, *136* (25), 8839–8842. https://doi.org/10.1021/ja5044787.
(43) Habisreutinger, S. N.; Schmidt-Mende, L.; Stolarczyk, J. K. Photocatalytic Reduction of CO_2 on TiO_2 and Other Semiconductors. *Angew. Chem. Int. Ed.* **2013**, *52* (29), 7372–7408. https://doi.org/10.1002/anie.201207199.
(44) Sari, S.; Aysan, E.; Muslumanoglu, M.; Ersoy, Y. E.; Bektasoglu, H.; Yard¿mc¿, E. Safe Thyroidectomy with Intraoperative Methylene Blue Spraying. *Thyroid Res.* **2012**, *5* (1), 15. https://doi.org/10.1186/1756-6614-5-15.

(45) Trust, T. J. Inadequacy of Aquarium Antibacterial Formulations for the Inhibition of Potential Pathogens of Freshwater Fish. *J. Fish. Res. Board Can.* **1972**, *29* (10), 1425–1430. https://doi.org/10.1139/f72-221.
(46) Cenens, J. Visible Spectroscopy of Methylene Blue on Hectorite, Laponite B, and Barasym in Aqueous Suspension. *Clays Clay Miner.* **1988**, *36* (3), 214–224. https://doi.org/10.1346/CCMN.1988.0360302.
(47) Mamba, G.; Mbianda, X. Y.; Mishra, A. K. Gadolinium Nanoparticle-Decorated Multiwalled Carbon Nanotube/Titania Nanocomposites for Degradation of Methylene Blue in Water under Simulated Solar Light. *Environ. Sci. Pollut. Res.* **2014**, *21* (8), 5597–5609. https://doi.org/10.1007/s11356-014-2499-2.
(48) Kerkez, Ö.; Boz, İ. Photodegradation of Methylene Blue with Ag_2O/TiO_2 under Visible Light: Operational Parameters. *Chem. Eng. Commun.* **2015**, *202* (4), 534–541. https://doi.org/10.1080/00986445.2013.853292.
(49) Johnson, L. V.; Walsh, M. L.; Chen, L. B. Localization of Mitochondria in Living Cells with Rhodamine 123. *Proc. Natl. Acad. Sci.* **1980**, *77* (2), 990–994. https://doi.org/10.1073/pnas.77.2.990.
(50) Gallery, J.; Gouterman, M.; Callis, J.; Khalil, G.; McLachlan, B.; Bell, J. Luminescent Thermometry for Aerodynamic Measurements. *Rev. Sci. Instrum.* **1994**, *65* (3), 712–720. https://doi.org/10.1063/1.1145090.
(51) Zhang, J.; Liu, H.; Ma, Z. Flower-like Ag 2 O/Bi 2 MoO 6 p-n Heterojunction with Enhanced Photocatalytic Activity under Visible Light Irradiation. *J. Mol. Catal. Chem.* **2016**, *424*, 37–44. https://doi.org/10.1016/j.molcata.2016.08.009.
(52) Taniguchi, M.; Lindsey, J. S. Database of Absorption and Fluorescence Spectra of >300 Common Compounds for Use in PhotochemCAD. *Photochem. Photobiol.* **2018**, *94* (2), 290–327. https://doi.org/10.1111/php.12860.
(53) Wang, D.; Liu, Z.-P.; Yang, W.-M. Revealing the Size Effect of Platinum Cocatalyst for Photocatalytic Hydrogen Evolution on TiO_2 Support: A DFT Study. *ACS Catal.* **2018**, *8* (8), 7270–7278. https://doi.org/10.1021/acscatal.8b01886.
(54) Mei, B.; Han, K.; Mul, G. Driving Surface Redox Reactions in Heterogeneous Photocatalysis: The Active State of Illuminated Semiconductor-Supported Nanoparticles during Overall Water-Splitting. *ACS Catal.* **2018**, *8* (10), 9154–9164. https://doi.org/10.1021/acscatal.8b02215.
(55) Gelderman, K.; Lee, L.; Donne, S. W. Flat-Band Potential of a Semiconductor: Using the Mott–Schottky Equation. *J. Chem. Educ.* **2007**, *84* (4), 685. https://doi.org/10.1021/ed084p685.
(56) Choi, Y.; Kim, H.; Moon, G.; Jo, S.; Choi, W. Boosting up the Low Catalytic Activity of Silver for H_2 Production on Ag/TiO_2 Photocatalyst: Thiocyanate as a Selective Modifier. *ACS Catal.* **2016**, *6* (2), 821–828. https://doi.org/10.1021/acscatal.5b02376.
(57) Petica, A.; Florea, A.; Gaidau, C.; Balan, D.; Anicai, L. Synthesis and Characterization of Silver-Titania Nanocomposites Prepared by Electrochemical Method with Enhanced Photocatalytic Characteristics, Antifungal and Antimicrobial Activity. *J. Mater. Res. Technol.* **2017**, S223878541730056X. https://doi.org/10.1016/j.jmrt.2017.09.009.
(58) Li-Advisor, D. Z. Seyyedmairhossein Hosseini, Ball State University, 2016.
(59) Pandey, P. K.; Bhave, N. S.; Kharat, R. B. Structural, Optical, Electrical and Photovoltaic Electrochemical Characterization of Spray Deposited NiWO4 Thin Films. *Electrochimica Acta* **2006**, *51* (22), 4659–4664. https://doi.org/10.1016/j.electacta.2005.12.042.

(60) Zheng, X.; Xie, Y.; Zhu, L.; Jiang, X.; Yan, A. Formation of Vesicle-Templated CdSe Hollow Spheres in an Ultrasound-Induced Anionic Surfactant Solution. *Ultrason. Sonochem.* **2002**, *9* (6), 311–316. https://doi.org/10.1016/S1350-4177(02)00086-X.
(61) Mancheva, M. N.; Iordanova, R. S.; Klissurski, D. G.; Tyuliev, G. T.; Kunev, B. N. Direct Mechanochemical Synthesis of Nanocrystalline NiWO $_4$. *J. Phys. Chem. C* **2007**, *111* (3), 1101–1104. https://doi.org/10.1021/jp065071k.
(62) Mursa, A.; Busch. Solubility Rules, 2018.
(63) Krivec, S.; Detzel, T.; Buchmayr, M.; Hutter, H. On the Temperature Dependence of Na Migration in Thin SiO2 Films during ToF-SIMS O2+ Depth Profiling. *Appl. Surf. Sci.* **2010**, *257* (1), 25–32. https://doi.org/10.1016/j.apsusc.2010.06.019.
(64) Niu, L.; Li, Z.; Xu, Y.; Sun, J.; Hong, W.; Liu, X.; Wang, J.; Yang, S. Simple Synthesis of Amorphous NiWO $_4$ Nanostructure and Its Application as a Novel Cathode Material for Asymmetric Supercapacitors. *ACS Appl. Mater. Interfaces* **2013**, *5* (16), 8044–8052. https://doi.org/10.1021/am402127u.
(65) Hofman, E.; Robinson, R. J.; Li, Z.-J.; Dzikovski, B.; Zheng, W. Controlled Dopant Migration in CdS/ZnS Core/Shell Quantum Dots. *J. Am. Chem. Soc.* **2017**, *139* (26), 8878–8885. https://doi.org/10.1021/jacs.7b02320.
(66) Logvinenko, V.; Bakovets, V.; Trushnikova, L. Decomposition Processes of Nickel Hydroxide. *J. Therm. Anal. Calorim.* **2012**, *107* (3), 983–987. https://doi.org/10.1007/s10973-011-1689-0.
(67) Fuhrmann, T.; Schlegel, S.; Hoidis, M. Comparison between Nickel and Silver as Coating Materials of Conductors Made of Copper or Aluminum Used in Electric Power Engineering. **2014**, 6.
(68) Severo, E. da C.; Abaide, E. R.; Anchieta, C. G.; Foletto, V. S.; Weber, C. T.; Garlet, T. B.; Collazzo, G. C.; Mazutti, M. A.; Gündel, A.; Kuhn, R. C.; et al. Preparation of Zinc Tungstate (ZnWO4) Particles by Solvo-Hydrothermal Technique and Their Application as Support for Inulinase Immobilization. *Mater. Res.* **2016**, *19* (4), 781–785. https://doi.org/10.1590/1980-5373-MR-2015-0100.